Ph.D. Dissertation

Doppler wind LIDAR systems data processing and applications: An overview towards developing the new generation of wind remote-sensing sensors for off-shore wind farms

A thesis submitted to the Universitat Politècnica de Catalunya
in partial fulfillment for the degree of

Doctor of Philosophy

Miguel Ángel Gutiérrez Antuñano

Remote Sensing Laboratory
Department of Signal Theory and Communications

Doctorate program in
Signal Theory and Communications

Supervisors:
Dr. Francesc Rocadenbosch Burillo
Dr. Jordi Tiana Alsina

Barcelona, July 2019

UNIVERSITAT POLITÈCNICA DE CATALUNYA
BARCELONATECH
Escola de Doctorat

Acta de qualificació de tesi doctoral

Curs acadèmic:

Nom i cognoms

Programa de doctorat

Unitat estructural responsable del programa

Resolució del Tribunal

Reunit el Tribunal designat a l'efecte, el doctorand / la doctoranda exposa el tema de la seva tesi doctoral titulada

____

____.

Acabada la lectura i després de donar resposta a les qüestions formulades pels membres titulars del tribunal, aquest atorga la qualificació:

☐ NO APTE ☐ APROVAT ☐ NOTABLE ☐ EXCEL·LENT

(Nom, cognoms i signatura) President/a	(Nom, cognoms i signatura) Secretari/ària

(Nom, cognoms i signatura) Vocal	(Nom, cognoms i signatura) Vocal	(Nom, cognoms i signatura) Vocal

______________________, _______ d'/de __________________ de _______________

El resultat de l'escrutini dels vots emesos pels membres titulars del tribunal, efectuat per la Comissió Permanent de l'Escola de Doctorat, atorga la MENCIÓ CUM LAUDE:

☐ SÍ ☐ NO

(Nom, cognoms i signatura) President/a de la Comissió Permanent de l'Escola de Doctorat	(Nom, cognoms i signatura) Secretari/ària de la Comissió Permanent de l'Escola de Doctorat

Barcelona, _______ d'/de ____________________ de _________

Menció Internacional en el títol de doctor o doctora

- Com a secretari/ària del tribunal faig constar que part de la tesi doctoral, com a mínim el resum i les conclusions, s'ha redactat i presentat en una de les llengües habituals per a la comunicació científica en el seu camp de coneixement i diferent de les que són oficials a Espanya. Aquesta norma no s'aplica si l'estada, els informes i els experts provenen d'un país de parla hispana.

(Nom, cognoms i signatura) Secretari/ària del Tribunal

Ph.D. Dissertation

Doppler wind LIDAR systems data processing and applications: An overview towards developing the new generation of wind remote-sensing sensors for off-shore wind farms

A thesis submitted to the Universitat Politècnica de Catalunya
in partial fulfillment for the degree of

Doctor of Philosophy

Miguel Ángel Gutiérrez Antuñano

UNIVERSITAT POLITÈCNICA
DE CATALUNYA
BARCELONATECH

Remote Sensing Laboratory
Department of Signal Theory and Communications

Doctorate program in
Signal Theory and Communications

Supervisors:
Dr. Francesc Rocadenbosch Burillo
Dr. Jordi Tiana Alsina

Barcelona, June 2018

Doppler wind LIDAR systems data processing and applications: An overview towards developing the new generation of wind remote-sensing sensors for off-shore wind farms

[a] CommSensLab,
https://www.tsc.upc.edu/en/research/research-groups/commsenslab, https://ors.upc.edu/
Department of Signal Theory and Communications, Universitat Politècnica de Catalunya (UPC),
E-08034, Barcelona, Spain

[b] Institut d'Estudis Espacials de Catalunya (IEEC, Institute of Space Studies of Catalonia),
http://www.ieec.cat/en/home
E-08034, Barcelona, Spain

[c] Nonlinear Dynamics, Nonlinear Optics and Lasers (DONLL),
https://donll.upc.edu/en
Department of Physics (DFIS), Universitat Politècnica de Catalunya (UPC),
E-08022, Terrassa, Spain

Dedicado a los que me han acompañado, me acompañan y me acompañarán en este viaje a través del espacio y el tiempo.

Acknowledgments

The following institutions are gratefully acknowledged for their contribution to this work:

- *European Institute of Innovation and Technology (EIT)* - KIC InnoEnergy project NEPTUNE (Offshore Metocean Data Measuring Equipment and Wind, Wave and Current Analysis and Forecasting Software, call 2011) with the participation of the Catalonia Institute for Energy Research (IREC, PI. and Project Coordinator F. Schuon), Maritime Engineering Lab. of Universitat Politècnica de Catalunya (LIM-UPC, PI. D. González-Marco), Remote Sensing Lab. (RSLAB-UPC, PI. F. Rocadenbosch), University of Stuttgart (USTUTT, PI. O. Bischoff), Centro de Investigaciones Energéticas Medioambientales y Tecnológicas (CIEMAT, PI. A. Palomares), Gas Natural Fenosa (GNF, PI. R. Jané), and Soluciones de Ingeniería Marítima Operacional (SIMO, PI. F. Hermosilla).
- *European Union* - FP7 ITN Marie Curie project, ITARS (Initial Training in Atmospheric Remote Sensing), GA-289923.
- *Remote Sensing, Antennas, Microwaves and Superconductivity Group* (CommSensLab*) of the Universitat Politècnica de Catalunya (UPC).
- *Spanish Ministry of Science, Innovation and Universities* (Ministerio de Ciencia, Innovación y Universidades, MICINN) and *European Regional Development Fund* (FEDER) under **PGC2018-094132-B-I00** (Atmos. Rem. Sens. with cooperative lidar, radar and passive sensors) and TEC2015-63832 projects.
- *Microwave Remote Sensing Laboratory* (MIRSL) and Computer Engineering (Prof. Dr. Steve Frasier) for hosting the author (from 29 Feb 2016 to 30 May 2016) during the research stay carried out in this Ph.D. *Thesis submitted for **International Mention**.*
- *Laboratory of Maritime Engineering* (LIM) of the *Universitat Politècnica de Catalunya* (UPC) for the technical leadership in NEPTUNE project, development of the prototype buoy and cardan frame, and endless tests carried out at their laboratory premises, PdP and IJmuiden's facilities.
- *Stuttgart Wind Energy* (SWE) of the *University of Stuttgart* (USTUTT) at the initial stages of software development during the campaign.
- EOLOS FLS SA for the measurement campaign which is part of this study.

  *CommSensLab is an Excellence Unit (Unidad de Excelencia María de Maeztu, MDM-2016-0600 funded by the Agencia Estatal de Investigación).

Esta tesis es el resultado de mucho tiempo, esfuerzo y cariño por parte de muchas personas.

En primer lugar dar mi más sincero agradecimiento a los dos directores de esta tesis, Francesc Rocadenbosch Burillo y Jordi Tiana Alsina, por confiar en mí para realizar este proyecto y ayudarme a recorrer este largo camino. Sin vuestra experiencia y paciencia no habríamos llegado hasta aquí.

También tengo que mencionar a la gran familia de Acciona Energía en Navarra, especialmente a Sancho Laspalas y Manuel Calleja por sus enseñanzas y abrirme la puerta del mundo de la energía eólica. Es imporante para mí destacar que quién me trajo a Barcelona fue Frieder Schuon que además me ha dado un grandísimo ejemplo de dedicación y esfuerzo.

Me gustaría reservar unas líneas para Steve Frasier por darme la oportunidad de visitar la Universidad de Massachusetts y conocér gente muy especial. Debo agradecer también al equipo del CITM y el Departamento de Física del campus Besòs por confiar en mi y así descubrir lo mucho que me gusta la docencia y compartir lo poco que sé.

Una de las cosas que más ha marcado mi estancia en esta bellísima ciudad es el conocer al Sifu José María Prat, aprender artes marciales y tener unos hermanos de Kung Fu que espero que sigamos cuidándonos siempre como nos hemos cuidado hasta ahora.

Como no puedo mencionar a todos los que querría, quiero recordar simplemente a Barcelona, Paris, Sarriguren, Amherst, Santander, Bilbao. Lugares que engloban muchas cosas, muchos recuerdos y muchas personas. Y por supuesto Castro.

Mi agradecimiento a mi familia y amigos por haberme hecho como soy. En mi corazón siempre llevaré a Canela, a Bandera y sobretodo a Lennon. Finalizar con un recuerdo muy especial a mi padre por todo su apoyo incondicional para que aprendiese, como persona y como profesional, y realizase este doctorado.

The purpose of this Thesis is the study of a focusable continuous-wave Doppler lidar and its use in offshore wind energy. The use of lidars mounted on floating platforms such as buoys is studied to measure the wind field in offshore and deep-sea sites. This technology, developed within the framework of the European project NEPTUNE, is of interest for the wind industry sector since it allows to gather data with similar precision as meteorological met-masts but with an important reduction on costs that would facilitate the transition to a low-carbon economy.

The main goal of this Thesis is to investigate different solutions capable of reducing the sea-motion influence on the floating-lidar measurements. To that end, different approaches, from mechanical solutions to post-processing algorithms, are proposed and analysed. First, performance of the cardan-frame solution (i.e., gimbal stabilizer) to counter-balance the motion of the Doppler lidar installed on the floating buoy is studied. Second, advanced filtering techniques are proposed to cancel out the effects of buoy motion in offshore wind lidars. Finally, a lidar motion simulator is developed to numerically assess the effects of buoy tilting on wind-lidar measurements performance and accuracy. Such post-processing techniques enable enhancement of data quality, namely, 1-s (high temporal resolution) wind and turbulence intensity measurements. Both are critical variables in wind turbine design and wind farm planning.

To validate the suitability of the proposed methodologies, floating lidar measurements are cross-examined against fixed-lidar and reference measurements. Data processing techniques (including adaptive temporal averaging and spectral analysis) and classic statistical analysis tools are used to assess Key Performance Indicators and to evaluate and refine data quality. These techniques are applied to both raw and motion-corrected data, thus evidencing their capability to reduce motion-induced errors in wind-lidar measurements.

Three different measurement campaigns have been carried out during this thesis: (i) *Laboratory tests* with a view to define the comparison criteria between the reference and the moving lidar as well as preliminary tests to evaluate the suitability of the cardan frame as a mechanical motion-compensation device. (ii) *Proof-of-concept near-off-shore tests* to assess the behaviour of the lidar buoy under monitored real sea conditions (MARHIS Scientific-Technical Singular Infrastructure (ICTS) facility, LIM-UPC). (iii) Finally, validation of the lidar buoy has been carried out under real operating conditions during the 6-month off-shore campaign at IJmuiden, North Sea, as part of the floating lidar *commissioning phase*. These three measurement campaigns have provided an exceptional opportunity to assess and improve the motion-correction techniques developed in this Ph.D.

El objetivo de esta Tesis es el estudio del lidar focalizable Doppler de onda contínua y su uso en la energía eólica marina. El uso de lidares montados en plataformas flotantes como boyas se estudia para medir el campo de viento en entornos marinos de gran profundidad. Esta tecnología, desarrollada en el marco del proyecto europeo NEPTUNE, es de gran interés para la industria eólica ya que permite registrar data con una precisión similar a la de un mástil meteorológico pero con una gran reducción de costes, lo que facilitará la transición hacia una economía con baja emisión de carbono.

El objetivo principal de esta Tesis es investigar diferentes soluciones capaces de reducir la influencia del movimiento en las medidas de un lidar flotante. Para ello, diferentes aproximaciones, desde una compensación mecánica hasta algoritmos de post-procesado, son propuestas y analizadas. En primer lugar, se ha analizado la efectividad de un marco cardánico (i.e., una estabilizador mecánico) que contrarresta el movimiento del lidar situado en una plataforma flotante. En un segundo enfoque, se proponen diferentes técnicas de filtrado avanzado para cancelar los efectos del movimiento de la boya en los datos del lidar. Finalmente, se ha desarrollado un simulador capaz de evaluar numéricamente el impacto de la inclinación del lidar en la calidad y precisión de sus medidas. Estas técnicas de post-procesado permiten mejorar la calidad de los datos de alta resolución así como la medida de Intensidad de Turbulencia. Estas variables son clave para el diseño de turbinas y la planificación de parques eólicos.

Para validar la efectividad de las metodologías propuestas se han comparado los datos del lidar flotante con un lidar fijo y otras medidas de referencia. Se han desarrollado técnicas de procesado de datos (incluyendo primediado temporal adaptativo) y análisis estadístico clásico para establecer parámetros indicativos clave y así evaluar y mejorar la calidad de los datos recogidos. Estas técnicas se han aplicado tanto a datos brutos como corregidos para evaluar la capacidad de estas de reducir el impacto del movimiento en las medidas del lidar.

A lo largo de esta Tesis se han llevado a cabo tres campañas de medición: (i) *Tests de laboratory* para establecer los criterios de comparación entre lidar en movimiento con la referencia, así como tests preliminares para evaluar la viabilidad del marco carcdánico como solución para compensar el movimiento del lidar. (ii) El *testeo de una boya de prueba en condiciones marinas cercanas a la costa* para poder evaluar el comporatamiento de la boya en condiciones controladas de mar. (iii) Finalmente, la validación de la boya lidar funcionando en condiciones reales de mar durante una *campaña de validación* de 6 meses de duración en el Mar del Norte. Estas tres campañas de medición han brindado la oportunidad excepcional de evaluar y mejorar las diferentes soluciones para compensar el efecto del movimiento en el lidar.

L'objectiu d'aquesta Tesi és l'estudi d'un lidar doppler d'ona continua i el seu ús en el camp de l'energia eòlica marina. L'ús de lidars instal·lats en plataformes flotants tals com boies s'ha estudiat per mesurar el camp de vent per emplaçaments en alta mar. Aquesta tecnologia, desenvolupada en el marc del projecte NEPTUNE, resulta de gran interès pel sector de la indústria eòlica ja que ens permet obtenir dades amb una precisió similar a l'obtinguda amb màstils metereològics però amb una important reducció de costos que facilitarien la transició a una economia de baixes emissions de carboni.

L'objectiu pruncipal d'aquesta Tesi es centra en investigar diferents solucions capaces de reduir la influència del moviment de la superficie marina sobre les mesures d'un ludar flotant. Així, es plantegen i s'analitzen diferents propostes que van des d'una solució mecànica a algoritmes de post-processament. Primer, hem analitzat el comportament d'un marc cardànic (i.e. estabilitzador mecànic) per compensar el moviment d'un lidar Doppler instal·lat en una plataforma flotant. Seguidament, s'han desenvolopat tècniques avanades de filtratge per tal de minimitzar els efectes del movimient marítim sobre les dades de vent. Finalment, s'ha desenvolopat un simulador lidar de moviment per avaluar numèricament l'impacte de la plataforma flotante sobre la qualitat de les mesures. Aquestes tècniques de post-processat ens han permès millorar la qualitat de les dades, tant de les mesures d'alta ressoluci-temporal de la velocitat del vent com les mesures d'intensitat de turbulència, magnituds crítiques per al disseny d'aerogeneradors i parcs eòlics.

Per tal de validar la idonïetat de les metodologies proposades, les mesures del lidar en moviment s'han comparat amb les d'un lidar fixe de referència així com altres mesures de referència. S'han utilitzat tècniques de processat de dades (inclent el promitjat temporal adaptatiu i l'anàlisis espectral) i eines clàssiques d'anàlisi estadístic per tal d'evaluar els principals indicadors de rendiment i millorar la qualitat de les dades. Aquestes tècniques s'han aplicat a ldes dades en brut (i.e. afectades pel moviment) així com a les dades corregides permetant-nos determinar la capacitat de les metodologies proposades per reduir l'impacte del moviment.

Durant aquesta Tesi s'han realitzat tres campanyes de mesura. Aquestes campanyes inclouen: (i) *Tests de laboratori* per establir els criteris de comparació entre el lidar en moviment i el de referència, així com tests preliminars per avaluar la viabilitat del marc cardanic com a solució mecànica per compensar el moviment del lidar. (ii) *Estudi conceptual de la boia en condicions marines prop de la costa* per poder avaluar el comporatamient del lidar flotant en condicions controlades de mar. (iii) Finalment, s'ha dut a terme una *campanya validació* del prototip en condicions reals de funcionament en una campanya de 6 mesos al Mar del Nord. Durant totes aquestes campanyes de mesura s'ha tingut l'oportunitat d'avaluar i millorar les diferents solucions per compensar l'efecte del moviment en el lidar.

Contents

List of Figures

List of Tables

List of Acronyms

AEP Annual Energy Production.

CAPEX Capital Expenditure.

CIEMAT Centre for Energy, Environmental and Technological Research.

CoG Center of Gravity.

ECN Energy Research Centre of the Netherlands.

EIT European Institute of Technology.

FWHM Full Width at Half Maximum.

GNF Gas Natural Fenosa.

HWS Horizontal Wind Speed.

IMU Inertial Measurement Unit.

IREC Catalonian Institute for Energy Research.

KPI Key Performance Indicator.

LAT Lowest Astronomical Tide.

LIM Laboratory of Maritime Engineering.

LO Local Oscillator.

LOS Line-Of-Sight.

LT Local Time.

MD Mean Deviation.

MSE Mean Square Error.

OPEX Operation Expenditure.

OWA Offshore Wind Accelerator.

PCA Principal Component Analysis.

PdP El Pont del Petroli.

PiF Points in Fit.

RMSE Root Mean Square Error.

RSLAB Remote Sensing Laboratory.

RWE Rheinisch-Westfälisches Elektrizitätswerk.

SIMO Operational Maritime Engineering Solutions.

SV Spatial Variation.

SWE Stuttgart Wind Energy.

TI Turbulence Intensity.

TKE Turbulent Kinetic Energy.

TRL Technology Readiness Level.

UPC Polytechnic University of Catalonia.

VAD Velocity Azimuth Display.

VWS Vertical Wind Speed.

WD Wind Direction.

WTG Wind Turbine Generator.

Chapter 1

Introduction

Light Detection and Ranging (LiDAR or lidar) is becoming more and more widely used as a valuable tool for the wind energy market, as its capabilities and price are pushing forward the use of this technology as complement, or even alternative, for measuring the wind vector in a trustful way. This thesis addresses the suitability and capabilities of Doppler Continuous-Wave lidar and related signal processing tools in the context of wind-energy project NEPTUNE. This Chapter gives an overview of the efforts of UPC CommSensLab in the use of the Doppler-Lidar for offshore wind energy applications. Additionally, it proceeds to present the motivation, objectives and organization of this Ph.D. thesis.

1.1 Wind Energy

Wind energy has been developed in the last years to reach nowadays a significant level of maturity from the technological point of view and relevant importance regarding its impact in the global energy market. This energy source has some important advantages with respect to other sources as, between others, it does not produces CO_2 or other contaminants. It has also some counterparts, one of them, being the unpredictability of the wind (more in the short term but also in the long term). Therefore, to evaluate the economical viability of a site it is important to measure accurately the wind resource of a candidate location by correctly assessing its long term energy output and fitting the best wind generator in order to make the most of the particular conditions of the site.

These requirements give rise to a high demanding level concerning how the wind resource has to be measured (*International Electrotechnical Commission*, 1998). This standard establishes the cup anemometer as the most widely accepted sensor to measure the wind but the limitations of its use (e.g., met-mast installation and measurements heights) makes necessary to complement these measurements with other sources of data such as those coming from measurement points in nearby locations, global numerical models and, lately, the usage of remote sensing in the form of Sound Detection and Ranging (SoDAR) and lidar (*Rodrigo*, 2010).

There are different means of gathering wind data in offshore locations, such as metmasts, conventional weather buoys or Ocean Data Acquisition Systems (ODAs), radar, satellite data, numerical models, ... (*Rodrigo*, 2010) each one with its own advantages and disadvantages. However, the use of lidar (*International Energy Association*, 2007) (*Rodrigo*, 2010) (*Pichugina et al.*, 2011) is more and more being accepted as the best suitable remote sensing technology for offshore wind farms for several reasons:

- It is a *cost-effective* solution compared to the most-widely accepted data source, that is, the met-mast with cup anemometers. The installation of an offshore met-mast can easily reach millions Euros budget and requires long planning and construction. Lidar, both in nacelle, transition piece (base between the tower and the submerged structure) or in a floating buoy, are in the hundred-of-thousand-Euro range and are not so demanding regarding the soil, environmental constraints and time-frames.
- It is *flexible*, in the sense that it can easily be re-deployed in other locations (new resource assessment campaigns) or turbines (in case of power-performance tests).
- It is *reliable*. In the last years, commercially available wind lidars had widely been deployed around the world and had proven the reliability of its data, both as stand-alone or in complement of a met-mast. Besides, they are gaining acceptance between the industry due to its particular capabilities (simple installation, easily re-deploy, vertical wind profiling up to more than 200 m), specially for offshore applications (*Rodrigo*, 2010).

These advantages has caused a growing interest of the wind industry for lidar technology.

1.2 Offshore Wind Energy Market Outlook

Offshore wind energy industry has the challenge of reducing costs in the following years in order to achieve commercial competitiveness against other energy sources. In Fig. 1.1 we can see the Levelized Cost of Energy (LCoE) of the more common energy sources. For example, the LCoE baseline of offshore wind farms is around 8-14€cent/kWh (*Kost and Schlegl*, 2018) and this figure should be reduced in the following years to improve the implementation of wind farm in the seas.

Offshore wind projects are expensive and complex energy facilities, easily achieve thousand millions Euros budget and several years from the planning to final commissioning of the project. Consequently, the need of trustable data is of vital importance in different phases of the project, from the early beginning in the development phase, to assess to feasibility of the project, to the operation phase to validate the performance of the turbines, through the construction phase when is crucial to foresee the meteo-ocean conditions to schedule the works.

The cost of an offshore wind farm facility depends on several factors, some of the most important are the selected technology (e.g., rotor diameter, hub-height or rated power) and the depth and distance to shore of the site (*Associates*, 2017), and, here, there is the tendency of going further into offshore and to higher depths to, despite the costs increase, profit the higher wind speeds of these locations (Figure 1.2).

Figure 1.2 also evidences a trend of increasing the rated power of the Wind Turbine Generator (WTG) which implies higher rotor diameter and hub-height.

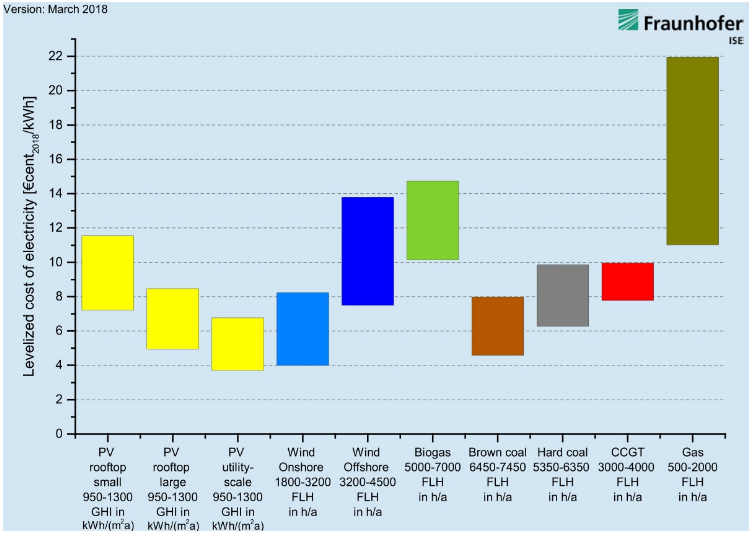

Figure 1.1: Levelized Cost of Energy for different energy sources, namely photovoltaic (PV), wind, biogas, coal and combined cycle gas turbine (CCGT) (*Kost and Schlegl*, 2018).

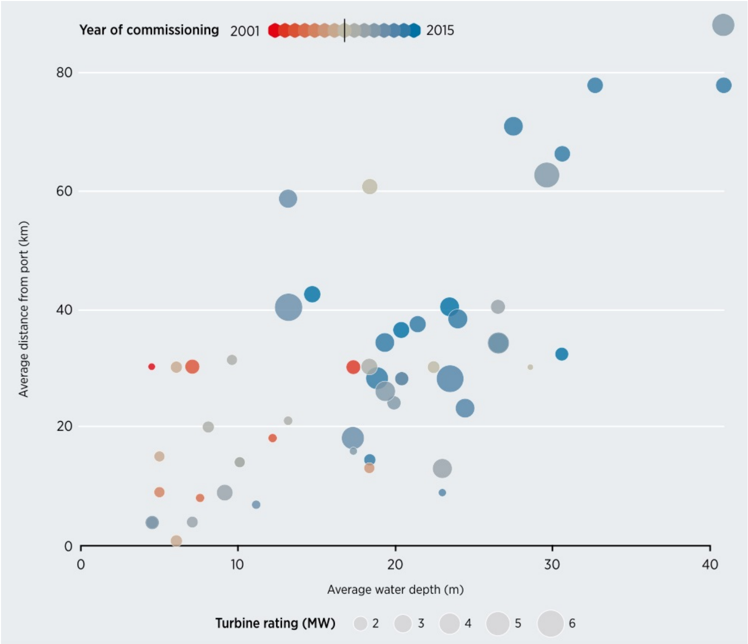

Figure 1.2: Offshore wind farms date (color), depth (X-axis), distance to shore (Y-axis) and WTG rated power (circle size) trend (*Ilas et al.*, 2018).

This trend of going to larger distances from shore is motivated by the interest of exploiting better locations with higher *capacity factor*, the ratio of actual energy produced over a period of time (usually one year) and the maximum possible power generated over that period. Fig. 1.3 shows the increasing trend in the capacity factor or both onshore and offshore wind farm. This increase in the capacity factor produces an increase the Annual Energy Production (AEP) and, therefore, the revenues.

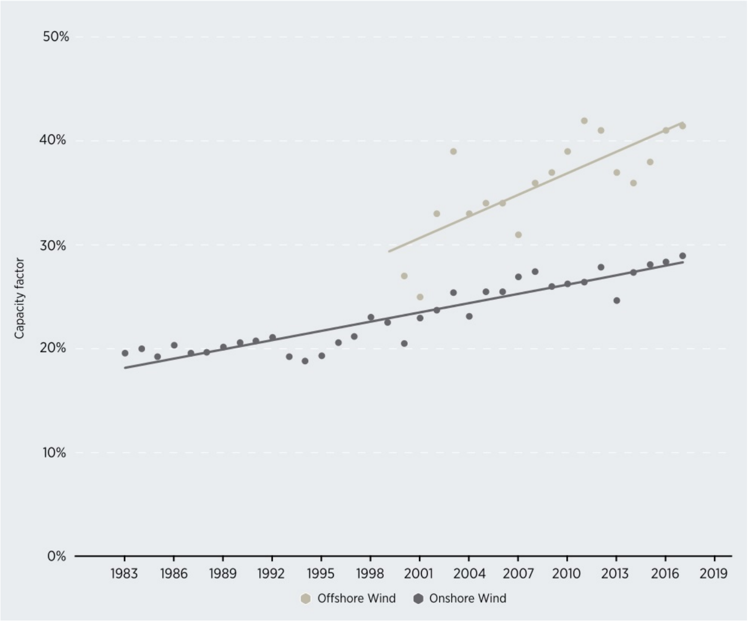

Figure 1.3: Capacity factor trend for both onshore and offshore wind farms between 1983 and 2018 (*Ilas et al.*, 2018).

Tabs. 1.1 and 1.2 present a wind-farm classification according to the main parameters with direct impact on costs and production, namely, WTG type and site type, as proposed in (*Associates*, 2017). In Tab. 1.1 are described the main characteristics of the selected site types of the classification along with the considered example of rated power of a generic wind farm. Tab. 1.2 summarizes main costs and the production items of several generic study-cases nowadays to present a picture of the current status of the market, and explains the tendency of increasing size and power of the wind turbines as, nowadays, Capital Expenditure (CAPEX) is more dependent on distance to shore than on the size of the wind turbines, but Operation Expenditure (OPEX) per MW decreases as the rated power of the turbine increases. For example, in Tab. 1.2, the 8-A-17 label type represents a wind farm with 8 MW WTGs in a site type A, near shore, in the year 2017. On the other hand, a 12-D-25 will be composed with 12 MW WTGs in far-to-shore site (type D) in the year 2025.

The current trend of increasing the rotor height (rated power) and, therefore, the spatial range required to measure the whole rotor swept area, and the distance to shore makes difficult the use of conventional met-masts and brings the necessity of using wind remote-sensing technologies, under the exigent criteria of the industry and in a cost-effective way.

The need of reliable and cost-effective solution is specially relevant in the resource assessment phase of the project, to evaluate the profitability of the chosen site, as well as for O&M planning or to measure power curves of WTGs.

Table 1.1: Classification of Wind Farms sites (*Associates*, 2017).

Site	**Type A**	**Type D**
Average water depth (MSL)	25 m	35 m
Distance to nearest construction and operation port	40 km	125 km
Average wind speed at 100 m above MSL	9 m/s	10 m/s
Farm size (MW)	500	500

Table 1.2: Summary of Baseline Costs parameters (*Associates*, 2017).

Type	**Parameter**	**8-A-17**	**8-D-17**	**10-A-20**	**10-D-20**	**12-A-25**	**12-D-25**
CAPEX	Development [€k/MW]	92	97	90	94	88	93
	Turbine [€k/MW]	1,003	1,023	1,030	1,051	1,049	1,070
	Structure [€k/MW]	489	590	449	531	379	476
	Electrical array [€k/MW]	50	51	44	46	37	37
	Construction [€k/MW]	341	360	279	295	212	221
OPEX	Operations [€k/MW/yr]	33	36	31	32	29	30
	Unplanned [€k/MW/yr]	43	57	36	44	29	32
AEP	Gross AEP [MWh/yr/MW]	4,599	5,119	4,692	5,209	4,842	5,363
	Losses [-]	17.50%	16.10%	16.90%	15.50%	15.90%	14.60%
	AEP [MWh/yr/MW]	3,794	4,294	3,901	4,402	4,072	4,582
	Capacity factor [-]	43.30%	49.00%	44.50%	50.20%	46.40%	52.3%

1.2.1 NEPTUNE project

NEPTUNE KIC InnoEnergy (*Schuon et al.*, 2012) project is a initiative of several partners from the energy and environmental communities which merges synergies together with the aim of develop cost-effective solutions for the offshore wind energy.

In 2011 the Catalonian Institute for Energy Research (IREC) in collaboration with the Polytechnic University of Catalonia (UPC) (Laboratory of Maritime Engineering (LIM) and CommSensLab), the Centre for Energy, Environmental and Technological Research (CIEMAT), the University of Stuttgart (through Stuttgart Wind Energy (SWE)), Gas Natural Fenosa (GNF) and Operational Maritime Engineering Solutions (SIMO), led the project NEPTUNE which lasted up to the end of 2014. The project successfully developed (i) the EOLOS buoy prototype, consisting on a floating Doppler offshore lidar system and processing tools specially designed to yield high-quality wind data, (ii) a coupled wind, wave, and sea-current model and analysis tool (forecast/hindcast) for wind-resource assessment and (iii) specific spin-offs and patents related to previous points (i-ii) alone.

The main goal of the EOLOS lidar buoy was to develop a fully commercial system capable of measuring wind over the sea surface up to 200 m as an alternative of the more expensive sea-bottom-fixed metmast. The system was also able to measure other relevant parameters (e.g., wave and sea currents) for the development phase of an offshore wind farm (*KIC InnoEnnergy*, 2015).

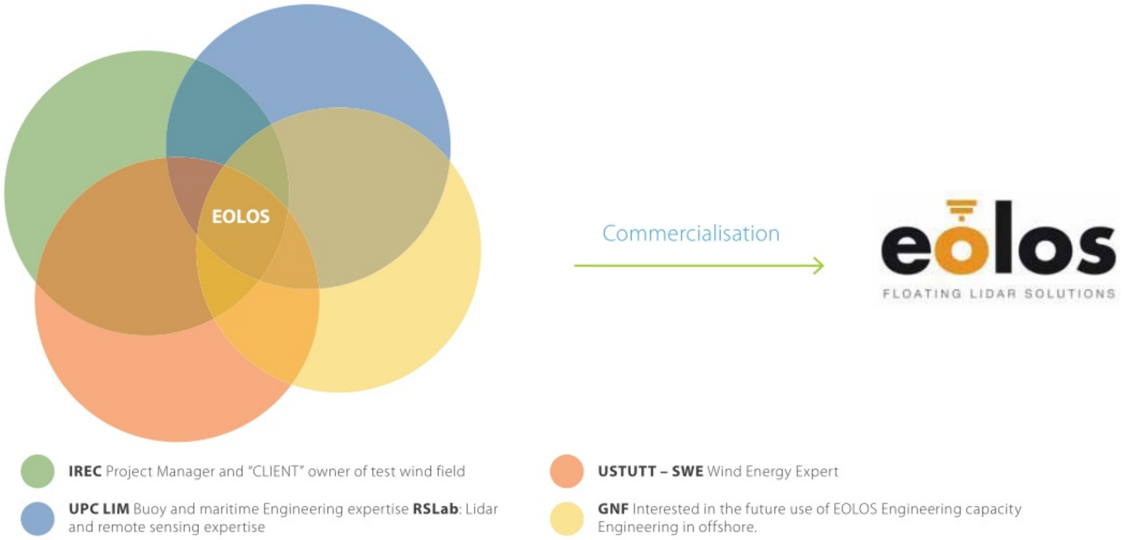

Figure 1.4: NEPTUNE project partners and EOLOS Spin-Off diagram (*KIC InnoEnnergy*, 2015).

At the time of the project there were not commercial floating lidars and the only systems available were in a pre-commercial phase. Therefore, one of the challenges of the project was to develop a fully functional commercial system that could withstand the rough conditions of maritime environment and capable of measuring wind field magnitudes with accuracy required by the industry standards. To that aim a set of measurement campaigns were planned to assess suitability of the developed buoy: The first in the UPC laboratory in Barcelona and the second with a proof-of-concept buoy in near-shore conditions in Badalona.

The consortium of the project, in cooperation with KIC InnoEnergy, fostered the creation of a spin-off to offer the developed system to the market: the EOLOS FLS company, which was awarded with the Innovations Award 2015 of the European Institute of Technology (EIT). Additionally it was selected to participate in KIC InnoEnergy Highway® that supports the enterprise creation.

The EOLOS lidar buoy was included in the Offshore Wind Accelerator (OWA) project of the Carbon Trust to participate in a 6-month validation campaign against and offshore metmast in IJmuiden, North Sea. In this campaign, with the collaboration of Rheinisch-Westfälisches Elektrizitätswerk (RWE) and the third party validation of Energy Research Centre of the Netherlands (ECN), the EOLOS FLS200 buoy fulfill all the Key Performance Indicators (KPI) requirements (*Carbon Trust*, 2013) and achieve the final stage of the pre-commercial system, Technology Readiness Level (TRL) 6.

1.3 Main Objectives

As mentioned, the Ph.D. thesis is aimed at *understanding and improving the capabilities of Doppler wind lidar systems in the frame of offshore wind energy.* Specific objectives are:

- *Objective 1: Wind-lidar signal processing and performance assessment.*- This objective is two fold: First, focus is on the definition of an end-to-end signal-processing methodology ranging from the collection of lidar-and-cooperative-sensors raw data (level-0 data) and its pre-processing (level-1 data) to the output of performance indicators (level 2 data).

- *Objective 2: Motion compensation.*- Here, the Ph.D. is to tackle sea-motion compensation at Velocity Azimuth Display (VAD) level. Towards this aim, an advanced VAD simulation algorithm is developed to analyse and deconvolve the effect of sea motion on the VAD wind-vector retrieved by the floating lidar buoy.

- *Objective 3: Test campaigns.*- Test campaigns are a validation backbone transversal to the whole Ph.D.. Three campaigns are considered: First, the Ph.D. starts from basic LIM-UPC laboratory tests, where a mechanical-motion simulation platform has been used to simulate the effect of a "floating" lidar in a laboratory environment. Second, El Pont-del-Petroli (PdP) measurement campaign at Badalona (Barcelona, Spain) is to provide an outlook of the first near-shore results at Badalona pier. Finally, the third campaign at Ijmuiden (North Sea) is to compare EOLOS floating-lidar buoy final prototype against a highly instrumented, 100-m tall, offshore met-mast, which is used as reference, during a measurement period of 6 months.

All in all, the proposed objectives are aligned with European Project NEPTUNE and, perhaps, its continuation.

1.3.1 Objective 1: Signal processing approach

This section describes lidar and cooperative sensors data and different methods and processing tools to be used to understand and improve the lidar accuracy in gathering wind speed, in general for the continuous-wave lidar ZephIR 300® and particularly in a floating platform. During this thesis these methods will be developed, tested, improved and systematized to produce a systematic procedure to assess the precision of continous-wave Doppler lidar measurements in the wind vector calculation.

The data processing of the lidar and complementary sensors includes:

- *Raw data* .- Main instruments involved in NEPTUNE measurement test campaigns (detailed in Chapter 2) are two lidar units Zephir300® and Inertial Measurement Units (IMUs). The latter provide time series describing the system motion and attitude. In the last measurement campaign, described in Chapter 5, sonic anemometer on an offshore metmast are also used.

- *Pre-processed data* .- It is necessary to prepare the lidar data to be evaluated: data synchronization is necessary to compare high resolution data from the two lidar units, therefore several algorithms are tested to perform this operation, Delay correction and Constant timestamp algorithms will be applied to achieve the necessary data synchronization. Advanced algorithms are applied to movement and internal status data to assess the quality of the data and to evaluate the error against these parameters. Windowing of the signal (low pass filtering) is applied to reduced the movement induced variations of Horizontal Wind Speed (HWS) measured by the floating lidar and generate compensated data. This methodologies are described in Chapter 4.

- *Error assessment* .- Main indicators and techniques used to assess the performance when comparing wind-desired quantities from both lidars ("fixed" or "reference" lidar, and "moving" or "floating" lidar) as well as motion compensation algorithms will be described and applied to different measurement campaign. These techniques include, but are no limited to Scalar statistical indicators, (Bias, Root Mean Square Error (RMSE), ...), scatter plot analysis (Slope, offset, determination coefficient, ...), or other more specific requirements (KPI of the Carbon Trust OWA roadmap for the commercial acceptance of floating Lidar (*Carbon Trust*, 2013)). This indicators are to be defined in Chapter 2.

1.3.2 Objective 2: Motion compensation

With the aim of adapting the lidar to measure in a floating platform, solutions to reduce the impact of lidar movement on the wind-speed measurement become necessary. This can be carried out using different approaches: (1) motion-compensation using a cardanic frame (2) motion-compensation at post-processing level and (3) motion-compensation at VAD level. This Ph.D. will evaluate the impact of each one of these solutions but will concentrate efforts on (3).

1. *Motion-compensation using a cardan frame* .- The Gimbal or cardan frame designed, tested and integrated with the lidar is a mechanical solution that allows free platform movement while keeping the lidar virtually stand still pointing to the zenith. Chapter 3 describes several experiments carried out to assess the performance of this solution.

2. *Motion-compensation at post-processing level* .- Window averaging of the HWS, is a low-pass filter technique that enables to filter out unwanted high-frequency components such as those caused by the motion of the floating lidar (Chapter 4).

3. *Motion-compensation at VAD level* .- To analyse and deconvolve lidar motion in the radial velocity measured along each Line-Of-Sight (LoS) given attitude data (pitch and roll information) a VAD simulator is to be developed (*Bischoff et al.*, 2015) (*Gottschall et al.*, 2012a). This methodology will be developed in Chapter 6.

1.3.3 Objective 3: Test campaigns

- LIM-UPC Test campaign

  The LIM - UPC test campaign took place at UPC Campus Nord, Barcelona, October 19th 2012 - February 26th 2013. The campaign was aimed at studying the correlation degree between two CW Doppler lidar units (Zephir300®) namely, the "fixed" and "floating" lidar. The so-collled "floating" lidar was mounted on a mechanical *motion-simulator platform*, which reproduced pitch and roll angular movements similar to the one that the "floating" lidar is to suffer when deployed in the water. A further goal was to evaluate the performance of *cardanic frame* as mechanical motion compensation device. The possibility to test the cardanic frame under quasi-real sea states in motion platform allows to work out most adequate solutions without need to build and deploy costly equipment in real-sea conditions.

Fig. 1.5a shows the location of LIM/UPC premises where the test campaign was carried out. Black dots denote the position of the "fixed" and the "floating" lidars and, light red circles the lidar scanning cone projection at 10 m in height. Fig. 1.5b shows the experimental setup.

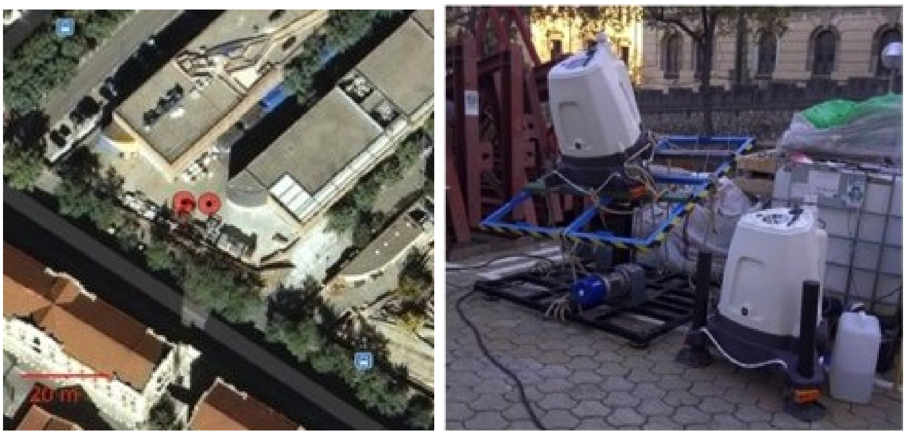

Figure 1.5: LIM - UPC test campaign. (a) Plan view of experimental set up at LIM/UPC premisses (b) Experimental set up showing the reference "fixed" lidar and the moving "floating" lidar on the motion simulator platform.

- PdP Test campaign

  The PdP campaign (Badalona, Barcelona, May 2nd 2013 - July 26th 2013) was aimed first, at examining the correlation degree between the two Zephir300š lidar when retrieving wind-related parameters, namely, HWS, Wind Direction (WD) and Turbulence Intensity (TI), and, second, to infer tips for error reduction and overall improvement of the final specifics of the definitive lidar buoy prototype which is to be deployed in the commissioning phase in the North Sea.

  PdP (Fig. 1.6) was a former fuel supply pier next to Barcelona, outgoing from the coast some 250 m into the sea. It was reshaped in 2008 by the town council of Badalona as an in-sea promenade. Together with this, an agreement with LIM-UPC made possible to convert it also into a scientific facility with electrical and communications network distributed all along its length to support oceanographic experiments.

Figure 1.6: PdP test campaign site. (a) Location of the test site near Barcelona coast (Badalona). Red dots denote the position where the "fixed" and "floating" lidars have been placed. (b) Plan view PdP test site. (c) Meteorological tower and EOLOS Doppler lidar buoy.

As fixed instrumentation, it includes a full set of meteorological and oceanographic sensors and, during the length of the campaign, the fixed CW Doppler lidar Zephyr 300 was temporary installed at the mid level of the tower to be used as reference wind measurement. The proof-of-concept buoy, integrates the "floating" Zephir300® lidar as well as the two IMUs to record buoy movement. The cardan was integrated into the buoy structure so different dumping configuration were tested during the campaign.

- IJmuiden offshore assessment campaign

  The final phase of the development of EOLOS lidar buoy is to prove its commercial suitability for the demanding requirements of wind industry for wind measurements in an offshore location. NEPTUNE's project spin-off company, EOLOS FLS, was in charge of this final phase and was selected by the Carbon Trust to develop a pilot validation trial against RWE's met-mast in IJmuiden, the Netherlands.

  This pilot validation trial took place on the Meteorological MetMast IJmuiden, an offshore facility operated by Energy research Centre of the Netherlands (ECN). IJmuiden is a port city located in the mouth of the IJ, in the province of North Holland, in the Netherlands. The IJmuiden metmast, owned by RWE and operated and maintained by Energy research Centre of the Netherlands (ECN), is located 85 km off-coast of the Netherlands (insert in Figure 1.7a), has sensors up to 87m height and the sea-depth at the test-site facility (Fig. 1.7b) is around 28m (*Werkhoven and Verhoef*, 2012).

  The first commercial prototype developed in the project NEPTUNE, the EOLOS FLS200 buoy, was assembled and tested at LIM-UPC facilities in Barcelona (Spain), Dec. 2014 to Jan. 2015. Later, was transported to the Netherlands and commissioned at 200m range of the IJmuiden metmast to perform the pilot validation trial from March to October, 2015. The results of this campaign are presented in Chapter 5.

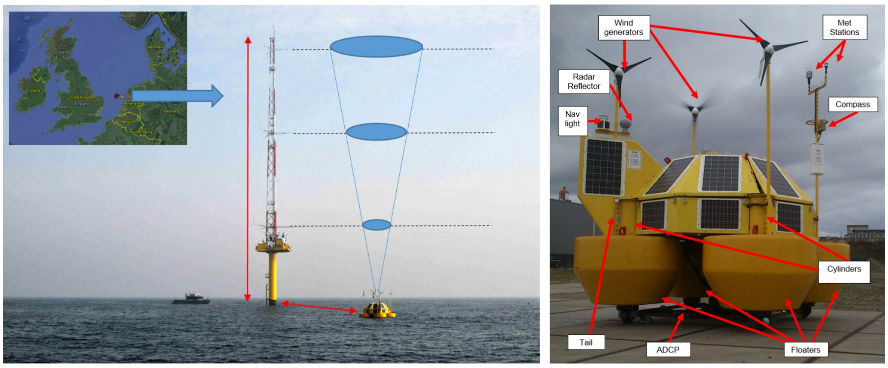

Figure 1.7: (a) IJmuiden met-mast location and image. (b) The EOLOS lidar buoy.

1.4 Organization Of The Ph.D. Thesis

This Ph.D. Thesis is organized as follows:

- ***Chapter 1*** describes the motivation and main objectives of this Ph.D. and in relation to the NEPTUNE project and the state of the art of offshore wind energy.

- ***Chapter 2*** reviews lidar and radar atmospheric remote sensing foundations including the VAD algorithm to retrieve the wind vector.

- ***Chapter 3*** studies the mechanical compensation of the lidar movement by means of a cardan frame. Firsts experimental results are discussed.

- ***Chapter 4*** presents different signal processing and filtering techniques to refine offshore wind-measurements and to compensate for buoy motion-induced errors. This is discussed in the context of PdP near-shore measurement campaign.

- ***Chapter 5*** describes the commissioning phase at IJmuiden, North Sea, which has enabled to reach the highest TRLs before the final go-ahead to market. Therefore, to become a wind-industry-accepted trustworthy solution to measure the near offshore wind resource.

- ***Chapter 6*** has a two-fold approach: On one side, it gives the foundations of the motion simulation conceived to evaluate the effects of offshore lidar motion in wind measurements. On the other side, the motion-induced error is mathematically estimated using statistical theory and basic motional parameters input to the simulator.

- ***Chapter 7*** gives concluding remarks along with future recommendations.

Chapter 2

Doppler lidar in offshore wind energy

This Chapter presents the basics of lidar foundations with focus to its application in the wind energy industry. Additionally, it gives an introduction to the main methodologies used to assess the quality of the data.

2.1 Wind Lidar Foundations

2.1.1 History

A lidar is a device that allows to determine the distance to a target by illuminating this target with a laser light source and gathering the backscattered signal with a sensor. The term lidar is an acronym for Light Detection And Ranging and it was chosen as an analogy with the radar acronym. While radar devices emit radio waves, lidars use light (from ultraviolet to near infrared) to illuminate the target to be studied.

The invention of the Lidar can be dated in the beginning of the 60s just after the development of first lasers. The combination of laser light sources and appropriate sensors and data acquisition electronics made possible to measure distances to targets by measuring the time of flight of a photon from the emitter to the target and come back.

A relevant milestone achieved with lidar technology was the measurement of the distance between the Earth and the Moon (*Smullin and Fiocco*, 1962), by pointing a laser to the moon and measuring the backscattered light. Later on, and during the Apollo 15 mission (1972) a laser altimeter was used to map the surface of the moon. `https://www.lpi.usra.edu/lunar/missions/apollo/apollo_16/experiments/la/index.shtml`

One of the first applications for lidar technology came in meteorology to measure properties of the clouds (*Goyer and Watson*, 1963). The key idea of lidar was firstly introduced by (*Synge*, 1930), who proposed the use of powerful searchlights, consisting in a highly bright and collimated beam which can be pointed to any direction with the help of a parabolic reflector, to probe high layers of the atmosphere.

The use of lidar for wind energy applications was firstly introduced by (*Hardesty and Weber*, 1987), 1987 as well as by (*Vaughan and Forrester*, 1989). In that time and with the available technology, it was difficult to fulfill the industry standards. From 90s and coinciding with the growth of wind energy industry and the development of all-fibre lidars, this technology has been stablished as a valuable tool for wind assessment more and more accepted in the wind industry.

2.1.2 Basic principles

As mentioned before a lidar is a device used to determine the distance from the emitter to the source by using a laser beam with both high temporal and spatial resolution. Typical temporal and spatial resolution can reach 1 m and 1 s respectively.

Lidar technology is based on the strong optical interaction between light and atmospheric molecules or aerosols, occurring when the laser wavelength and the size of the target are comparable (i.e. $\lambda \sim r$). Therefore, and in order to suit the target size, a wide range of wavelengths (from about 10 μm to 250 nm) are available depending on the size of the objects to be measured. Lidars can detect and characterize different targets including forest canopy, rocks, chemical compounds, clouds, rain droplets and aerosols. Multi-wavelength lidar systems allow to retrieve physical and micro-physical properties of atmospheric aerosols since different backscattering interactions such as Rayleigh scattering, Mie scattering, Raman scattering, enable to identify wavelength-dependent changes in backscattered signal.

Independently of the specific lidar technology, lidar systems consist of the following basic components (see Fig. 2.1a) (1) a transmitter, laser; (2) the transmitter optics; (3) Receiver optics; (4) a detector; and (5) the electronic system for data acquisition/processing. Additional subsystems can be added for particular applications.

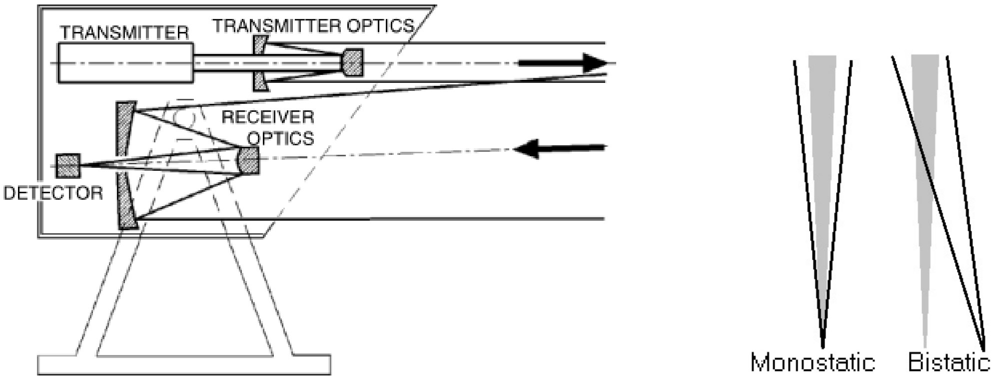

(a) (b)

Figure 2.1: (a) Essential optical components of a lidar system (*Fujii and Fukuchi*, 2005). (b) Monostatic and bistatic lidar types: In gray the transmitted beam and in black line the field of view of the receptor.

2.1.3 Types

Depending on the detection needs, lidars can be classified as *incoherent* or *coherent*. Incoherent or direct energy detection basically measures amplitude changes on the backscattered signal while coherent detection measures Doppler shifts or changes in phase on the backscattered signal.

Incoherent lidars (e.g., backscatter and Raman lidars) are mainly used in atmospheric science to measure atmospheric parameters such as aerosol concentration and particle properties (extinction coefficient, backscatter coefficient, depolarization), cloud height, cloud layers, temperature and humidity, and trace gas concentration (ozone, methane, nitrous oxide).

Doppler lidars are mainly used to measure the wind speed by measuring the Doppler shift resulting from the component of target velocity along the beam (or LoS) direction. In coherent detection the backscattered signal is mixed with a Local Oscillator (LO) to measure the Doppler shift (*Sonnenschein and Horrigan*, 1971) while in direct detection this shift is calculated by an optical frequency analyser (*Fujii and Fukuchi*, 2005). The Doppler shift and the velocity along the LoS are related as follows:

$$f_d = -\frac{2v_r}{\lambda} \tag{2.1}$$

where v_r is the radial velocity (positive means moving away from the lidar) and λ is the sounding wavelength (1-10 μm wavelength, where the optical interaction is stronger).

In order to measure the Doppler shift with coherent Doppler lidars, two different configurations are available in the market. Homodyne and heterodyne detection schemes can be used to mix backscattered signal with the local-oscillator (LO) reference signal. It is well known that when mixing two harmonic waves oscillating at two slightly different frequencies the resulting intensity shows beats. The resulting intensity can be written as follows:

$$\begin{aligned} i(t) &\propto (E_{LO}cos(\omega_{LO}t) + E_s cos(\omega_s t))^2, \\ i(t) &\propto (E_{LO}^2 + E_s^2) + 2E_{LO}E_s cos(|\omega_s - \omega_{LO}|t), \end{aligned} \tag{2.2}$$

where E_{LO} and ω_{LO} are the LO electric field amplitude and frequency respectively and E_s and ω_s are the backscattered field amplitude and frequency respectively. Therefore, the Doppler shift can be written as:

$$f_d = 2\pi|\omega_s - \omega_{LO}| \tag{2.3}$$

In the homodyne configuration the backscattered signal is directly mixed with the LO and usually only the magnitude of the Doppler shift can be retrieved but not its sign. This causes an ambiguity in the detection of the Doppler shift since both positive (radial velocity towards the lidar) and negative Doppler shifts (away from the lidar) cannot be distinguished from one another (i.e., the resulting beating frequency is the same). In the heterodyne configuration the return signal is mixed with the LO which is frequency-shifted. Therefore, both positive and negative Doppler shifts can be detected relative to the frequency shifted LO reference.

Depending on the relative position of the transmitter and the receiver, lidars can be classified as *monostatic and biaxial.* While in monostatic configuration both the transmitter and the receiver optics share the same optical axis, in biaxial configuration both transmitter and receiver optics have independent optical axis (Fig. 2.1b).

Finally, another possible classification for lidars is according to the emitted signal. Lidars can be classified as *pulsed* or *continuous wave (CW).*

In *pulsed lidar systems*, the time of flight is used to discriminate between returns from different distances. Range information is obtained as half of the time of flight, between the emission time and the time bin of interest (also called "range gate" or "range bin" because of the time-space duality). The final spatial resolution is given by length of the laser pulse, the acquisition time, and subsequent post-processing.

In *CW lidar systems*, light is continuously emitted and focused around a specific height or volume. Therefore, CW systems have to sequentially focus from one height to the next in order to gather the wind velocity in an atmospheric vertical column, whereas in pulsed systems all atmospheric information is gathered on the same backscattered optical pulse (each range bin stands for a specific height). In CW lidars, the spatial resolution is not uniform. Under this technology the spatial resolution depends on the measurement distance (R) and the laser-beam radius at the output lens (A) and is given by:

$$\Gamma = \frac{\lambda R^2}{\pi A^2} \tag{2.4}$$

In this Thesis we have used the ZephIR 300 Lidar consisting in an all-fiber monostatic homodyne CW lidar.

2.1.4 Velocity Azimuth Display

As mentioned in previous section, Doppler shift enables the retrieval of the radial (or LoS) velocity. In order to gather the three components of the wind (i.e., the wind vector) a conical scan with multiple LoS measures is required. Although the minimum number of LoS measures per scan is three (i.e. a system of three equations with three unknowns must to be solved), in CW lidar 50 LoS with a conical tiliting angle of 30 deg are analysed at each scan. The redundancy on the measured LoS allows the use of the Velocity Azimuth Display (VAD) algorithm.

The VAD algorithm is one of the most used approaches to calculate the wind vector from a particular height from the ground ((*Banakh et al.*, 1995), (*Fujii and Fukuchi*, 2005)). The schematic geometry for the VAD algorithm is shown in Fig 2.2

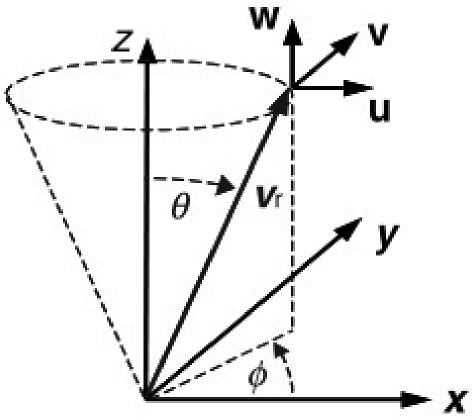

Figure 2.2: Schematic of the geometry of the VAD conically scanning technique. Modified from *Fujii and Fukuchi* (2005).

Each radial velocity, $\mathrm{V_r}$, can be expressed as the dot product between the wind vector, $\overrightarrow{\mathrm{V}} =< u, v, w >$ and the radial unitary vector, $\hat{r}$:

$$V_r[\phi(t)] = \hat{r}(t) \cdot \overrightarrow{\mathrm{V}} = v_H \; sin(\theta) \; cos[\phi(t) - \phi_0] + w \; cos(\theta), \tag{2.5}$$

Being ϕ_0 the angle of the HWS, v_H over the X-axis. In this representation the components of the wind vector are:

$$\begin{aligned} u &= A \; cos(\phi_0) \; csc(\theta), \\ v &= A \; sin(\phi_0) \; csc(\theta), \\ w &= A_{OS} \; sec(\theta), \end{aligned} \tag{2.6}$$

being $v_H = \sqrt{u^2 + v^2}$ and $A = v_H \; sin(\theta)$. To understand this methodology is useful to represent the LoS velocities as a function of the azimuth angle which gives name to the VAD methodology. Fig. 2.3 gives an example of this representation applied to a synthetic wind vector $\overrightarrow{\mathrm{V}} = < 0, \; 1, \; 0 > \; [m/s]$ as it would be seen by a ZephIR 300 lidar, which performs 50 LoS measurements (black dots) every second, i.e., in one scan.

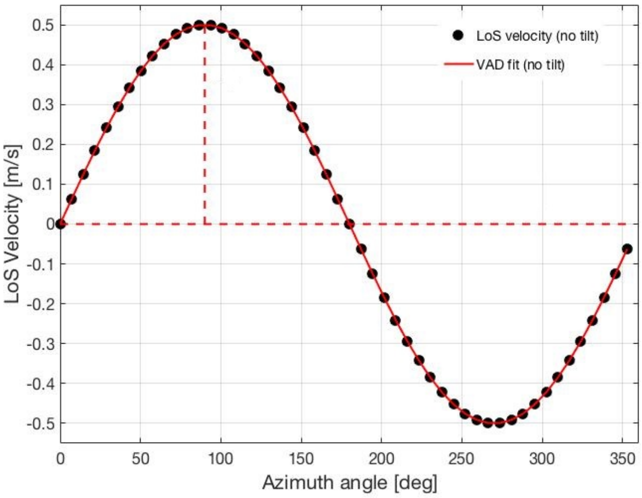

Figure 2.3: VAD representation of the LoS velocity (Y-axis) as a function of the azimuth angle (X-axis) with no lidar inclination. Synthetic values (black dots) and sinusoidal fit (red trace). A is the amplitude of the sinusoidal function, A_{OS} is the vertical offset and ϕ_0 the horizontal offset of the cosinus.

2.2 Present Status Of Doppler Lidar In Wind Energy

2.2.1 Commercial lidars

Due to the capabilities of lidar technology, wind industry, specially offshore, is using more and more Doppler wind lidars to measure wind. Some of the most widely used commercial devices are the ZephIR 300, from ZephIR lidar, and the Windcube, from Leosphere. Main characteristics of such devices are presented in Table 2.1, that shows that main differences between the two devices is the measurement principle, one being CW and the other Pulsed.

Parameter	**ZephIR 300**	**Wincube V2 offshore**
Measurement Principle	Continuous-wave	Pulsed
Detection principle	Homodyne	Heterodyne
Default Cone angle	30 deg	30 deg
Range	10 - 200 m	40 - 200 m
LoS per scan	50 LoS/scan	4 LoS/scan
Temporal Resolution	1 s/scan(one height)	1 s/scan (all heights)
Probe length	0.07 m at 10 m and 7.7 m at 100 m	27 m
Maximum Number of heights	10	12
Speed Accuracy	<0.5%	0.1 m/s
Speed range	1 - 70 m/s	0 - 60 m/s
Direction accuracy	<0.5 deg	<2 deg
Laser wavelength	1.5 μm	1.5 μm
Laser power	1 W	10 mW MO + 200 mW
Eye Safety (IEC 60825-1)	Class 1	Class 1
IP rating	IP67	IP67

Table 2.1: Comparative between ZephIR 300 and Windcube V2.

The ZephIR 300 is a continuous-wave (CW) focused Doppler lidar system specially adapted for offshore environments. It is widely used in the wind industry and has shown its trustability in deployments and verification processes to assess the quality of its data (*Mangat*, 2016). The system is able to profile the wind up to more than 200 m in height by using the VAD scanning technique (*Fujii and Fukuchi*, 2005). The lidar can measure at a user-defined set of heights between 10 m and 200 m in steps of 1 m. Due to the laser and optics characteristics of the lidar, it exhibits a height-dependent spatial resolution (e.g., 15 m when focusing at 100 m in height). The lidar achieves 1-s time resolution (when not refocusing) by using 50 LoS beams per second. It is worth noting that the measurement is not perfectly uniform (this point will be further discussed in Section 4.3.)

2.2.2 Applications

The main application of the wind-lidar technology is to assess the adequacy of a candidate site for offshore wind-farm installation. Towards this aim, the main parameter being used is the mean HWS, which is directly related to the wind energy that can be gathered in the candidate site. However, to evaluate the suitability of a measurement technology, a critical parameter is the uncertainty of the AEP, which depends not only on the technology but also on the methodology used to perform this calculation.

Thus, Tab. 2.2 presents some typical values for on-shore wind facilities. Considering that *wind flow modeling* contribution can be neglected, as the topography is not considered relevant in offshore wind, the most important parameter is the *wind shear*. The latter is not usually well resolved in conventional anemometry with a metmast. The influence of *wind shear* can be crucial for studying atmospheric conditions specially for offshore sites, where turbine blades can reach heights above 150 m and, therefore, there is risk of low-level jets ((*Bonner*, 1968) (*Zhang et al.*,

2006) (*Nunalee and Basu*, 2014).) that cannot be detected by other measurement technologies, such as cup anemometers in conventional metmasts.

Uncertainty Sources	**Mean**	**Max**	**Min**
Field Verification	0.5%	1.0%	0.2%
Measurements	2.4%	4.8%	1.6%
Long-Term Average	3.2%	4.8%	2.1%
Evaluation Period Wind Resource	1.9%		
Wind Shear	2.6%	6.4%	0.0%
Wind Flow Modeling	4.0%	8.0 %	2.4%
Wind Speed Frequency Distribution	1.0%	1.5%	0.6%
Total Plant Losses	3.5%	4.8%	3.2%
Total Energy Uncertainty	7.5%	13.5%	5.2%

Table 2.2: Typical Energy Production Uncertainty Values (*AWS Truepower*, 2014).

Wind industry facilities are usually expensive projects and some parts of the warranties and assurances of a project usually relies in the verification of the power performance tests of some turbines. In onshore industry, there is quite robust methodology used for these validation but it requires a metmast cup anemometer (*International Electrotechnical Commission*, 1998). These requirements can be very expensive for offshore application, or even impossible for certain offshore sites, so wind lidar provides a solution, specially now that its use is foreseen to be accepted in the next IEC Standard for Power Performance verification (*International Electrotechnical Commission*, 1998), by using nacelle lidar or floating systems.

Besides, wind-lidar could also be a great tool for other applications such as detection of *yaw mislignment* (i.e., the angular offset between Wind Direction (WD) and wind turbine orientation), and monitoring general atmospheric conditions with a view to evaluate or manage on-site operations. Some proofs of industry interest in lidar technology are:

- Expert group study of recommended practices for the use of lidar for resource assessment (*Clifton and Courtney*, 2013)
- The activities of the International Energy Agency in the Annex 32 (*Courtney et al.*, 2012).
- The Carbon Trust, through the OWA, to provide guidelines for the usage and commercial acceptance of floating lidar devices (*Carbon Trust*, 2013).

2.2.3 OWA roadmap

The OWA is a programme fostered by the Carbon Trust that aims to bring the offshore wind energy competitive with conventional energy generation. It has also the additional objective to provide industry standards for the industry, health and safety. OWA partners are offshore wind developers that account for most of Europe's offshore installed wind capacity.

Two main activities of the interest of this Thesis has been developed by the OWA: (1) Floating lidar trials, as the one described later in Chapter 5, to validate in-situ the accuracy of floating lidars versus conventional anemometry. (2) Floating lidar roadmaps and Recommended Practice, that serves as guidance to the industry about the use of floating lidar.

One of this documents “Roadmap to Commercial Acceptance of Floating LIDAR” (*Carbon Trust*, 2013), presented in 2013, establishes tests should a floating lidar conduct to have the acceptance from the industry. In particular, defines the phases of maturity of a system (*Baseline*, *pre-commercial* and *commercial*) and the milestones to go from one phase to the other.

This document recommends a successful 6-months pilot validation trial of floating lidar versus a metmast to reach the *commercial* qualification. The recommendations define the KPIs the HWS, the WD and the Data Availability should fulfill to prove the accuracy of the measurements.

2.3 Error Assessment And Key Performance Indicators

In this Section we introduce the statistical indicators used to assess the measurement errors from the moving lidar with respect to a reference which can be either a fixed lidar or a reference metmast. Those statistical parameters are going to be evaluated for the three main wind variables analysed during this thesis which are, HWS, Vertical Wind Speed (VWS), and WD.

2.3.1 Statistical error indicators

Main indicators used to assess performance when comparing wind variables measured simultaneously from both lidars (i.e., by the “fixed”or “reference” lidar and by the “moving” or “floating” lidar) or from metmast and moving lidar, are inherited from classic statistics.

- *Differential Error* .- The differential error in a measurement is defined by the difference between the measured quantity and the considered reference or correct value, mathematically:

$$\epsilon_X = X_{measured} - X_{reference}, \tag{2.7}$$

- *Bias o Mean Deviation (MD)*.- The bias of an estimator is the difference between an estimator's expected value and the true value of the parameter being estimated. It is obtained as the mean value of the Differential Error. In present work, the difference between the value of a wind variable measured by the “floating” lidar and the true value measured by the “reference” lidar

$$Bias = \frac{\sum_i^N (X_{measured} - X_{reference})}{N} = \frac{\sum_i^N \epsilon_X}{N} = \bar{X}_{measured} - \bar{X}_{reference}, \tag{2.8}$$

- *RMSE* .- The Root Mean Square Error (RMSE) of an estimator with respect to an estimated parameter is defined as the square root of the Mean Square Error (MSE). RMSE measures the average of the squares of the "errors". Formally,

$$RMSE = \sqrt{\frac{\sum_{i=1}^{N}(X_{measured} - X_{reference})^2}{N}}, \tag{2.9}$$

where N is the number of measurements.

The MD gives an estimation of the systematic error, equivalently, the amount of bias, while the RMSE is the quadratic mean of differences, with an ideal value of 0 indicating a perfect fit.

- *scatter-plot analysis.* Concerning scatter-plot analysis, three parameters related to the linear fit between v_{moving} and v_{ref} are computed to assess their correlation degree: slope and offset of the straight line fit and the coefficient of determination, ρ^2. Both standard linear regression (eq. 2.10), i.e., with the intercept term - so called in this Thesis "offset term"-, and regression through the origin (eq. 2.11), i.e., without the offset term, will be used im this Thesis:

$$y = ax + b, \tag{2.10}$$

$$y = ax, \tag{2.11}$$

2.3.2 Key Performance Indicators

The above defined error indicators have to fulfill the quality requirements established by the wind industry. The confidence thresholds, or KPIs, which provide acceptance criteria for the measured magnitudes are establish in the Carbon Trust (2013) roadmap (*Carbon Trust*, 2013) report in a 10-min basis.

In this thesis we are going to consider errors not only at 10-min time scale but also at 1-s time scale. As it can be seen from Tab. 2.3, acceptance criteria depend on the time resolution (1-s or 10-min) of the acquired data. While 10-min criteria come from (*Carbon Trust*, 2013), 1-s criteria come from the authors under the general guideline that acceptance criteria under 10-min average interval must be, in general, stricter than under 1-s basis.

These KPI provided the quantitative criteria to be used in the different measurements campaign of the project. For example, in a given period of study the 1-s HWS will be considered accurate if it fulfills each one of the KPIs for this variable. For example, in the regression analysis, the slope should be between 0.96 and 1.04, the offset below 3% of the mean value of the mean HWS (in the period of study) and the coefficient of determination greater than 0.95.

Table 2.3: Acceptance criteria for 1-s and 10-min data: KPIs (adapted from (*Carbon Trust*, 2013)). $v_{ref,mean}$ is the mean speed of the reference instrument.

KPI	**1-s**	**10-min**
Mean HWS slope, m	0.96-1.04	0.98-1.02
Mean HWS offset, n	$< 3\% \cdot v_{ref,mean}$ [m/s]	$< 4\% \cdot v_{ref,mean}$ [m/s]
Mean HWS coefficient of determination, ρ^2	> 0.95	> 0.98
Mean HWS Bias	$< 5\% \cdot v_{ref,mean}$ [m/s]	$< 4\% \cdot v_{ref,mean}$ [m/s]
Mean HWS RMSE	$< 8\% \cdot v_{ref,mean}$ [m/s]	$< 4\% \cdot v_{ref,mean}$ [m/s]
Mean WD slope, m	0.97-1.03	0.97-1.03
Mean WD offset, n	< 5 [deg]	< 5 [deg]
Mean WD coefficient of determination, ρ^2	> 0.95	> 0.97

Chapter 3

UPC laboratory-tests campaign and motion compensation by mechanical techniques

This chapter addresses the experimental part carried out to assess the performance of the ZephIR 300 wind lidar and the effects of buoy motion. A mechanical-compensation device, the cardan frame, is tested. The HWS measured by both a reference lidar ('fixed') and a moving lidar (to installed on the floating buoy) "with" and "without" the cardan frame is examined by using standard statistical indicators and a composite-pendulum model. Performance tests are carried out both at the laboratory by using a motion-simulation platform and at PdP sea-test facility.

Results of this Chapter are a combination of a peer-review conference paper, *Tiana-Alsina et al.* (2015), 2015 (available at the IEEE Xplore website `https://ieeexplore.ieee.org/document/7327051`), and deliverables D2.6a and D2.6b from Neptune project (*Tiana-Alsina et al.*, 2013a,b). Systematic or multiple reproduction or distribution to multiple locations via electronic or other means is prohibited and is subject to penalties under law.

3.1 Introduction

There are two main approaches concerning mechanical compensation of the sea wave-induced motion on offshore lidar measurements: The first consists of placing the lidar device on a platform able to absorb the motion of the sea in order to offer the necessary stability, and hence, to guarantee reliable wind measurements (*Nicholls-Lee*, 2013). These platforms are typically either a *spar buoy* or a *tension-leg buoy*. The main inconvenient of these kind of buoys is that they are expensive and difficult to re-deploy. The second approach consists of using a wave buoy (*Schuon et al.*, 2012). The main consequence of the small size of these typology of buoys is that they suffer from translational and rotational motion, which has to be either mechanically or software compensated. Fig. 3.1 describe these two motion components. Translational motions (sway, surge, and heave, along the x, y, and z axes, respectively) can easily be compensated by subtracting the motion vector from the measured wind vector while rotational motions (roll, pitch, and yaw, around the x, y, and z axes, respectively) are more difficult to cancel out. Buoy tilting or spin have a strong impact on the LoS measurement, which can induce a non-negligible bias on the measured wind vector. With the aim of adapting the lidar instrument to measure on floating platforms, a mechanical solution to reduce the impact of lidar motion on the wind-speed is proposed.

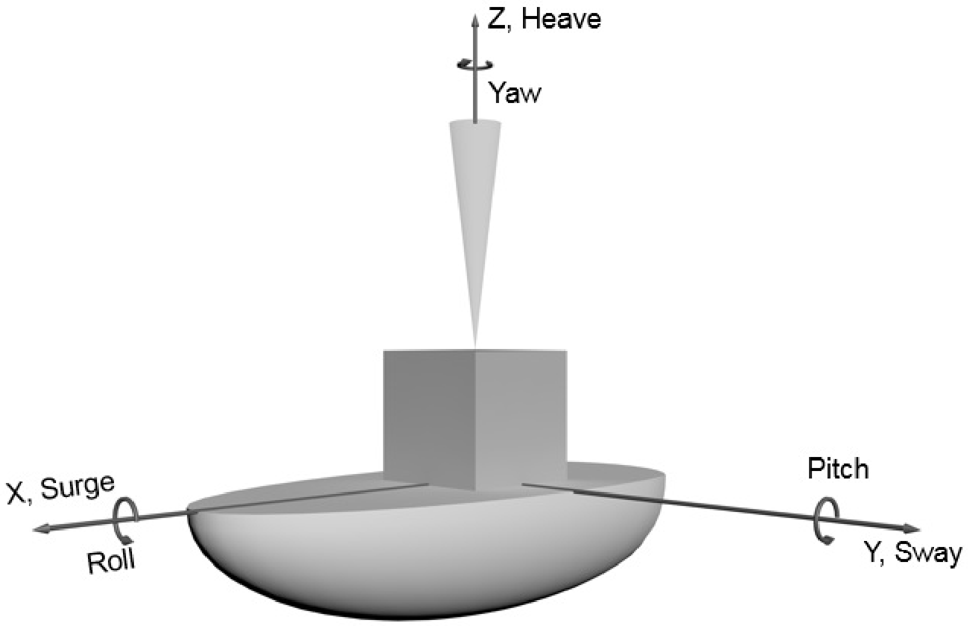

Figure 3.1: Translational and rotational motion along the 3-axis.

At the time of project Neptune (2012), there were few alternatives to the expensive offshore metmast. Additionally, the application of the Doppler-lidar technology to the wind energy field was not as extended as nowadays. For example, the IEA Wind Task 32 concerning the use of lidar in the wind energy field, started its work that same year (*Clifton et al.*, 2018). The first recommended practice for onshore lidar use in wind energy was presented in January 2013 (*Clifton and Courtney*, 2013) and the Carbon Trust roadmap for acceptance of floating lidar technology dates from November 2013 (*Carbon Trust*, 2013).

Therefore, it becomes necessary to carry out measurement campaigns to ensure the reliability of Doppler-lidar data and to study the impact of wave-induced motion on the main magnitudes relevant for wind energy field. First, tests were carried out to quantitatively assess the measurement accuracy of one commercially available lidar unit in the absence of motion. It become necessary to evaluate the impact of the separation distance between the reference and analysed sensor, the importance of other environmental magnitudes (e.g. atmospheric stability) or the location of the experiment.

Once gathered the relevant information about the performance of the static lidar, the second step was to evaluate the impact of sea wave-induced motion on its measurements. To that end, a motion-simulation platform was designed. The platform was capable of simulating angular motion of different amplitudes and frequencies along roll and pitch axes. This platform allowed to better understand the lidar performance in the live-sea conditions during the next phases of the project.

The final step was to develop and test a mechanical motion-compensation device aimed to reduce the amount of buoy motion that is transmitted to the lidar. A double cardan frame was build and tested by the Maritime Engineering Lab (LIM/UPC). The design allowed to keep the lidar virtually still when the buoy/platform holding it was tilted. Performance of the cardan frame was first validated in laboratory tests and finally in near-shore conditions at PdP, Badalona.

This chapter studies degree of correlation between two ZephIR 300 lidars units, one fixed (reference lidar) and another moving (floating), under different experimental scenarios. This conditions include “large” angular movements that the floating lidar is to suffer at the sea. The measurement campaign took place at UPC North Campus premises, Barcelona, October 2011 to February 2013. The near shore tests started the 24th May 2012 and ended the 31th June 2012.

3.2 North-Campus Measurement Tests

Fig. 3.2 show the location of the LIM/UPC installation in which were carried out the first measurement campaign. It is worth to note that calibration test were carried out at the roof of building D3 (Fig. 3.2b) while all the other tests where performed at ground level (Fig. 3.2a).

The goal of the laboratory tests was to intercompare both ZephIR 300 lidars (to be called “reference” and “floating” lidar in what follows with a view to the future application) under the same measurement scenario. Due to the fact that the measurement test site was located at the University campus, this measurement campaign was carried out in a complex terrain environment (i.e. surrounded by buildings). Since local wind circulation and highly turbulent wind fields were observed during the campaign we placed both lidars as close as possible to each other in order to minimize terrain-induced wind speed errors.

(a) (b) (c)

Figure 3.2: Location of LIM/UPC facilities where the North-Campus measurement campaign was carried out. (a) Moving platform. (b) Fixed calibration. (c) Photo of the roof. In (a) Black dots denote the position of the reference and floating lidars and, light red circles the lidar cone projection at 10-m.

Three different experimental setups were considered:

First step .- In the first setup both lidars are kept fixed (i.e. one besides the other, Fig. 3.2c) in order to ensure the nearly identical measurement conditions between the two lidars. The lidars were fixed and configured to measure at 100 m. Two different separation were considered: “closely-spaced lidars" range ($1-m$ separation to assess how both lidars measure when collocated), "distantly-spaced lidars" ($40-m$ separation to study the impact of the separation).

Second step .- In the second experimental setup "reference" lidar was fixed and, the "floating" lidar was placed the motion simulator platform (Fig. 3.3a). Both lidars were configured to measure at 100-m height. The mechanical platform allows two degrees of freedom (pitch and roll). Rotation around the Z-axi (yaw) was not considered because it is corrected by subtracting this magnitude from the measured WD. To track all-relevant motion, i.e., translational accelerations and angular attitude of both the platform and the "floating" lidar, two Microstrain 3DM-GX3 IMUs were used. These IMUs yield angular attitude and angular speed as rotational variables as well as translational accelerations.


(a) (b)

Figure 3.3: Motion simulator and experimental test setup. (a) Motion platform used to simulated pitch and roll tilting. (b) Cardan frame used to counter-balance the motion applied by the platform simulator. Both the motion-simulation platform and the cardan frame have been developed by the Maritime Engineering Lab (LIM-UPC).

Different angular motions where applied to the motion-simulation platform. Wave periods, $T = 3$, 6 and 12 s, and amplitudes, $A = 11, 16$ and 25 deg, were used. These values correspond to typical values measured along the Catalan coast (see (*Bolaños et al.*, 2009)). Measurement time series typically lasted for 300 minutes.

The "moving" lidar was mounted on the cardan frame, which was sitted on the simulation platform (Fig. 3.3b). The cardan frame was equipped with eight dampers (four on each axis), which were tuned to find the best strength to counterbalance the motion of the platform (4.5 turns, which corresponds to an intermediate damping). In addition, under this damping configuration, the cardan frame was able to rapidly absorb sudden impacts. Tab. 3.1 summarises the cardan frame parameters used.

Final step .- The third and last experimental setup were near-shore sea tests with a proof-of-concept buoy. This buoy was installed 250 m offshore PdP pier, Badalona (Barcelona), from May to July 2015 (to be described in Chapter 4).

Table 3.1: Cardan frame configuration parameters.

Parameter	Original	Optimized
Mass, m [kg]	105	105
Length, L [m]	0.53	0.0005
Moment of Inertia, I [kg·m^2]	10.03	10.03
Damping Coefficient, d [N·m·s/rad]	19	5

3.3 Results

3.3.1 Calibration tests with both lidars fixed

Next are shown the measurements results obtained for the first experimental setup described in Sect. 3.2(Fig. 3.2). KPIs defined in Sect. 2.3 are used to assess error performance between both lidars.

Two distances between lidars were studied, "closely-spaced lidars" ($1-m$ apart) and "distantly-spaced lidars" ($40-m$ apart). The aim of the and "distantly-spaced lidars" is to recreate the eonditions to be found at PdP, where the reference lidar and lidar buoy will be separated around $50-m$.

Since the results obtained for the "closely-spaced lidars" and "distantly-spaced lidars" are conceptually analogous only the "closely-spaced lidars" are analyse in detail. The main difference between both configurations lies in the fact that for the "distantly-spaced lidars" the measurement delay between the time series measured by both lidars is longer.

Sects. 3.3.1.A and 3.3.1.B show the key figures for high- (1-s) and low- (10-min) temporal resolution respectively. For the 1-s data are only shown results for the HWS while for the 10-min data are presented results for the these three main variables: HWS, VWS, and WD. The reason for not showing 1-s WD and VWS lies on the fact that conclusions are analogous than for 10-min data.

3.3.1.A High temporal resolution data (1-s)

Closely-spaced lidars .- The statistical parameters (Sect. 2.3) obtained during 36 h continuous measurement (from 19/10/12 12:00 to 21/10/12 24:00) are summarized in Tab. 3.2. These statistical parameters are computed for the three main variables: HWS, VWS, and WD, using 1-s data.

Table 3.2: 1-s statistics for the "closely-spaced lidars" study (19/10/12 12:00 - 21/10/12 24:0).

	Bias	RMSE	Slope	Offset	R^2
HWS	-0.0489	0.5574	0.9903	0.1059	0.9572
VWS	-0.0494	0.5874	0.1182	0.0441	0.0141
WD	-61.429	108.14	0.065	102.79	0.0056

For the 1-s HWS data, bias, slope and offset (i.e. intercept point) are within the acceptance region defined in 2.3, while RMSE and determination coefficient (R^2) do not comply with. Regarding VWS and WD variables, none of the computed statistical indicators satisfy the specified requirements. As it will be shown next, the main reason for those poor figures are phase jumps caused by homodyne detection ambiguities. Otherwise, the atmospheric stability also affect the quality of the statistical parameters.

Fig. 3.4 and Tab. 3.2 show the main results for the 1-s HWS test ("closely-spaced lidars"). Fig. 3.4a shows 1-s HWS temporal series for both lidars with both of them collocated and measuring at 100 m height. The HWS time series of both lidars are in good agreement but -as expected- errors are observed.To quantify discrepancies between both time series Fig. 3.4b shows the HWS scatter plot between both data sets.

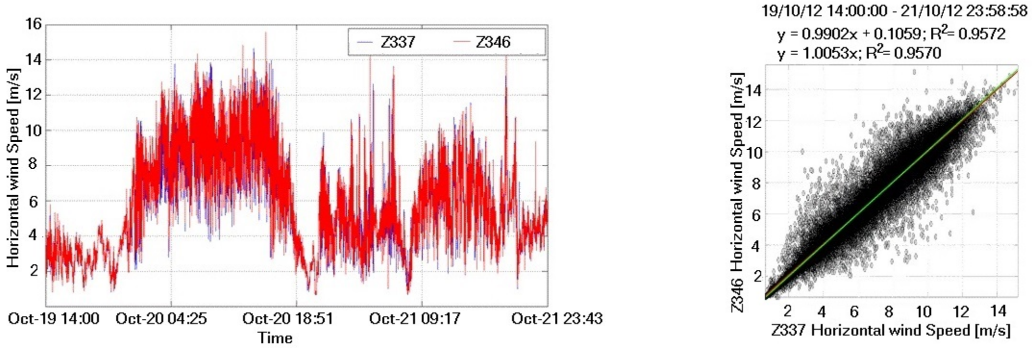

(a) (b)

Figure 3.4: 1-s data for fixed calibration test at "closely-spaced lidars" test. (a) Temporal series, (b) scatter plot.

It is observed that the data points are distributed along a fitting line with slope approximately unity and offset approximately zero, which indicates a clear correlation between both signals. Two linear models have been used to fit the data with a straight line: with and without offset term (so called independent term). The red line corresponds to the linear model of Eq. 2.10 and the green line to Eq. 2.11 model. The determination coefficient (Tab. 3.2) is reasonably high but not as good as expected for a collocated calibration test. The deviation, which is about 5%, is mainly associated to large fluctuations in the time series.

Fig. 3.5 shows four key parameters measured by the lidar: Points in Fit (PiF), Backscatter indicator parameter, and the Spatial Variation (SV). The PiF parameter is the number of radial wind speed measurements per scan, the backscatter parameter is one indicator directly related to mean backscattered intensity, and the SV is a parameter directly related to the Turbulence Intensity (TI) of the radial wind-speed components within the circle of scan. Data Validity parameter is a suggested boolean indicator of the validity of each data.

In Fig. 3.5 are observed some regions with high backscater levels (> 3 [units]) and high SV (around 0.5 [units]), which would correspond to a cloud layer at the sounding height (100 m) or below it, and to poor homogeneity of the wind in the sounding volume, most probably due to low winds. This assumption is in accordance with the atmospheric conditions existing during the test. On other periods, other regions with a moderate backscatter (between 0.1 and 3 [units]) are observed, which can be associated with clear atmospheric conditions; good operation of the lidar device is expected.

To qualitatively show the effect of the backscattering indicator on the correlation between the

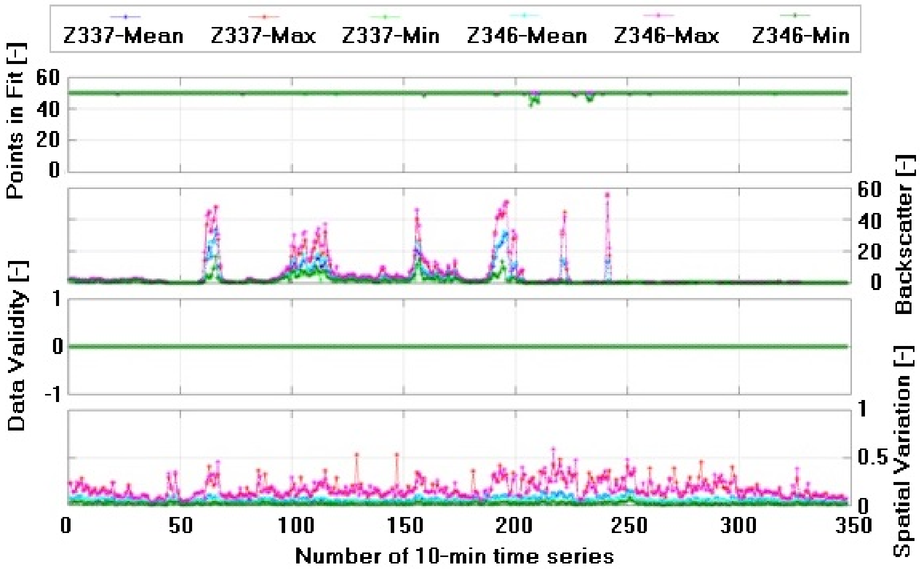

Figure 3.5: 10-min lidar internal-parameters time series (closely-spaced-lidars test).

two lidars, two time intervals are analysed: with (i) moderate and (ii) high backscatter indicator.

Tab. 3.3 shows the statistical parameters obtained for the case of moderate backscatter (19/10/2012 14:00 to 20:00). With comparison to Tab. 3.2 a clear improvement on the statistical parameters is evidenced.

Table 3.3: 1-s statistical parameters obtained for moderate-backscatter levels (19/10/2012 14:00 to 20:00 Local Time (LT)).

	Bias	RMSE	Slope	Offset	R^2
HWS	-0.0130	0.0867	0.9876	0.0479	0.9850
VWS	-0.0067	0.0505	0.9627	0.0095	0.9457
WD	-9.0337	5.6791	0.9435	11.281	0.9118

In this particular time interval, the statistical parameters obtained for the HWS are within expected KPIs values defined in Tab. 2.3. Additionally, statistical parameters for the VWS and WD have also improved. For the 1-s WD data, all statistical parameters approach (without reaching) the required performance indicators. Sudden 180 *deg* jumps are the responsible for this lost of correlation. The worst WD indicators are bias and offset because the two lidars were not perfectly oriented. After they were re-oriented (not shown), is achieved a bias of 6 *deg* (only 1 *deg* above acceptance criteria) and offset around 4 *deg*, which are relatively close to the desired confidence defined by the KPIs.

Fig. 3.6 shows 1-s HWS scatter plots under different conditions: Fig. 3.6a shows the case of moderate backscatter (19/10/2012 14:00 to 20:00). Fig. 3.6b shows the case of high backscatter (20/10/2013 00:00 to 10:00), which exhibits degraded statistics.

On the other hand, and as it can be seen from Tab. 3.4 and Fig. 3.6b, the determination coefficient for the high-backscatter case (20/10/2012 00:00 to 10:00) significantly degrades with respect to Fig. 3.6a. A similar behaviour can be observed when analysing regions with high SV.

Table 3.4: 1-s statistical parameters obtained for high backscatter power return (20/10/2012 00:00 to 10:00 LT).

	Bias	RMSE	Slope	Offset	R^2
HWS	-0.1438	0.8074	0.8692	1.2679	0.7369
VWS	-0.0822	0.5510	0.1813	0.0132	0.0324
WD	-	-	-	-	-

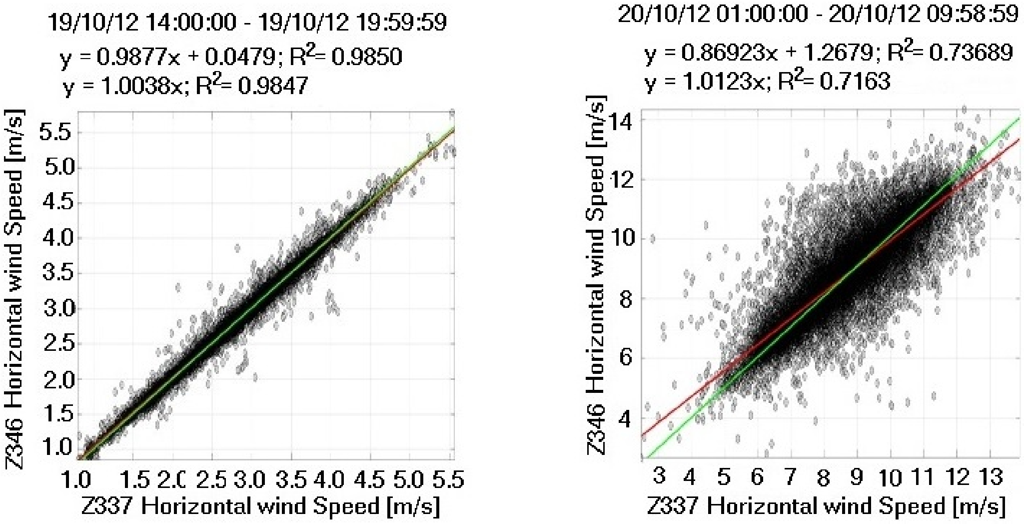

(a) (b)

Figure 3.6: 1-s scatter plots for different backscatter levels. (a) Moderate backscatter. (b) High backscatter.

The computed statistical parameters for a high backscatter scenario (cloudy atmosphere) are clearly poorer. While for clear atmospheres both lidars show excellent agreement (Tab. 3.3), under low clouds or low wind speeds (Tab. 3.4) the correlation unquestionably decays.

Distantly-separated lidars .- To intercompare high temporal resolution data of two lidars a some distance it becomes necessary to take into account the time that takes the wind to travel from one to the other, e.g., 5 s to travel 50 m at 10 m/s speed. This methodology called *delay correction* will be further discussed in Sect. 4.3.1

Regarding the 1-s HWS acceptance criteria defined in Tab. 2.3 after applying the delay correction, all statistical parameters are within the requirements. On the other hand WD statistical parameters approaches the required KPI.

A final remark is that for separations below approximately 50 m statistical performance parameters between the two lidars do improve by compensating for the wind travel delay. However, above this separation there are other disturbing atmospheric phenomena (e.g., large signal fluctuations due to the cumulative effects of turbulence along the travel distance between the two lidars) that do not allow further improvement by just compensating by the travel delay.

3.3.1.B Low temporal resolution data (10 min)

This section shows similar tables and figures to those shown in Sect. 3.3.1.A but for the 10-min data.

As expected, errors on the retrieved wind variables (HWS, VWS, WD) for the 10-min data are smaller than for the 1-s data because fast temporal fluctuations are smoothed out during the 10-min average.

Closely-spaced lidars .- Tab. 3.5 show the computed statistical parameters for 10-min averaged data. The scatter plot analysis has been performed by using the linear model presented in Eq. 2.10.

Table 3.5: 10-min averaged statistics for the closely-spaced lidars test (Eq. 2.10 model).

	Bias	RMSE	Slope	Offset	R^2
HWS	-0.0470	0.1308	1.0149	-0.0413	0.9975
VWS	-0.0052	0.1415	0.8483	0.0345	0.5961
WD	16.601	119.27	0.9988	8.2832	0.9958

Regarding the 10-min HWS acceptance criteria (defined in Tab. 2.3) this test corresponds to the most beneficial scenario.

Fig. 3.7 shows 10-min data for the two lidars collocated on the roof of building D3. HWS temporal series for the two lidars devices are in very good agreement (Fig. 3.7a). Fig. 3.7b shows that the 10-min HWS scatter plot has significantly improved over Fig. 3.4b. The two regression lines plotted correspond to Eq. 2.10 and Eq. 2.11 fitting models.

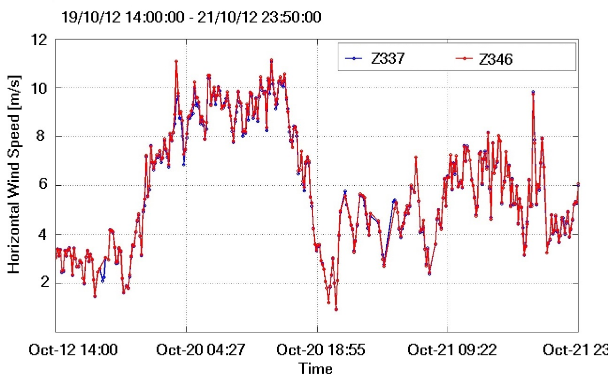

(a) (b)

Figure 3.7: 10-min data for the closely-spaced lidars test. (a) Temporal series. (b) Scatter plot.

Fig. 3.8 shows the absolute HWS error distribution (grey bars), which follows a normal distribution centered at the corresponding bias (Eq. 2.8, green line) and with a Full Width at Half Maximum (FWHM) equal to two times the RMSE (Eq. 2.9, red lines).

Fig. 3.9 shows main results for the 10-min WD data. Fig. 3.9a shows the WD time series corresponding to both lidars. It can be seen that both lidars exhibit 180 *deg* sudden jumps. These jumps are a consequence of the inherent ambiguity of homodyne detection. Apart from these jumps, WD time series from both lidars are in good agreement. The slight bias observed between the two time series is attributed to misalignment between the two lidars.

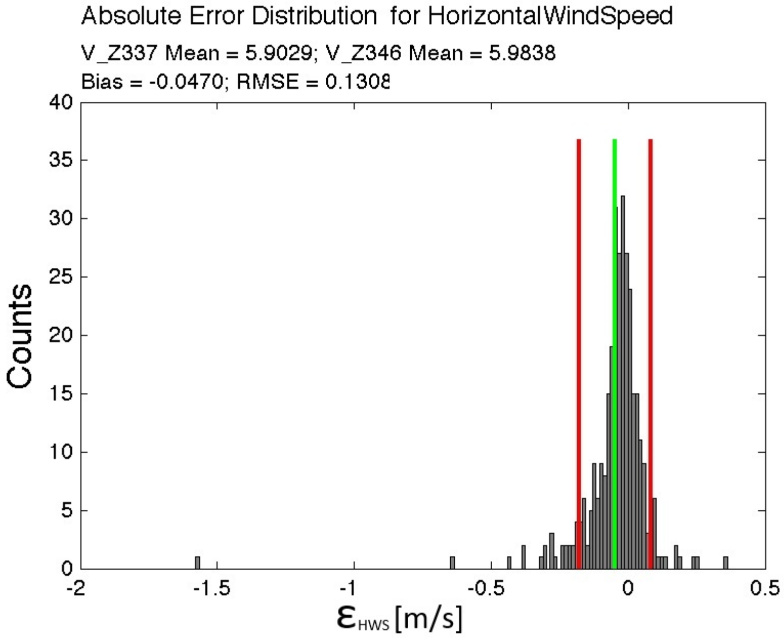

Figure 3.8: 10-min absolute-error distribution for the closely-spaced lidars test.

To study the correlation between the WD time series, the time series are split into three families; 0 *deg*, +180 *deg*, and −180 *deg* difference. Once the data is split into these phase-jump families regression lines are fitted to them.

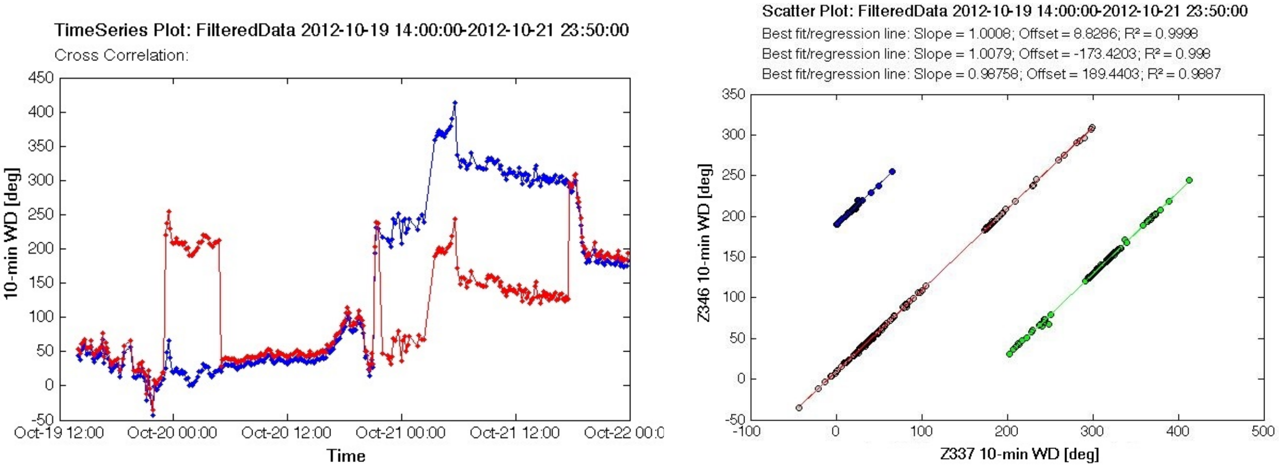

(a) (b)

Figure 3.9: 10-min WD corresponding to fixed closely-spaced lidars test. (a) Temporal series. (b) Split scatter plot.

Fig. 3.9b shows the scatter plot and the corresponding linear fit (Eq. 2.10) for each of the three WD families, respectively. Grey dots correspond to 0-deg difference, green and blue dots corresponds to −180 *deg* and +180 *deg* difference respectively. Excellent correlation is achieved in all the three families.

Finally are presented the results obtained for VWS data measured at 100-m height (Fig. 3.10). Fig. 3.10a plots the time series measured by both lidars. A clear mismatch between the two time series is observed. At some times, the VWS of the two lidars are anticorrelated ($\rho = -1$), which means ther measured opposite vertical directions. As a result, a poor correlation is obtained. This difference in the VWS sign is also related with the homodyne measurement principle of the ZephIR 300 lidar.

Fig. 3.10b is a split scatter plot of the VWS measured by the two lidars.Two distinct behaviours are shown, one corresponding to positively-correlated data (grey dots), which fits to a straight line with positive slope equal to 1, and another behaviour corresponding to negatively-correlated data (green and blue dots), which approximately fits to a straight line with negative slope equal to ~ 1.

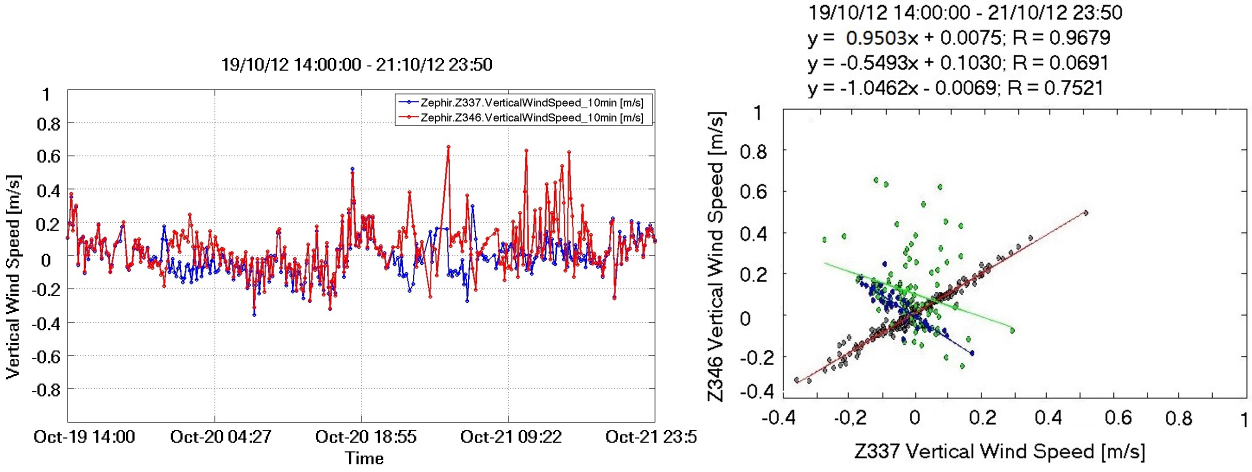

(a) (b)

Figure 3.10: 10-min VWS corresponding to closely-spaced lidars tests. (a) Temporal series. (b) Split scatter plot. NOTE: Please note that x and y-axis do not appear of equal length.

Distantly-spaced lidars .- Fig. 3.11 studies 10-min averaged HWS data for the two lidars 50 *m* apart. The averaging process to obtain 10-min data has filtered out the impact of distance observed at 1-s data. A difference smaller than 0.5% in R^2 is observed between closely and distantly-spaced data sets. Results are within the acceptance criteria of Tab. 2.3.

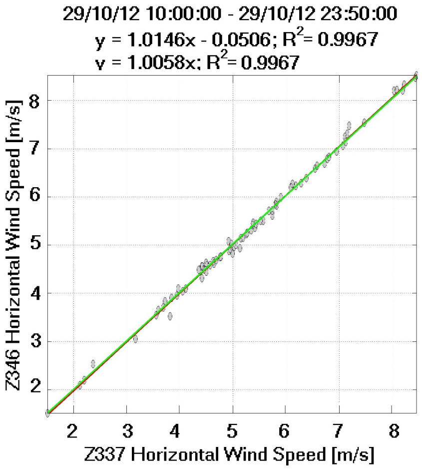

Figure 3.11: 10-min scatter plot HWS corresponding to distantly-spaced lidars test.

3.3.2 Cardan frame laboratory tests

To qualitatively study the motional effect (pitch and roll rotation) on the HWS, VWS and WD errors and its compensation when a cardan frame is used, two case examples are presented: *Moving platform* and *Free cardan frame*, for both 1-s and 10-min data.

First, the reference lidar (Z346) is kept fixed, and the floating lidar (Z337) placed on the motion simulator platform (see motion table in Fig. 3.3a). Afterwards, the moving lidar will be assembled into the cardan frame to help counterbalance the movement of the motion table (See Fig. 3.3b.

3.3.2.A High temporal-resolution data

Two cases will be analyse for 1-s data:

- (i) *blocked cardan frame*, this is to say, with no mechanical compensation.
- (ii) *free cardan frame*, therefore able to activate the mechanical compensation of the platform motion.

Blocked cardan frame .- During this test, harmonic oscillation are applied to the pitch angle of the motion platform. As it can be seen in Fig. 3.12, the amplitude is ∼ 16 *deg* and period ∼ 12 *s*. With these particular settings the motion-induced error is considerably high.

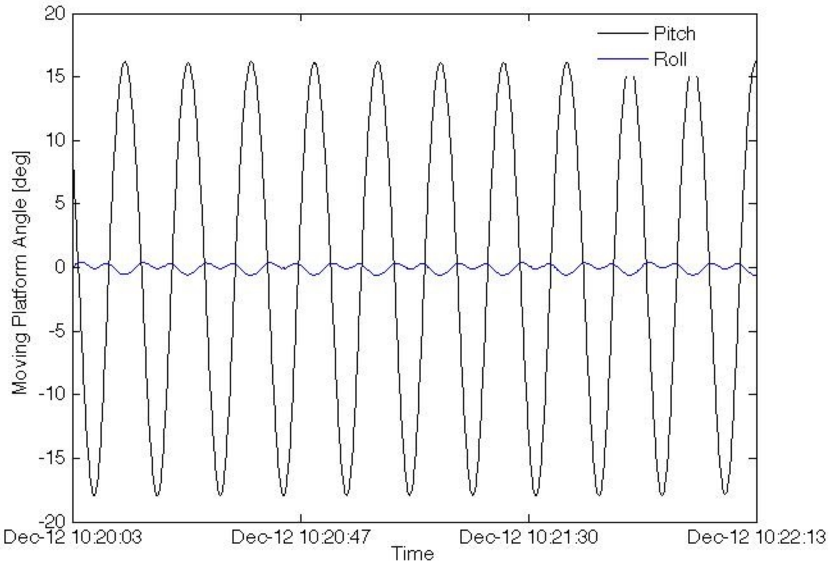

Figure 3.12: Platform motion time series (blocked cardan frame).

When pitch excitation is applied Fig. 3.12 also shows residual rotation of about 1-deg in roll. This is caused by mechanical imperfections in the platform and can be assumed negligible for the purpose of this study.

Tab. 3.6 summarize the statistical parameters obtained for this case example (moving platform)

Comparing Tab. 3.6 above with Tab. 3.2 closely-spaced lidars), a clear deterioration of the statistical parameters is evidenced. When the motion of the platform is not compensated, the

Table 3.6: 1-s statistical parameters for the blocked cardan-frame case study ($A = 16\ deg$, $T = 12\ s$, Eq. 2.10 model).

	Bias	RMSE	Slope	Offset	R^2
HWS	0.0289	0.3705	0.8358	0.3253	0.7126
VWS	-0.2073	0.6084	-0.3432	0.0659	0.1671
WD	-146.09	60.19	0.3378	216.23	0.1035

statistical parameters are undoubtedly out of the required 1-s KPI, Tab. 2.3. The HWS and WD determination coefficients and slopes are far from unity, the offset is clearly larger than 2% of the mean HWS and WD. The RMSE fails the KPI test as expected. The only statistical indicator that passes the KPI test is the HWS bias which is within the desired limits of acceptance.

Fig. 3.13 presents the results of the blocked cardan-frame tests. Fig. 3.13a shows the HWS time series for both the fixed and the moving lidar. It is seen that the time moving-lidar series largely fluctuates around the fixed-lidar time series. This effect is responsible for a 20 % reduction in the determination coefficient. Period of these fluctuations coincide with the motional period, therefore, it can be inferred that the observed scattering is mainly due to the motion.

Fig. 3.13b HWS scatter plot shows a spread in the data distribution mainly caused by the oscillatory movement applied. The linear fit model (Eq. 2.10) shows a clear positive offset, which accounts for underestimation of the moving-lidar HWS. Its hypothesized that may be caused by the fact that - due to the oscillation - the moving lidar measures on average at lower heights than the fixed lidar. On account of the standard wind-shear profile, lower wind speeds will be measured.

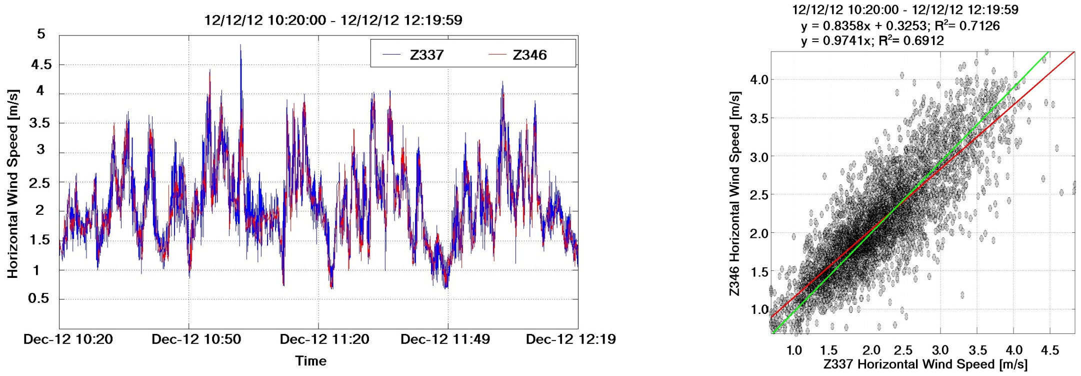

(a) (b)

Figure 3.13: 1-s HWS corresponding to cardan blocked moving lidar test. (a) Temporal series. (b) Scatter plot.

Fig. 3.14 plots the distribution of the HWS absolute error defined as in Eq. 2.7 in terms of different magnitudes such as histogram of events frequency (Fig. 3.14a), WD (Fig. 3.14b), or HWS (Fig. 3.14c).

From Figs. 3.14b and 3.14c it is evidenced that the largest errors occur around 250-deg WD and 1-to-2.5-m/s HWS. When plotting bin-averaged data (red and blue dots in Figs. 3.14b and 3.14c, respectively) a uniform distribution is observed. This is indicative that the surrounding complex terrain –as it the case at UPC premises- uniformly affects the HWS error distribution.

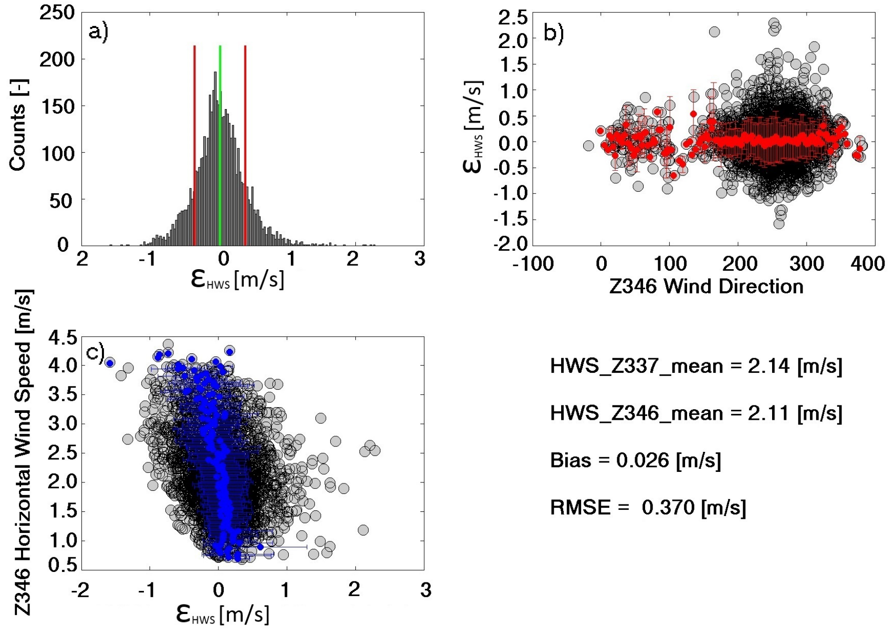

Figure 3.14: 1-s HWS absolute-error distribution versus HWS and WD. Cardan-frame blocked. (a) Histogram of the HWS differential error (Eq. (2.7)). (b) Scatter plot of the HWS differential error versus WD. (c) Scatter plot of the floating-lidar HWS differential error vs moving-lidar HWS differential error.

Concerning 1-s WD data, degradation of the determination coefficient (shown in Tab. 3.6 comparing to Tab. 3.2) can be associated to two intrinsic mechanisms: First, as with HWS measurements, the movement itself induces errors on the measured WD. Additionally, as it can be seen in Fig. 3.15, sudden 180 *deg* back- and forth phase jumps occur, all of which worsens the determination coefficient. However, these phase jumps were not observed during the calibration tests.

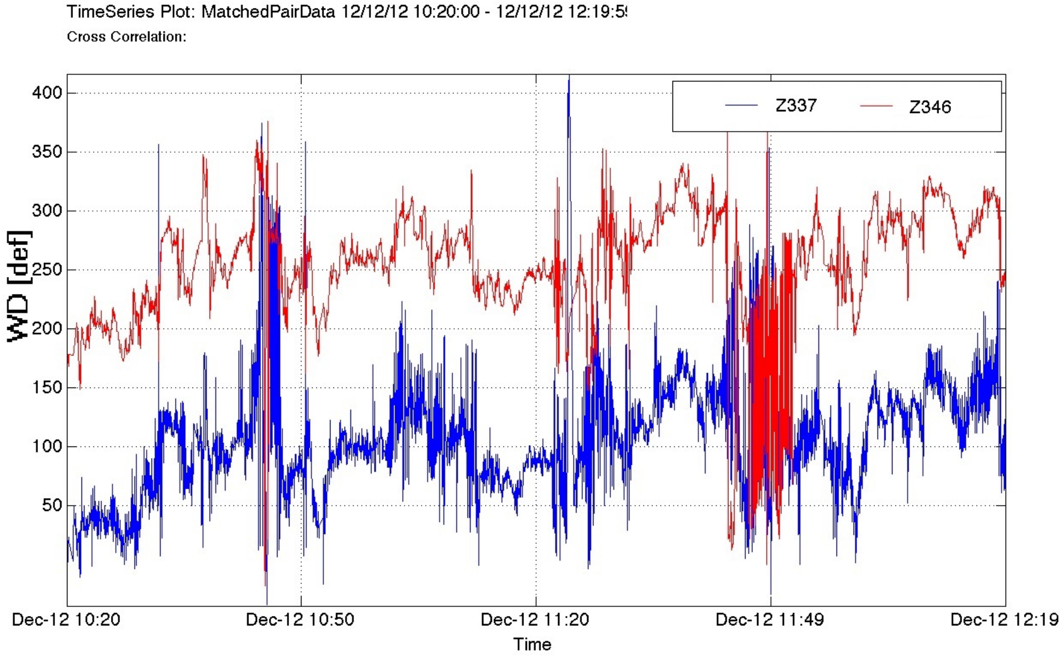

Figure 3.15: 1-s WD time series (cardan-frame blocked test).

Because sudden phase jumps appear for both the reference and the moving lidars a cause-effect relation between motion and phase jumps cannot be inferred. It is assumed that the complex terrain where the tests have been carried out is responsible for these phase jumps.

The evident effects of motion is a worsening in all the statistical parameters discussed so far (bias, RMSE, slope, offset and determination coefficient). The determination coefficient is particularly poor for the WD variable. There are two main reasons for that: the oscillatory movement itself which induces fluctuations in the WD, and back-and-forth (sudden) 180 *deg* phase jumps.

Free cardan frame .- As in the blocked-cardan-frame test harmonic motion is applied on the pitch angle. Yet, in this case, the cardan frame is unblocked to allow for compensating motion. The cardan frame is equipped with eight dampers (ACE, model HB-22-150-EE-P) tuned to 4.5 turns. As shown in Tab. 3.7 (and by comparison to Tab. 3.6) all statistical parameters related to the HWS and WD improve. However, large errors do persist for the VWS. An increment of the correlation of about 20% for the HWS data and of about 80% for the WD data is observed.

Table 3.7: 1-s statistical parameters for the free-cardan-frame case study ($A = 16\ deg$, $T = 12\ s$, Eq. 2.10 model).

	Bias	RMSE	Slope	Offset	R^2
HWS	0.0063	0.1985	0.9567	0.1136	0.9434
VWS	-0.0054	0.5116	-0.3559	0.0573	0.1419
WD	177.06	16.666	0.9373	-160.74	0.8553

The improvement in the statistical indicators moves the system closer to the required HWS KPIs. While the bias lies within the acceptance region, the RMSE and the offset are still far from the virtually ideal figures of Tab. 2.3. The large RMSE obtained in Tab. 3.7 indicates that non-negligible fluctuations around the reference measurement persist. At this point, it is important to remark that WD statistical parameters behaves worst due to sudden 180 *deg* phase jumps (see e.g. Fig. 3.19).

As shown in Fig. 3.16, pitch angular amplitude of the moving table is $\sim 16 - deg$ and period is approximately $12 - s$. The pitch amplitude of this moving lidar is ± 2 *deg* approximately, which evidences satisfactory motion compensation. This represents an 85% reduction.

As in Sect. 3.3.2.A, the roll angle shows a residual movement (mechanical cross talk), which cannot be eliminated. Fig. 3.16 also evidences a time delay between the moving-platform and the moving-lidar time series. This, however, does not impede correct operation of the cardan frame.

Figure 3.17 shows the results of the 1-s HWS for the free cardan tests. With the cardanic frame active, nearly filters out the signal fluctuations induced by the motion simulator platform as it can be seen in Figure 3.17a. In Figure 3.17b the scatter plot and the fitting lines are depicted.

As mentioned, motion-induced minor HWS fluctuations still persist when comparing Fig. 3.17b with closely-spaced lidar tests (Fig. 3.6). Two main reasons may account for that: (i) angular motion of the lidar is not completely compensated by the cardan frame (3.16) so there is still influence of the inclination of the lidar and (ii) the environmental conditions (backscatter or SV) still produces differences in the measurements of both lidars. Translational velocity component of the lidar are rejected as cause of this behaviour because subtracting this speed to the measurement of the moving

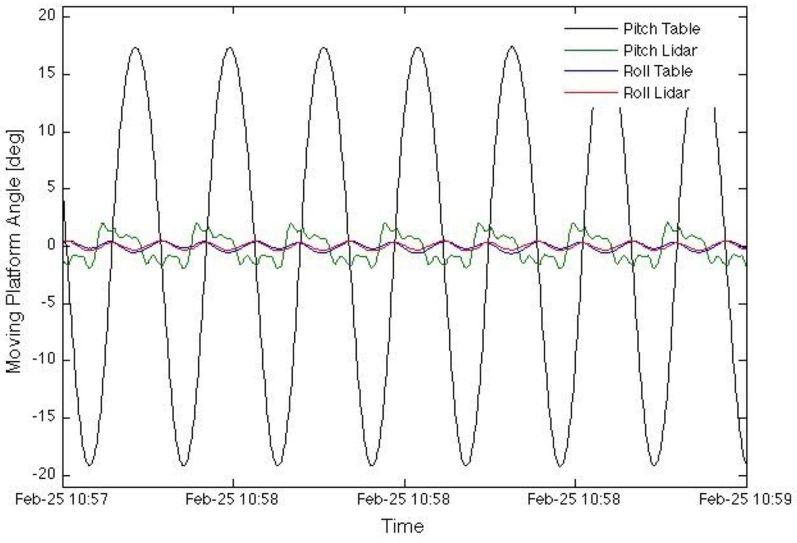

Figure 3.16: Platform motion free-cardan-frame time series.

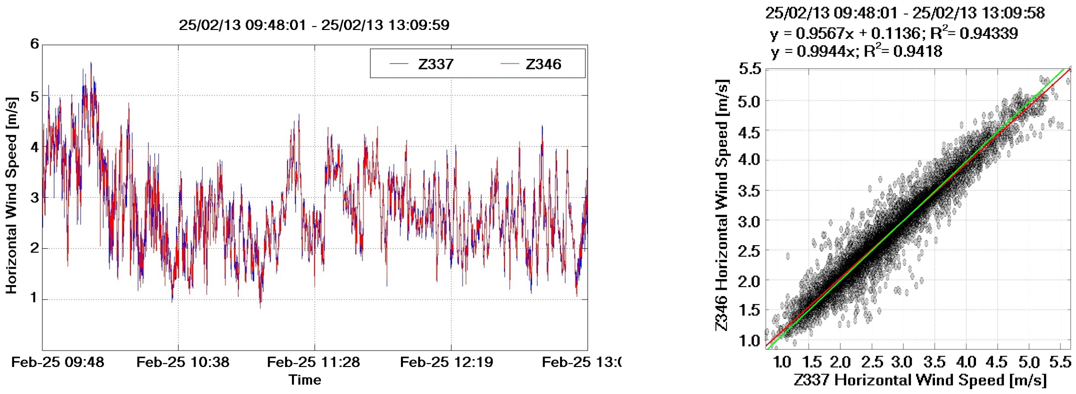

(a) (b)

Figure 3.17: 1-s HWS time series for the moving (Z337) and reference (346) lidars (free-cardan-frame tests). (a) Temporal series. (b) Scatter plot.

lidar produces no significant improvement (those velocities components are one order of magnitude smaller than the measured HWS).

Fig. 3.18 shows that the absolute error distribution narrows and the determination coefficients approach to unity. This evidences the smoothing effect the cardan frame has on the moving-lidar HWS time series. It can be concluded, at least for this case example ($A = 16\ deg$, $T = 12\ s$), that the cardan frame becomes a valuable motion-compensation.

Finally, Fig. 3.19 shows the WD time series meaured with the cardan frame unblocked. When comparing with Fig. 3.15 the smoothing effect of the cardan frame is evident. Besides, there are less 180 *deg* phase jumps (still afew around 25/02/2013 10:38 LT and at the end of the timeseries).

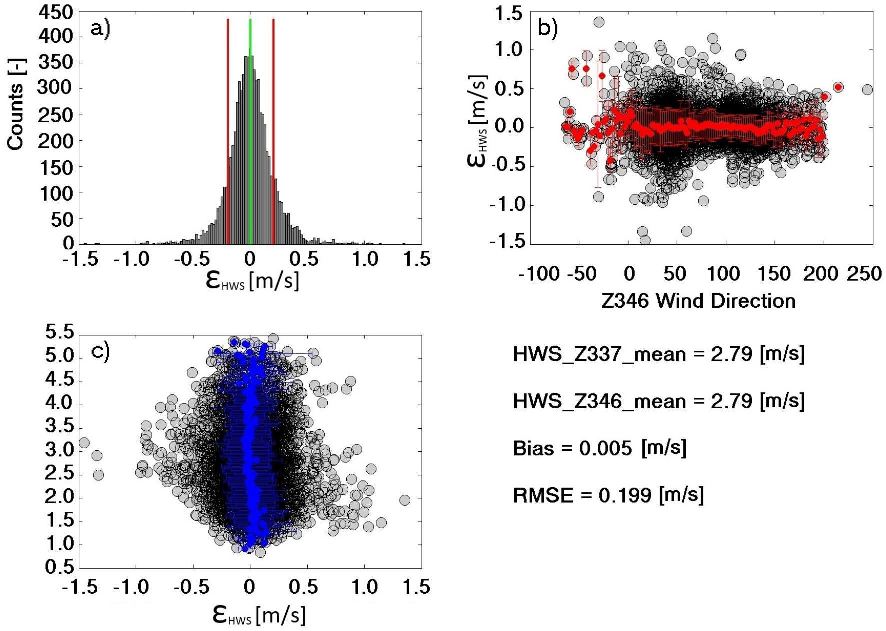

Figure 3.18: 1-s HWS absolute-error distribution versus HWS and WD. Free cardan-frame. (a) Histogram of the HWS differential error (Eq. (2.7)). (b) Scatter plot of the HWS differential error versus WD. (c) Scatter plot of the floating-lidar HWS differential error vs moving-lidar HWS differential error.

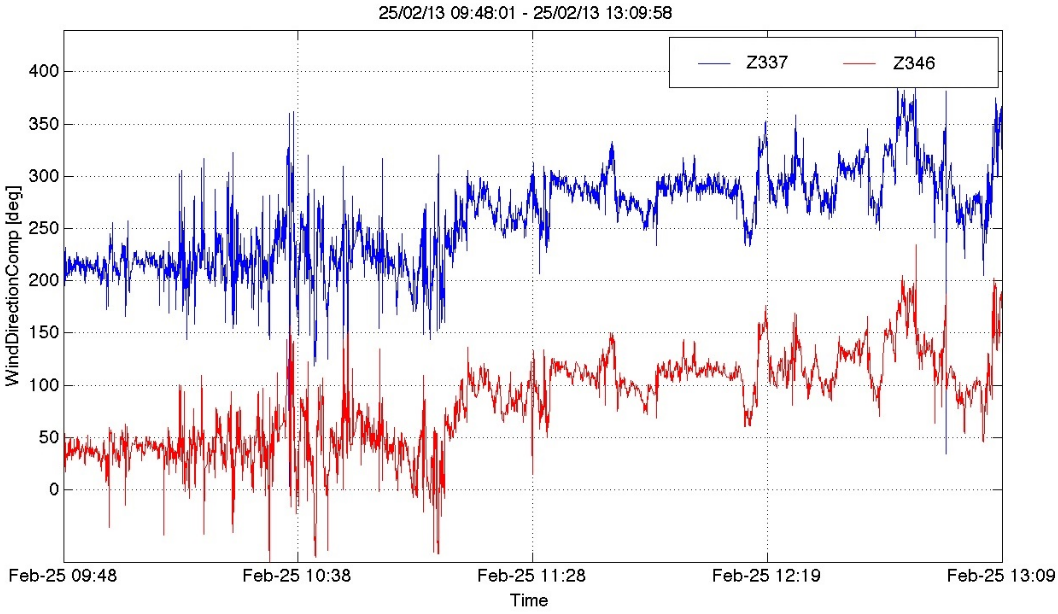

Figure 3.19: 1-s WD time series (free-cardan-frame test).

3.3.2.B Low temporal-resolution data

In this section, 10-min measurements results with and without mechanical compensation are inter-compared. Quantitative results are presented in relation to described KPI (Tab.2.3) and for the three variables under study, HWS, VWS, and WD.

10-min moving-lidar statistical parameters for the blocked cardan-frame tests are summarized in Tab. 3.8. A clear improvement is observed for all of them, even if the platform motion is not compensated.

Table 3.8: 10-min moving-lidar statistical parameters (cardan-frame blocked, $A = 16$ *deg*, $T = 12$ *s*, Eq. 2.10 model).

	Bias	RMSE	Slope	Offset	R^2
HWS	0.0347	0.0315	0.9763	-0.0171	0.9949
VWS	-0.2388	0.3509	-0.7732	0.0213	0.8273
WD	-158.44	7.3627	1.0313	-215.68	0.9791

The WD fails the KPI because both the determination coefficient and the slope fall below the specs of Tab. 2.3. As mentioned, WD bias and offset are associated to the persistent 180 *deg* phase jumps.

For the same motion motional conditions, Tab. 3.9 shows 10-min statistical parameters for the moving lidar when cardan-frame is free to compensate the motion.

Table 3.9: 10-min moving-lidar statistical parameters (cardan-frame free, $A = 16$ *deg*, $T = 12$ *s*, Eq. 2.10 model).

	Bias	RMSE	Slope	Offset	R^2
HWS	0.0022	0.0374	0.9645	0.1003	0.9966
VWS	-0.0628	0.1969	-0.9607	0.0944	0.3069
WD	176.22	0.7302	1.0093	-178.75	0.9996

When comparing Tab. 3.8 and Tab. 3.9 a slight improvement is observed although it is not so high as compared to the case of 1-s data. A most relevant result is the improvement in the bias and RMSE. In Tab. 3.9, all HWS and WD statistical indicators comply with KPI (Tab. 2.3).

Fig. 3.20 shows 10-min HWS scatter plots for the moving lidar ($A = 16$ *deg*, $T = 12$ *s*). In both cases, blocked cardan-frame (Fig. 3.20a) and free cardan-frame (Fig. 3.20b), excellent agreement emerges between the two lidars. Surprisingly, the offset term is substantially larger in the free-cardan-frame test. This effect may be due to the lack of statistical significance of the data ($N = 18$ datasets) but neither case represent a relevant error for the HWS.

Fig. 3.21 shows 10-min scatter plots for the VWS when the moving lidar is without (Fig. 3.21a) and with (Fig. 3.21b) mechanical compensation. When the cardan frame is blocked, an anticorrelated behaviour is observed, which is in agreement with similar behaviour in Fig. 3.10b. When the cardan frame is free the anticorrelated behaviour is similarly observed.

Fig. 3.22 shows the 10-min scatter plots for the WD when the moving lidar has cardan frame blocked (Fig. 3.22a) or free (Fig. 3.22b). In the latter case, a clear improvement is observed in comparison to the blocked-cardan-frame case.

It is worth noting that the amount of data for the 10-min averaged tests shown is insufficient to ensure statistically significance, therefore, these results must be considered with caution.

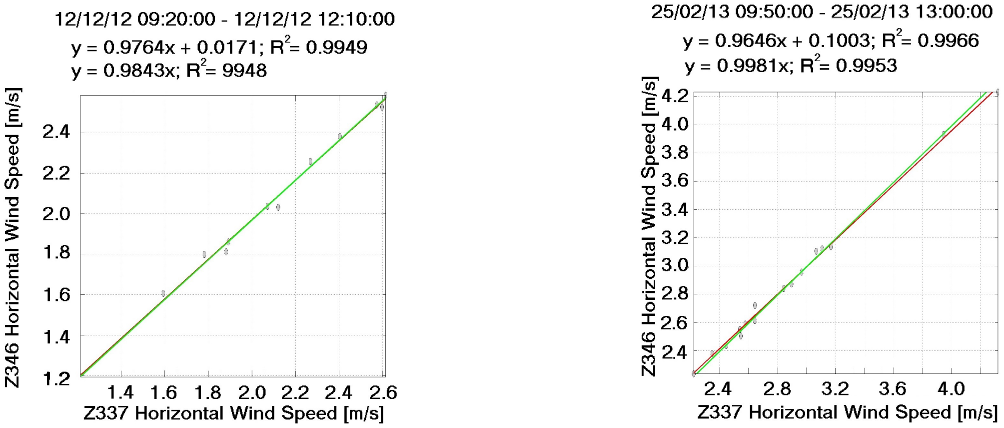

(a) (b)

Figure 3.20: 10-min HWS scatter plot for the moving lidar. (a) Blocked cardan frame. (b) Free cardan frame.

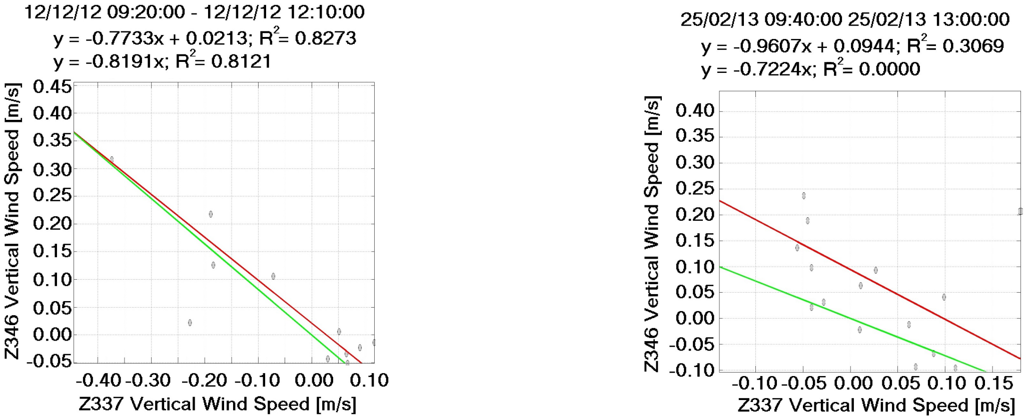

(a) (b)

Figure 3.21: 10-min VWS scatter plot for the moving lidar. (a) Blocked cardan frame. (b) Free cardan frame.

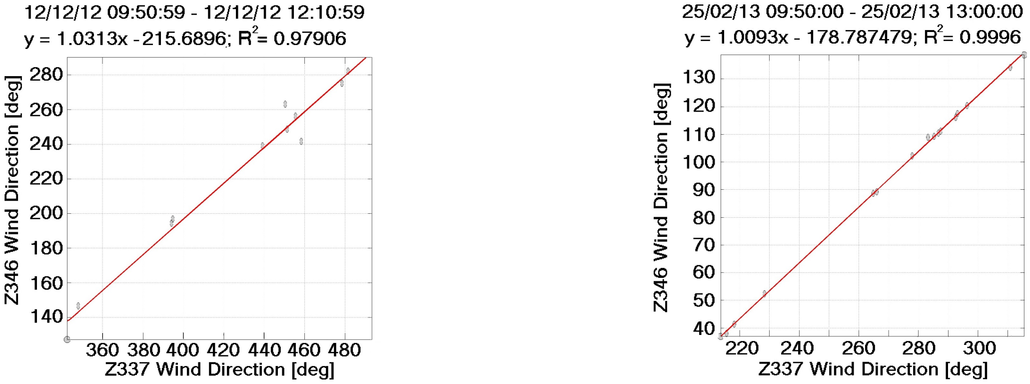

(a) (b)

Figure 3.22: 10-min WD scatter plot for the moving lidar. (a) Blocked cardan frame. (b) Free cardan frame.

3.3.2.C Overview of the moving lidar tests

Until now it has been presented test cases for specific conditions ($A = 16\ deg$ and $T = 12\ s$ for blocked- and free-cardan), this Section summarizes the rest of the tests carried out to analyze more general motion conditions. For reference, in Tab. 3.10 are presented the results for the calibration campaign with both lidars in the roof of the UPC (Figs. 3.2b and 3.2c) studied in Sect. 3.3.1 including without ("Raw") and with ("Corrected") the application of the delay-correction algorithm to be presented in Sect. 4.3.1.

This Table shows the values to be used as reference when analysing the impact of motion in the lidar measurements. It is observed that values very close to ideal correlation can be achieved for 10-min data but it will only be possible for 1-s data in moderate or low backscattering atmosphere.

Tab. 3.11 summarize the statistical parameters obtained during the rest of the test campaign at LIM-UPC.

- Regarding the *blocked-cardan-frame* tests, a clear deterioration in all the statistical parameters occurs for 1-s data. For example, the effect of angular motion (e.g., pitch amplitude, $A = 16\ deg$, period, $T = 12\ s$) the determination coefficient falls from 0.985 (collocated lidars, Sect. 3.3.1.A) to 0.71 (Tab. 3.11).

  For 1-s measurements there are no significant differences between the $T = 12\ s$ and $T = 6\ s$ motional periods, however, for higher frequencies ($T = 3\ s$) the statistical parameters worsen. Similarly, degradation of the statistical parameters increase with the angular amplitude.

  At 10-min time resolution good performance is also obtained when the cardanic frame is blocked for low angular amplitudes and low periods. For high angular amplitudes and short periods (i.e. pitch amplitude, $A = 25\ deg$, period, $T = 6\ s$) KPI are worsen.

- Regarding the *free-cardan-frame* tests, satisfactory motion compensation always obtained. This improvement usually implies fulfillment of the KPIS. For instance, a motion amplitude of 16 deg in pitch is reduced down to 2 deg (85% reduction), which causes the determination coefficient to improve from 0.71 to 0.94 (Tab. 3.11). Therefore, the cardan frame turn out a valuable mechanical motion compensation system to ensure the confidence at 1-s time resolution.

Table 3.10: HWS statistical indicators for the case of collocated/distant lidars (Sect. 3.3.1).

Resolution	Test Case	Bias	RMSE	Slope	Offset	R^2
1-s	General close range	-0.0489	0.5574	0.9903	0.1059	0.9572
1-s	Moderate Backscatter close range	-0.013	0.0867	0.9876	0.0479	0.9850
1-s	High Backscatter close range	-0.1438	0.8074	0.8692	1.2679	0.7369
1-s	Raw far range	-	-	0.9739	0.1511	0.9217
1-s	Corrected far range	-	-	0.9894	0.0757	0.9616
10-min	General close range	-0.0470	0.1308	1.0149	-0.0413	0.9975
10-min	General far range	-	-	1.0146	-0.0505	0.9974

Table 3.11: HWS statistical indicators. (Notation: Test case 10 deg, 12 s, indicates angular amplitude, $A = 10deg$ and period $T = 12s$).

Resolution	Test Case	Bias	RMSE	Slope	Offset	R^2
1-s	10 deg, 12 s, Blocked	0.0107	0.3398	0.8962	0.3884	0.8298
1-s	10 deg, 12 s, Free	-0.055	0.4756	0.9602	0.3213	0.9322
10-min	10 deg, 12 s, Blocked	0.0122	0.0400	0.9757	0.0811	0.9933
10-min	10 deg, 12 s, Free	-0.0488	0.0814	0.9676	0.2647	0.9917
1-s	10 deg, 6 s, Blocked	0.0145	0.3357	0.9146	0.3195	0.8207
1-s	10 deg, 6 s, Free	0.0210	0.3421	0.96087	0.1208	0.9309
10-min	10 deg, 6 s, Blocked	0.0096	0.0541	1.0248	-0.1058	0.9844
10-min	10 deg, 6 s, Free	0.0119	0.0279	0.99562	-0.0039	0.9990
1-s	10 deg, 3 s, Blocked	0.0146	0.7974	0.7357	1.2855	0.6240
1-s	10 deg, 3 s, Free	0.0328	0.3200	0.9094	0.22519	0.8661
10-min	10 deg, 3 s, Blocked	0.0080	0.0682	1.0653	-0.3292	0.9907
10-min	10 deg, 3 s, Free	0.0223	0.0362	1.0121	-0.0559	0.9970
1-s	16 deg, 12 s, Blocked	0.0289	0.3705	0.8358	0.3253	0.7126
1-s	16 deg, 12 s, Free	0.0063	0.1985	0.9567	0.1136	0.9434
10-min	16 deg, 12 s, Blocked	0.0347	0.0315	0.9763	-0.0171	0.9949
10-min	16 deg, 12 s, Free	0.0022	0.0374	0.9645	0.1003	0.9966
1-s	16 deg, 6 s, Blocked	0.0481	0.5957	0.8752	0.4059	0.7580
1-s	16 deg, 6 s, Free	-	-	-	-	-
10-min	16 deg, 6 s, Blocked	0.0412	0.0376	1.0060	-0.0642	0.9979
10-min	16 deg, 6 s, Free	-	-	-	-	-
1-s	16 deg, 3 s, Blocked					
1-s	16 deg, 3 s, Free	-	-	-	-	-
10-min	16 deg, 3 s, Blocked					
10-min	16 deg, 3 s, Free	-	-	-	-	-
1-s	25 deg, 12 s, Blocked	-0.0007	0.5172	0.83583	0.76188	0.6437
1-s	25 deg, 12 s, Free	-	-	-	-	-
10-min	25 deg, 12 s, Blocked	0.0848	-0.0463	0.99436	0.07126	0.9363
10-min	25 deg, 12 s, Free	-	-	-	-	-
1-s	25 deg, 6 s, Blocked	0.1963	0.5872	0.6792	0.5948	0.44204
1-s	25 deg, 6 s, Free	-	-	-	-	-
10-min	25 deg, 6 s, Blocked	-	-	1.0435	-0.2997	0.6718
10-min	25 deg, 6 s, Free	-	-	-	-	-
1-s	25 deg, 3 s, Blocked	-	-	-	-	-
1-s	25 deg, 3 s, Free	-	-	-	-	-
10-min	25 deg, 3 s, Blocked	-	-	-	-	-
10-min	25 deg, 3 s, Free	-	-	-	-	-

3.3.3 Buoy lidar sea tests with the cardan frame

Although previous lab-based experiments prove that the cardanic frame was a valuable device to compensate angular motion under pure senoidal excitation, real sea conditions in PdP cause the cardanic frame to amplify the angular motion of the buoy angular motion.

A physical model of the cardan frame as a composite pendulum is to be presented in order to analyse the performance of the cardan frame motion-compensation device as well as to understand this increase of the angular motion reported in the sea.

3.3.3.A Physical model of the cardan frame

This Section presents the physical model used to numerically simulate the behaviour of the cardan frame consisting of a simple compound pendulum with one degree of freedom excited by both titling and transversal accelerations of the buoy. Formally the 2nd-order differential equation for the physical pendulum takes the form (*Spieth*, 2013),

$$(m \cdot L^2 + I) \cdot \ddot{q} + d \cdot \dot{q} + m \cdot g \cdot L \cdot q = -m \cdot L \cdot \ddot{u} + d \cdot \dot{v}, \tag{3.1}$$

where m is the total weight of the lidar and the cardan frame, L is the distance from the Center of Gravity (CoG) of the lidar to the mounting axis of the cardan frame, g is the gravity constant and q is the angular amplitude. The right hand side terms of Equation 3.1 are the pendulum forcing terms with $m \cdot L \cdot \ddot{u}$ corresponding to the translatory excitation and $d \cdot \dot{v}$ to the rotational excitation.

From Equation 3.1 the natural frequency of the non-damped oscillator can be obtained as (*Spieth*, 2013).

$$f = \frac{1}{2\pi} \sqrt{\frac{m \cdot g \cdot L}{m \cdot L^2 + I}}. \tag{3.2}$$

3.3.3.B Results

Departing from the model formulation of Sect. 3.3.3.A and the lab test described in the preceding sections, the final part of the study was the evaluation of the cardan frame compensation in real sea conditions. To that end the moving lidar with its cardan frame was installed at PdP, nearby the fixed lidar that would be used as reference (Chap. 4).

As in the previous lab tests the motion of the buoy and the lidar was monitored by using two IMUs. In contrast to the lab tests with the motion simulator platform, the offshore tests showed that the cardan frame, in the configuration described in Tab. 3.1 did not compensate for the wave movements but even amplified them instead (Fig. 3.23a, blue and green traces). Buoy and lidar-motion data were analysed to investigate the reasons for this amplification. By analysing roll data in the time domain it becomes clear that the cardan frame amplifies the amplitude of the wave movement (Fig. 3.24). By looking at Fig. 3.23a frequency plot, one can see that the magnitude of the spectrum of the "lidar data" is significantly higher and the peak is shifted from around 0.4 Hz to 0.6 Hz. This leads to the conclusion that the eigen frequency of the cardan frame system (i.e., natural frequency of vibration) is at 0.6 Hz (see Equation 3.2) which causes that the system goes into resonance when excited at this frequency.

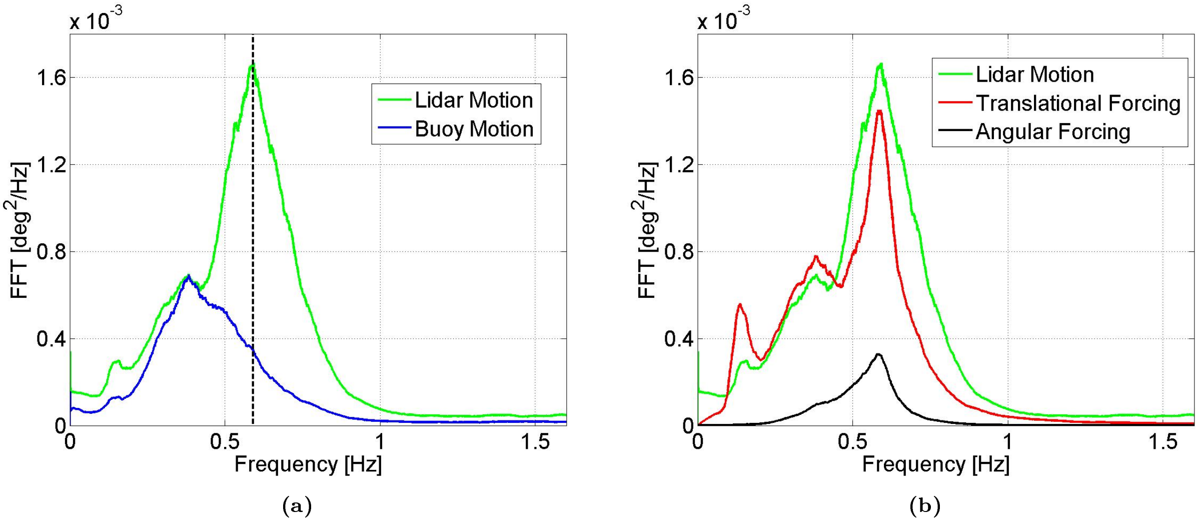

(a) (b)

Figure 3.23: Analysis and model validation of the roll-angle Fourier spectrum. (a) roll spectrum of the buoy (blue line) and the lidar (green line) measured at PdP Campaign (23/05/2015 00:00 to 00:15). (b) Model validation: Spectrum in response of only-translational excitation (red line) and only-rotatory excitation (black line) of the cardan frame.

From model Eqs. 3.1-3.2 a second analysis was carried out to find out which kind of excitation, translational or rotational, was responsible for the resonance problem of the cardan frame. Towards this end the model was simulated first with only translational excitation and, second, with only rotational excitation. The results are shown in Fig. 3.23b and they clearly show that mainly translational excitation mainly leads to an amplification of the roll movement of the lidar. The same holds for the pitch angle.

The third step in this study has been to find a new set of configuration parameters for the cardan-frame in order to optimize its dynamic response and, consequently, to reduce the lidar motion angular amplitude. To investigate the influence of the different cardan frame parameters a parameterised study was carried out. The parameters analysed were the distance L of the CoG of the lidar to the rotational axis of the frame as well as the damping coefficient d. The optimized configuration is summarized in Tab. 3.1. According to the model simulations, a best solution to avoid the resonance phenomenon is to reduce the distance between the lidar CoG and the rotational axis of the frame as much as possible (e.g., $L = 0.5\ mm$) while reducing the damping up to $d = 5\ N\ m\ s/rad$.

Finally, Fig. 3.24 shows the time and frequency response of the optimized cardan-frame configuration, for the lidar roll angle.

3.4 Conclusions

This chapter has shown the motional tests carried out during the development phase of the commercial floating lidar prototype.

- The *calibration tests* with both lidars fixed (Sect. 3.3.1) have shown that time intervals with

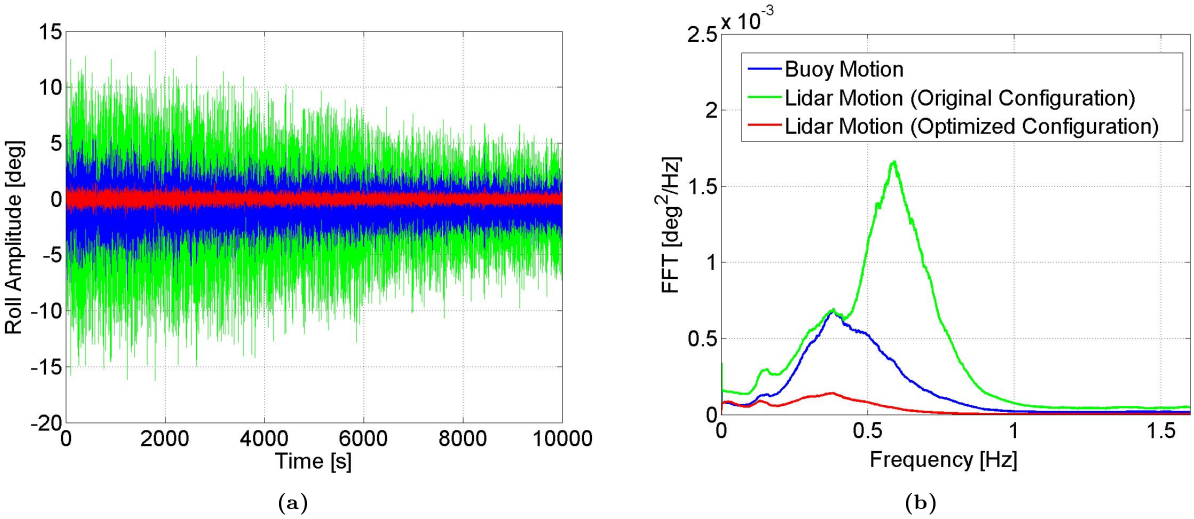

Figure 3.24: Time and frequency response of the optimized cardan frame configuration for the lidar roll angle. (a) Time domain. (b) Frequency domain and comparison with the original configuration and buoy motion.

high backscatter levels and spatial variability seriously degrade the *1-s* HWS, VWS, and WD correlation between both lidars. Backscatter levels and SV lower than 3 [units] and 0.05 [units], respectively, must be guaranteed in order to ensure statistical parameters within the KPI acceptance criteria of Tab. 2.3 (i.e., $R^2 > 0.96$).

Concerning *10-min* HWS data the KPI clearly lie within the acceptance region.

When cross-examining *10-min* WD and VWS data from the two lidars it is necessary to segregate into three phase-difference clusters: 0, +180 and -180 deg. The determination coefficients thus obtained for the WD are greater that 0.998 (Fig. 3.9b) while the determination coefficients obtained for the VWD are 0.97 (0-deg phase difference), 0.75 (+180 *deg*) and virtually 0 (uncorrelated, −180 *deg*) in Fig. 3.10b. Though these values cannot be given as typical ones, similar trends are reencountered when examining the whole measurement test campaign database. In Chapter 5.2 an algorithm to solve this behaviour is presented and evaluated.

- Regarding the *delay correction algorithm* applied to 1-s data it can be concluded that due to complex terrain at UPC premises, 50 m is the maximum separation between lidars that allows to comply with the KPIs. For 10-min data, larger separations are still possible without worsening statistical indicators out of the acceptance region.

- In *Laboratory cardan-frame tests*, for a pitch amplitude $A = 16$ *deg* and period $T = 12$ s at 1-s temporal resolution, there is clear deterioration in all the evaluated statistical parameters (bias, RMSE, slope, offset and determination coefficient) below the required KPIs. Without mechanical compensation the HWS time series from the “moving” lidar highly fluctuates around the “fixed”-lidar signal. The period of these fluctuations coincides with that of the applied motion. In contrast, when the cardan frame is free to rotate the HWS time series evidences that the cardan frame virtually filters out the fluctuations due to platform motion

. As a result, when the HWS from both lidars is compared distribution is less scattered (i.e., RMSE reduces) and the determination coefficient approaches unity. For example, oscillatory amplitude of 16 *deg* is reduced to 2 *deg* (85% reduction). For the 10-min data the impact of platform motion does not become relevant.

The cardan frame as motion-compensation solution during the *buoy lidar tests* has been studied and optimized. Performance has been analysed from HWS scatter plots of the reference lidar (“fixed”) and a “moving” lidar on a pitch/roll motion-simulation platform (wave periods in the 3-to-12-s range and angular amplitudes in the 10-to-25-deg range).

- Finally, simulations *physical model* of the simple compound pendulum with one degree of freedom (either pitch or roll angle) has shown to fairly reproduce roll-angle spectrum at the offshore test campaign at PdP. This pendular model becomes a comparatively simple and straightforward analysis tool. Linked to this model, a final outcome has been the optimization of the length, moment of inertia, and damping coefficient of the cardan frame when installed on the prototype lidar buoy (Tab. 3.1).

Chapter 4

El-Pont-del-Petroli test campaign and filtering techniques

This work provides a signal-processing and statistical-error analysis methodology to assess the accuracy of a floating Doppler wind lidar. The study introduces the raw-to-clean data processing chain, error assessment indicators and KPIs, as well as two filtering methods at post-processing level to alleviate the impact of angular motion and spatial variability of the wind flow on the performance indicators. Towards this aim, the study mainly revisits HWS and TI measurements with a floating ZephIR 300 lidar buoy during a 38-day nearshore test campaign in PdP (Barcelona). Typical day cases along with overall statistics for the whole campaign are discussed to illustrate the methodology and processing tools developed.

The contents of this Chapter are a combination of the journal paper, *Gutiérrez-Antuñano, Tiana-Alsina, and Rocadenbosch* (2017) “Performance evaluation of a floating lidar buoy in nearshore conditions”, `https://onlinelibrary.wiley.com/doi/abs/10.1002/we.2118`, submitted to Wind Energy, and peer-review conference paper, *Gutiérrez et al.* (2015), 2015 (available at the IEEE Xplore website `https://ieeexplore.ieee.org/document/7326228`).

4.1 Introduction

Alternatively to the mechanical-compensation method described in Chap. 3 (i.e., the cardan frame) one could try to reduce motion-induced errors by recording the buoy dynamics (i.e., its attitude) and by using *numerical algorithms* that help to correct the measured wind data. The residual uncorrected effects of such errors not only translates into additive noise to the measured wind signal but also as an “extra” turbulence (*Courtney and Hasager*, 2016). To this end, in this chapter is shown successful results from an *original motion-compensation algorithm* based on adaptive window averaging, which is analysed in both the temporal and spectral domains.

First, the processing workflow from level-0 data, i.e., the data acquired by sensors of interest (reference and moving lidars, and IMU sensors), to level-2 data, i.e., motion compensated will be presented.

In this work, discussion on the different error sources (e.g., motional versus turbulent) that degrade wind field measurements are presented, as well as the spectral analysis (*Proakis and Manolakis*, 2006) to validate the filtering methods applied, all of which is to contribute scientific novelty (*Sathe et al.*, 2011). This is a vast field of research that has also given rise to a wealth of simulation studies with synthetic turbulent wind files in the state of the art (*Gottschall et al.*, 2012b) (*Cool*, 2016).

In accordance with recommended practice (KPIs versus data availability) (*Carbon Trust*, 2013) and a growing maturity of floating lidars, a further contribution of this work concerns the methodological aspect with focus on the post-processing stage. Thus, departing from a 38-day nearshore campaign, system performance is assessed by using 1-s and 10-min time-series statistical analysis (*Proakis and Manolakis*, 2006). 1-s analysis (less usual in the state of the art) is to enable a better understanding of the involved phenomena, particularly, motion and turbulence.

In this Thesis is analysed a 38-days period from the near-shore measurement campaign carried out at PdP, Badalona, Barcelona (Spain), May 2nd 2013 - July 26th 2013, which was the key previous step towards the development of buoy prototype EOLOS. The correlation degree between two ZephIR 300 Doppler wind lidars measuring, one on a fixed platform on-shore (in what follows, the “reference” lidar) and the other on a proof-of-concept buoy (the “floating” lidar), will be cross-examined in terms of the retrieved HWS and TI at 100 m in height. Microstrain 3DM-GX3 IMUs were used to monitor the movement of the “floating” lidar.

4.2 Field Experiment Set-Up

Wind measurements from two ZephIR 300 lidars were intercompared at PdP facilities (41°26’24.5760”N 2°14’56.5008”E), Badalona, Barcelona, Fig. 4.1a (*Sospedra et al.*, 2015). The physical environment consists of metropolitan low-rise buildings (typically, 20-m tall) along the coast line. The PdP area is part of the commuter belt of the city and the spatial organization of its settlements follows urban typology. One of the lidars was on a stand still configuration on land (i.e., the“reference” lidar), and the other was assembled on a buoy (i.e., the “moving” or “floating” lidar), as shown in Fig. 4.1b. Fig. 4.1c shows the prototype buoy. The cardan frame, painted in black can be seen in the upper part, as well as the sonic anemometer of the lidar and other safety devices.

The fixed lidar was the key reference instrument used in PdP campaign. The lidar was directly rented to the manufacturer (ZephIR Lidar) and, as part of the Quality Assurance (QA) program, before and after PdP campaign it underwent QA tests against an IEC 61400-12-1-compliant met mast. Besides, both lidars (i.e., the “reference” and the “floating” one) were placed fixed on land 1-m apart during 3-h intercomparison periods before and after PdP campaign in order to verify identical measurements under 1-s and 10-min time basis. These tests were performed at the PdP pier so as to have topographical and environmental conditions as close as possible to those of the offshore campaign.

PdP includes a full meteorological station mounted on a tower at the end of the pier including a NORTEK Aquadopp© underwater current meter (5 m depth), a SBE 37-SM C-T pressure sensor, a Vaisala HMP-155 temperature and humidity probe, a LP02 Young 52203 rainfall sensor, a Gill Instruments WindSonic anemometer, and a Vegapuls 62 radar-based sea-state and water-height

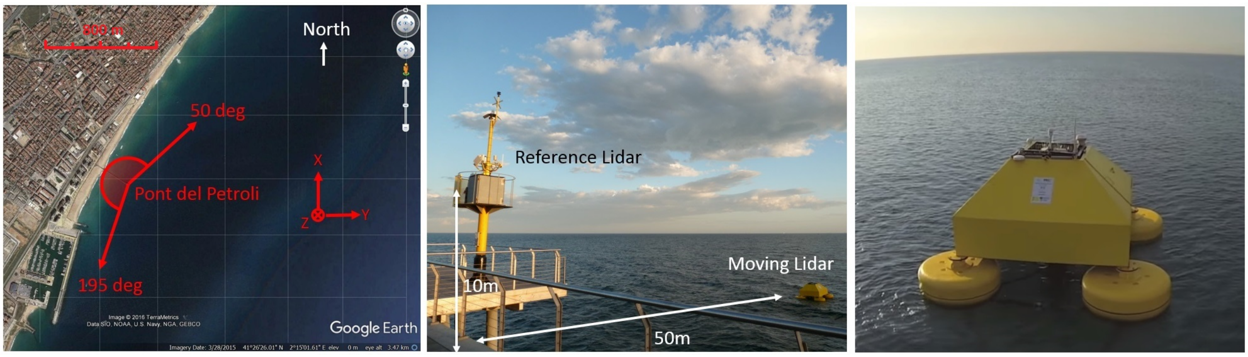

Figure 4.1: PdP test campaign site. (a) Location of the test site near Barcelona coast. Red vectors along NE and SSW directions delimit the angles of the circular sector influenced by land. Fixed Cartesian coordinate system used as part of the fixed reference frame is also shown. (b) Meteorological tower and prototype lidar buoy. (c) Picture of the prototype lidar buoy

measurement device. Webcams are also installed for both safety and beach-line monitoring. A WiFi link connects these sensors to an office computer on a nearby building and from there to the Internet, so that data gathered by all these instruments can easily be accessed, along with their performance, on a real-time basis.

Because the buoy housing the ZephIR 300 lidar was a proof-of-concept custom-made system developed for this purpose, it was powered by a submarine electrical power cable connected to PdP which also sent data to a datalogger installed in the support tower in the dock. The buoy integrates the “floating” ZephIR 300 lidar as well as the two IMUs described in Sect. 4.3.1.

The PdP campaign extended from May 24th, 2013 to June 31st, 2013, i.e., during the late spring / early summer period. Weather at this time of the year is dominated by local thermal winds not going over 15 m/s speeds at 100 m in height although occasional episodes of terrestrial wind blowing from the north may occur. Heavy eastern storms seldom happen to blow in early summer and, in fact, none did so during the campaign. During the campaign wind speeds ranged from 1 m/s to 15 m/s at 100 m in height (see Fig. 4.2a) with three predominant directions: from the South, from North East and from the North-West (see Fig. 4.2b). Typically, during the night, there is light land breeze (3-4 m/s) blowing from land to sea (WNW direction in Fig. 4.2b) and characterised by more turbulent behaviour than day wind. During the day, there is usually sea breeze blowing from sea towards land (NE and SSW directions in Fig. 4.2b) of higher intensity (4-7 m/s) and lower turbulence (see also Fig. 4.3a). The average wind blowing pattern along with the lidar-observed SV over the 38-day campaign is shown in Fig. 4.3. Because Fig. 4.3c represents the 38-day average WD, when Fig. 4.3c is compared to Fig. 4.2b the reader will notice that the 300-deg WD in Fig. 4.3c between approximately 0-5h UTC corresponds to the WNW direction in the wind rose of Fig. 4.2b. In contrast, the rough 120-deg WD for 7-20 h UTC time interval corresponds to the average of NE ($\approx$ 50 deg) and SSW ($\approx$ 195 deg) WDs in Fig. 4.2b.

Concerning atmospheric stability, (*Wharton and Lundquist*, 2012) came up with classification thresholds interrelating stability parameters (e.g., TI, Turbulent Kinetic Energy (TKE) and the like) and stability class conditions. From this background and using that, for this site, the lidar-observed SV parameter is well correlated with the lidar-observed TI (this assertion will be further discussed in Sect. 4.3 and Fig. 4.6), it emerges from (Fig. 4.6a) that for this site low SVs (SV $\approx$ 0.02 roughly related to TI $\approx$ 5%) are associated to stable conditions while high SVs (SV $\approx$ 0.05 related to TI $\approx$ 15%) are associated to convective ones. No fog or low-cloud events occurred during the campaign.

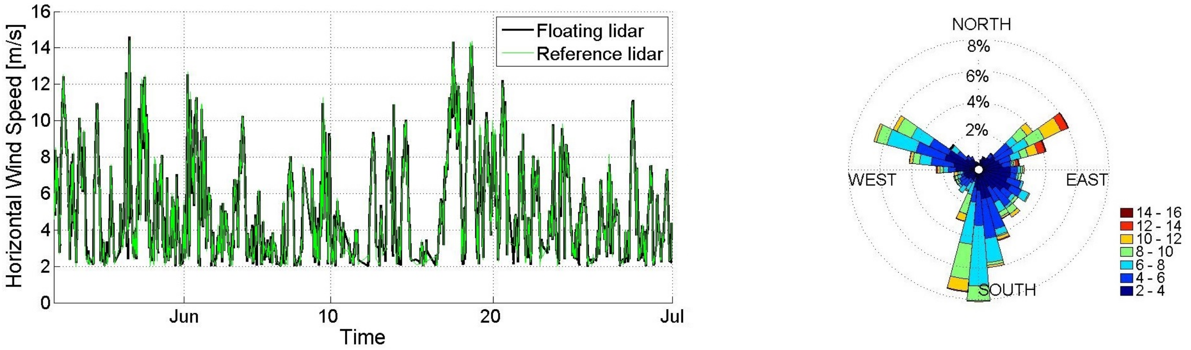

Figure 4.2: HWS time series and synoptic description of the wind flow at the test site during PdP campaign at 100 m in height. (a) 10-min HWS time series. (b) Wind rose showing 10-min WD bins for the reference lidar. Wind speeds below 2 m/s have been removed according to outliers' criteria (*Carbon Trust*, 2013).

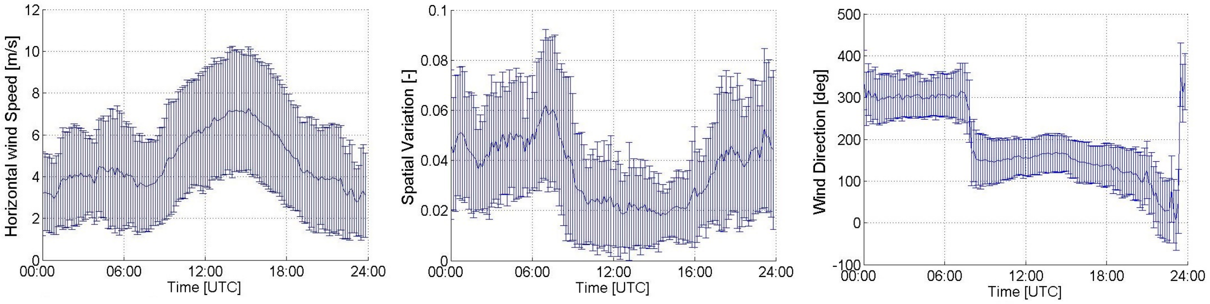

Figure 4.3: 38-day average wind patterns during the daily cicle. (a) HWS, (b) SV and (c) WD. Note: Time is UTC. Errorbars are computed at 1σ from 10-min data.

Fig. 4.4 color codes these measurement scenarios by plotting the number of events associated to a given 10-min HWS (Y-axis) as a function of buoy angular-motion amplitude (X-axis), defined as the modulus of the maximum pitch or roll angular amplitude of the "floating" lidar.

4.3 Assessment Methodology And Data Processing

The methodology and signal processing tools aim at cross-examining wind-measured data from the "reference" lidar and the "floating" lidar previously introduced. Aim is to statistically describe and quantify motion-induced error on the retrieved wind parameters, namely, HWS, WD, and TI. Fig. 4.5 block diagram summarizes the post-processing steps used in this approach, from level 0 (1-s data) to level 2 (post-processed motion-compensated data).

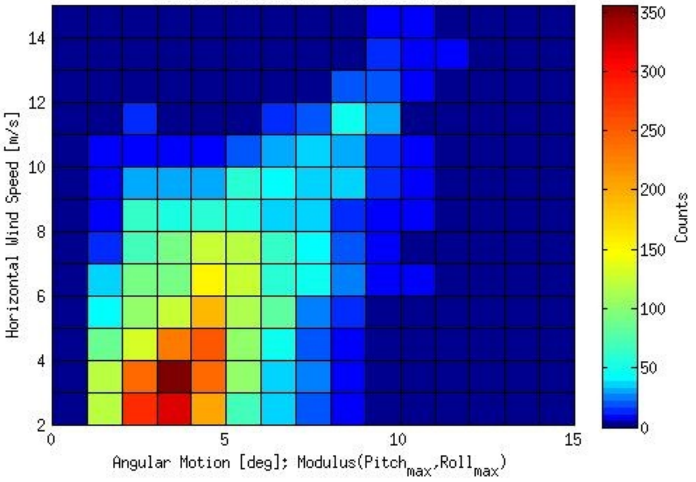

Figure 4.4: Color plot representing the number of 10-min datasets ("counts") per HWS bin and angular motion bin from 25/05/2013 to 31/06/2013.

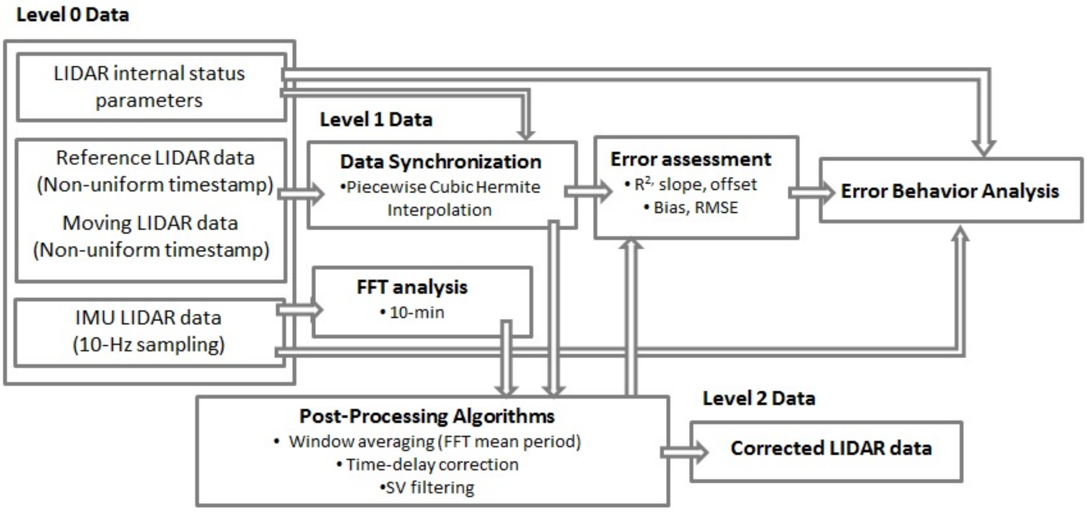

Figure 4.5: Wind lidar signal-processing block diagram.

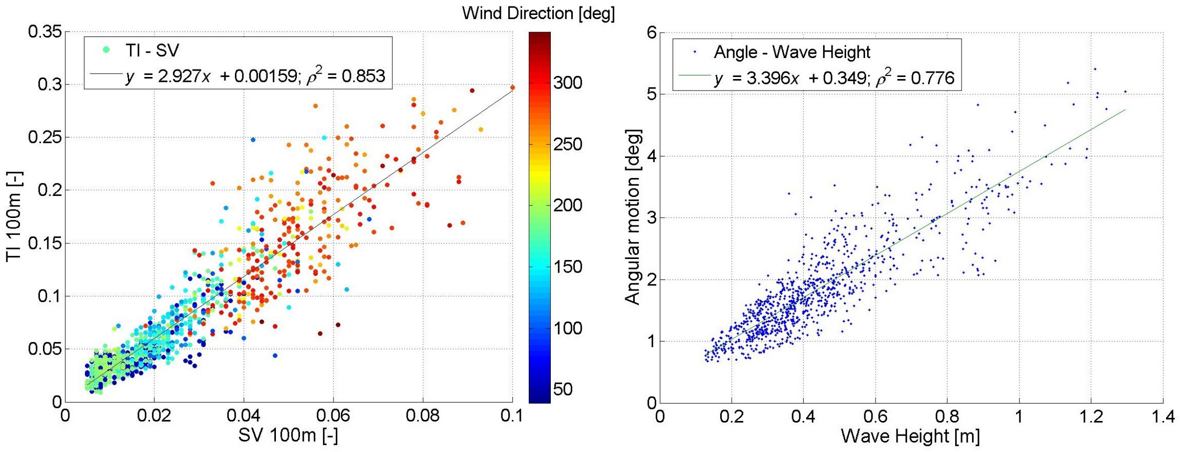

Figure 4.6: (a) Scatter plot showing SV-TI correlation (100-m in height). Each dot represents 10-min data computed from the available 38-day 1-s PdP-campaign dataset. Dots are color-coded according to WD. (b) Scatter plot showing the correlation between the wave height and buoy angular-motion parameter, $AM = \sqrt{\alpha^2 + \beta^2}$ [deg]. Wave height has been measured hourly. Angular motion has been computed hourly from IMU data by averaging six 10-min samples every hour.

4.3.1 From level-0 to level-1 data

Raw data.- Raw data comprises: (i) wind-lidar data from the Doppler lidar instrument, (ii) lidar internal status parameters and (iii) "floating" lidar motion time series gathered by the IMUs. Wind-lidar data includes HWS, WD, VWS as well as the lidar-observed TI.

TI magnitude highly depends on the location, the fetch, the measurement height and HWS, but typical values of horizontal TI, measured in offshore wind farm locations at 50-m height and above 10 m/s HWS, are around 8% to 10% (*Nino and Eecen*, 2001). An important remark to be mentioned here is that the *lidar-observed* TI figure is not completely equivalent to the *true*-TI measured by point-like ultrasonic or cup anemometers. This is due to the fact that the lidar-observed TI is affected by the inherent spatial and temporal averaging of the measuring instrument, which is directly linked to the spatial and temporal resolution window of the instrument (*Sjöholm et al.*, 2010)(*Wagner et al.*, 2009). Thus, in the case of the CW ZephIR 300, the measurement at a given height requires focusing the lidar beam at that height, which means that the instrument measures the average of the ensemble of radial velocities in the sounding volume determined by the laser beam and a probe length equal to the depth of focus (the probe length increases with the square of the focus distance). A similar and second-order effect is due to the conical scanning mechanism and related wind-component retrieval algorithm (VAD), which causes a portion of the scanning circle to be spatially averaged. These volume averaging effects cause that the lidar filters out turbulent scales smaller than the probe length and that it estimates standard deviations about 80% of the true value measured by cups in flat terrain (*Wagner et al.*, 2009). Differences between the lidar-observed and the true wind spectrum will be discussed in Sect. 4.4.3.

Lidar internal status parameters are also part of the raw data available and they are used to assess wind data. These status parameters are the SV, the backscatter (i.e., the intensity of the attenuated backscattered light return), and secondary system parameters. The SV parameter, also called turbulence parameter (TP), has been considered "black box" insofar as it is related to the

TI, which justifies the SV-TI correlation study conducted in following sections.

IMU data enables to track the "floating" lidar attitude. It has used a Microstrain 3DM-GX3-45 IMU equipped with a GPS antenna. Attitude data includes Euler angles (roll, pitch and yaw), which describe lidar system orientation with respect to a fixed-coordinate system (see Fig. 4.1a), translational accelerations on these axes, and GPS position of the buoy. IMU acquisition frequency can be adjusted between 1-10 Hz to match that of the wind lidar data.

The above lidar-related variables are acquired at 100 m in height and at two different time resolutions, 1-s and 10-min (except for the TI which is calculated every 10-min from 1-s datasets). 10-min is the usual time basis used in the wind industry, while the 1-s time basis is used here to better understand error behaviour and its compensation. 10-min data availability was 100% for the reference lidar and 99.98% for the floating lidar. After eliminating outliers - as signaled by lidar internal status parameters (999X labels, too high wind speeds, rain, etc.) - data availability became approximately 90% for both lidars. Rejection percentage due to external parameters was around 15% due to low wind speeds.

Data synchronization and time-delay correction.- The ZephIR 300 lidar acquires and outputs data under a non-uniform time basis close to 1-s. Because of internal system protocols (e.g., cloud averaging and refocusing actions) the output data stream at one particular height may contain time gaps of several seconds and a non-uniform sampling period roughly between 1 and 5 s. First, *data synchronization* becomes necessary to compose and intercompare wind-related data streams (e.g., HWS, WD, pitch and roll) from the two different lidars. This is accomplished by first creating a master time vector with a uniform timestamp common to all the sensors involved (mainly the two lidars and the IMUs). Towards this end, 1-s linear and piece-wise cubic Hermite interpolation methods (*Taylor*, 1938) have been used to resample the time vector of all the sensors into the common time vector. For both methods, identical results have been obtained. Time gaps equal to or larger than 10-s have been marked as "signal drop outs" in the master time vector when computing statistics. Second, a *time-delay correction* is necessary to intercompare high time resolution wind lidar data (e.g., 1-s HWS) from the two lidars separated a given distance. The application of this method to the "Distantly-spaced lidars" (Sect. 3.3.1) is illustrated by Fig. 4.7.

The time delay is estimated by standard cross-correlation analysis of the time delayed signals (i.e., the time shift yielding maximum correlation between the "floating" and the "reference" signals),

$$\Gamma_{cross}(\Delta t) = \frac{\langle (s_1(t) - \mu_{s_1})(s_2(t+\Delta t) - \mu_{s_2}) \rangle}{\sigma_{s_1}\sigma_{s_2}}, \tag{4.1}$$

where Δt is the estimated delay or lag time, μ_i is the mean value of signal s_i, and σ_{si} is the standard deviation. The underlying principle here is Taylor's frozen atmosphere hypothesis (*Taylor*, 1938), which states that turbulent eddies transported by the mean wind flow do not change their properties but remain unchanged as if they were frozen. By applying this methodology to wind data measured by a "floating" and "reference" lidar level-1 data is obtained and the HWS time series measured by the two lidars can be intercompared.

The time shift applied to the lidar signal significantly improves the correlation degree between

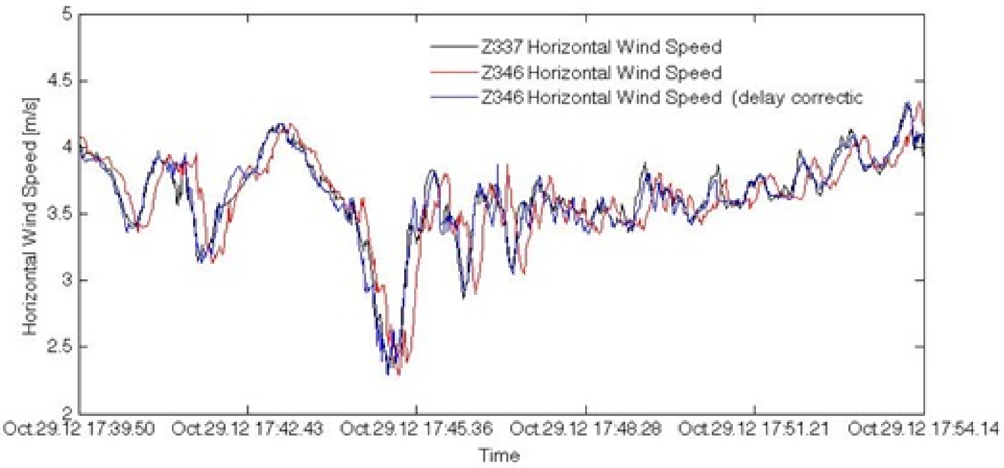

Figure 4.7: Delay correction corresponding to "Distantly-spaced lidars" test (1-s resolution).

lidar units. In the case example of Fig. 4.8 in which the two fixed lidars are 50 m apart, an improvement of about 4% in the correlation coefficient is achieved (i.e., R^2 goes from 0.9217 to 0.9616). Correlations as good as in the close-range test presented before could not be obtained probably because the assumption of horizontal homogeneity at 1-s temporal resolution begins to fail for comparatively large distances (around 50 m).

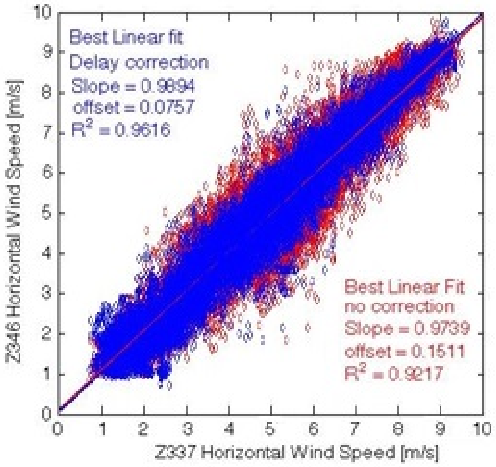

Figure 4.8: Delay-corrected scatter plot corresponding to "Distantly-spaced lidars" test.

Two off-the-shelf variables have been used to aid the error assessment study: SV and the so-called angular-motion parameter. The former is related to the lidar-observed TI, the latter to the buoy angular motion. They are explained next:

On the SV-TI correlation.- The so-called TP or SV parameter represents the variation degree -turbulence- of the radial wind speeds (LoS) within the circle of scan (*Wagner et al.*, 2009). Following (*Wagner et al.*, 2009), the SV parameter is defined as the TI of the radial wind speed over one rotation of the conically scanning lidar (see Eq. (12) therein). From a statistical point of view, it may be understood as an indicator of the goodness of the VAD fitting of the radial velocities within the scanning circle used to retrieve the estimated wind vector at a given height.

In order to closely study the SV-TI at one particular height (100 m here) an empirical SV-TI correlation study has been carried out by using 1002, 10-min measurements from the whole PdP campaign. To enhance the representativeness of the statistical sample, each measurement was chosen by ensuring that all other measurements within a 1-h window centered on the sample measurement (i.e., sample measurement ±30 min) were also compliant with outliers' criteria (*Carbon Trust*, 2013) and the lidar's manufacturer reliability specification (basically, HWS ≥ 2 m/s and exclusion of 999X labels). The lidar-observed TI has been computed over 10-min intervals and (SV, TI) pairs have been color-coded according to WD. Fig. 4.6a clearly shows that these two parameters are highly correlated (determination coefficient, $\rho^2 = 0.853$). Closer inspection of Fig. 4.6a reveals that mid-to-high values (i.e., (SV, TI) pairs above the (0.035, 0.1) point, shown by orange-reddish dots) are linked to WDs $\approx$ 270-300 deg. These WDs correspond to winds coming from the urban area (land breeze, Fig. 4.1a), which is consequent with higher terrain roughness due to the settlement of buildings along the coastline (*Belu and Koracin*, 2013).

On angular-motion parameter.- In this work angular motion (AM) parameter is a buoy-related parameter defined as the RMS of the pitch and roll angular amplitudes ($AM = \sqrt{\alpha^2 + \beta^2}$, where α is the pitch RMS angular amplitude and β is the roll one). The angular-motion parameter correlates well with the ***wave height*** as shown by a determination coefficient, $\rho^2 = 0.776$, in Fig. 4.6b. Selection of the angular-motion parameter as one of our primary variable of study instead of wave height (which is traditionally used as a key parameter to assess candidate wind-farm locations) is motivated by three main reasons: (i) availability of the angular-motion parameter with a much higher temporal resolution (10-Hz IMU sampling rate, i.e., 100-ms resolution) than the wave height (1-h resolution from the wave-height sensor); (ii) the fact that the angular-motion parameter is a direct measurement of the buoy motion (via pitch and roll angles) and hence, of the floating lidar motion; (iii) the availability of pitch and roll angles as individual time series from the IMUs, which enables a more in-depth knowledge of the buoy's temporal motion and in relation to WD.

4.3.2 Filtering methods

Motion-compensation algorithms.- In order to reduce the impact of sea-induced angular motion (pitch/roll) on the retrieved wind speed measured by the floating lidar, motion compensation at post-processing level becomes necessary (*Gottschall et al.*, 2012a) (*Bischoff et al.*, 2015). Fig. 4.9a shows the 1-s HWS measured with the floating lidar (blue dots) and that of the reference lidar (black trace). While the HWS standard deviation for the reference lidar is $\sigma_{ref} = 0.36$ m/s over a 24-h period starting on June 18th, 2013, the standard deviation for the floating lidar becomes as high as $\sigma_{float} = 0.74$ m/s. Different motion-compensation approaches can be considered depending on whether LoS data is available or not to the correction procedure:

Individual LoS correction.- This procedure takes advantage of the fact that the VAD algorithm combines multiple LoS to estimate the wind-speed components ((u, v, w), being each one the projection of the wind vector along the x, y and z axis, respectively). Thus, in the case of the ZephIR lidar, 50 LoS are combined in each conical scan at a frequency of 1 scan/s. It is possible to deconvolve lidar motion in the radial velocity measured along each LoS by using Euler-angle formulations (*Arfken*, 1985) and given attitude time series data (pitch and roll information). Because the geometry of the problem is known for each scanning LoS, the problem is invertible. From the point of view of its practical implementation this approach implies the prerequisite of individual LoS data being available (*Schlipf et al.*, 2012).

Motion-induced variance estimation.- This methodology assumes a constant wind field and a set of buoy motional conditions in order to estimate the motion-induced HWS variance. This is a research contribution of this Ph.D. ot be discussed in Chap. 6.

Window averaging.- When LoS data is not available, as is our case, a most suitable correction strategy consists of filtering out motion-induced signal fluctuations recorded under 1-s time basis (see Fig. 4.9). Window averaging is a class of low-pass filtering (or smoothing) techniques (Sect. 4.3) inherited from the Signal-Processing field (*Proakis and Manolakis*, 2006) that enable to filter out unwanted high-frequency components on the measured HWS such as those caused by motion of the floating lidar.

In this work is proposed an *adaptive window averaging* of the HWS as motion-compensation algorithm. This straightforward post-processing technique relies on a simple boxcar low-pass filter of adaptive length that enables to filter out unwanted high-frequency components such as those caused by the motion of the floating lidar. The time window length is chosen to be the mean oscillatory period of the buoy/platform, which is estimated by Fast Fourier Transform (FFT) of the buoy angular motion measured by the IMUs (Fig. 4.9b) and recomputed every 10 minutes. Thus, each FFT is computed by using 6000, 10-Hz time-spaced samples (10-min time segment) and zero padding until reaching 8192 samples (nearest power of two, 2^{13}). From Fig. 4.9b (11:20 to 11:30 LT time segment) the motional behaviour of the buoy is dominated by a pitch-angle peak frequency, $f = 0.25$ Hz. Thus, it corresponds to a mean oscillatory period (window length) equal to $T = 1 / 0.25 = 4$ s. Fig. 4.9a illustrates application of this FFT-based window averaging from the temporal point of view (time-series processing). It is evidenced that once the window-averaging algorithm is applied to the floating lidar HWS signal (blue dots) random fluctuations significantly reduce and hence, the "floating" lidar HWS signal (red dots) becomes closer to the reference-lidar HWS (black trace).

Window averaging technique has proven effective enough to minimize the impact of wave-induced motion on lidar performance by (i) reducing the width of the error histogram spectrum of 1-s HWS from $\mathrm{RMSE}_{float} = 0.6327$ m/s to $\mathrm{RMSE}_{window} = 0.3665$ m/s (Fig. 4.10) and (ii) improving the TI correlation offset between the reference and the floating lidar from $b_{float} = 0.049$ to $b_{window} = 0.006$ (Fig. 4.11) .

Analogous behaviour is reencountered from the spectral point of view (this is amply discussed in Sect. 4.4.3 in the context of wind spectrum analysis).

SV filtering.- As introduced above, the SV parameter represents the wind variability in the scanning area. Coast-line terrain complexity nearshore the test site plays a non-negligible role in the variability of the wind flow at PdP. This is to say that SV may well impair statistical confidence indicators between the two lidars even if the floating lidar did not move. Therefore, and as the second step to come up with SV-compensated data apt for fulfilling wind-energy industry

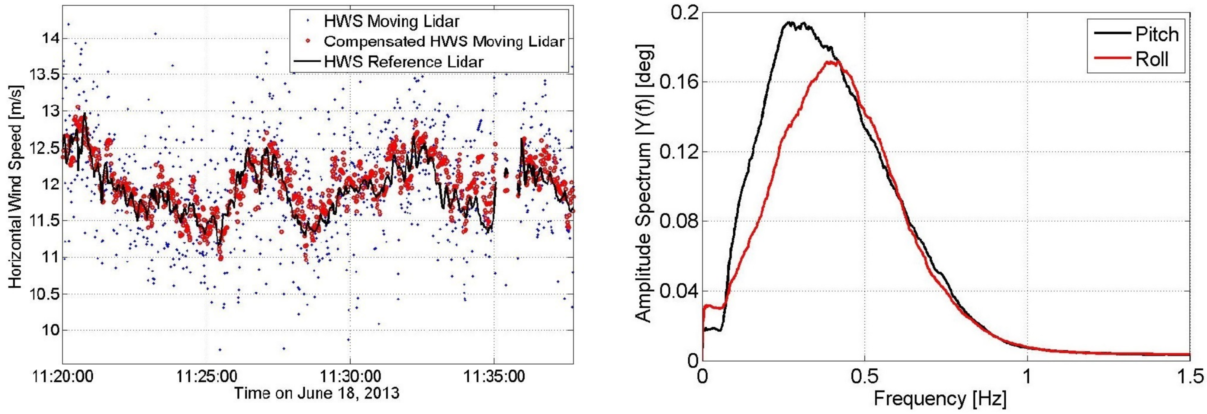

Figure 4.9: The adaptive window-averaging algorithm: (a) 1-s HWS time series measured by the "reference" lidar (black trace) and by the "floating" lidar (blue dots). 1-s HWS after window averaging (red trace). (b) Pitch and roll FFT of the buoy angular motion computed from the 10-min time segment starting at 11:20 LT and showing peak-dominant oscillatory behaviour at at peak frequency, f = 0.25 Hz.

requirements, a SV-threshold filtering is applied. Fig. 4.12a shows the 1-s SV histogram for two representative days corresponding to low- and high-SV scenarios. Fig. 4.12b depicts the SV for the whole PdP campaign computed with 10-min data. In both panels the SV threshold (0.05 and 0.1, respectively) is used to remove HWS measurement samples above the threshold. The threshold used for 10-min data is in agreement with (*Arranz*, 2011).

4.4 Discussion Results

This Section is aimed at illustrating that the proposed assessment methodologies of Sect. 2.3 is suitable for characterizing the HWS error behaviour of the floating lidar in terms of angular motion and lidar-observed wind turbulence (parameterized by the SV) as main error sources. Moreover, is presented a summary statistical analysis for the whole 38-day PdP campaign, representative of the two filtering methods presented in Sect. 4.3.2, used to comply with the acceptance criteria and KPI indicators of Tab. 2.3. Finally, and because of the importance of the TI for the wind industry, it is shown how the measurement reliability of the TI can be improved by application of Sect. 4.3 methods.

4.4.1 Quality of the reference lidar

Fig. 4.13 shows 1-s and 10-min HWS intercomparison tests before and after PdP campaign, when both lidar units where fixed. As mentioned in Sect. 4.2 both the "reference" and the "floating" lidar were placed fixed on PdP pier for these tests. Tests after PdP campaign yielded determination coefficients (ρ^2) and (straight-line fits) equal to 0.9960 ($y = 1.0065\,x + 0.0069\ [m/s]$) and 0.9990 ($y = 1.0094\,x + 0.0011\ [m/s]$) for 1-s and 10-min data, respectively. Likewise, RMSE were as low as 0.93% (1-s tests) and 0.04% (10-min tests). When the SV was intercompared (figure not shown), determination coefficient and straight-line fit were 0.9426 and $y = 0.9663\,x + 0.0004$ for

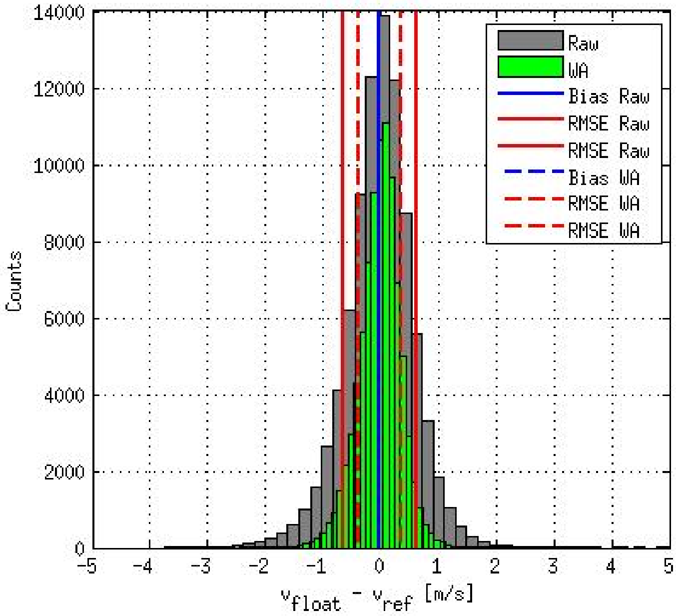

Figure 4.10: Window averaging algorithm histogram of raw and window-averaged 1-s HWS data.

1-s data, and 0.9953 and $y = 0.9759\,x + 0.0003$ for 10-min data (intercomparison test before PdP campaign, virtually identical indicators after the campaign). Excellent agreement in the results above shows that the "floating" lidar remained calibrated during the entire measurement campaign.

4.4.2 On the impact of angular motion and SV on the retrieved HWS

In order to characterise the HWS error behaviour of the floating lidar, two case studies of statistical significance are discussed:

- *Case 1* (Fig. 4.14) is representative of a high-angular-motion, low-SV scenario whereas
- *Case 2* (Fig. 4.15) is representative of a low-angular-motion, high-SV scenario.

At this point, is hypothesized that "low/high SV" accounts for SV primarily affected by patterns of the atmospheric conditions (atmospheric-induced SV due to e.g., low/high wind turbulence) and not that much - or secondarily - by patterns introduced by the motion of the floating lidar (motion-induced SV). To support this, the SV measured by the "reference" lidar has been compared against the SV measured by the "floating" lidar over the whole 38-day campaign (10-min data, statistical sample of 3937 points) in scatter-plot form (figure not shown). This has yielded a virtually ideal 1:1 correlation ($y = 1.065\,x$) with narrow dispersion ($\rho^2 = 0.948$) hence, showing that -because both lidars virtually measure the same SV- angular motion of the buoy has little effect on the lidar-observed SV. The physical explanation behind this result lies on the quasi-static behaviour of the buoy as compared to the conical scanning period of the lidar. Because typical oscillatory periods of the floating lidar buoy (3 to 5 s) are comparatively larger than the 1-s conical scanning

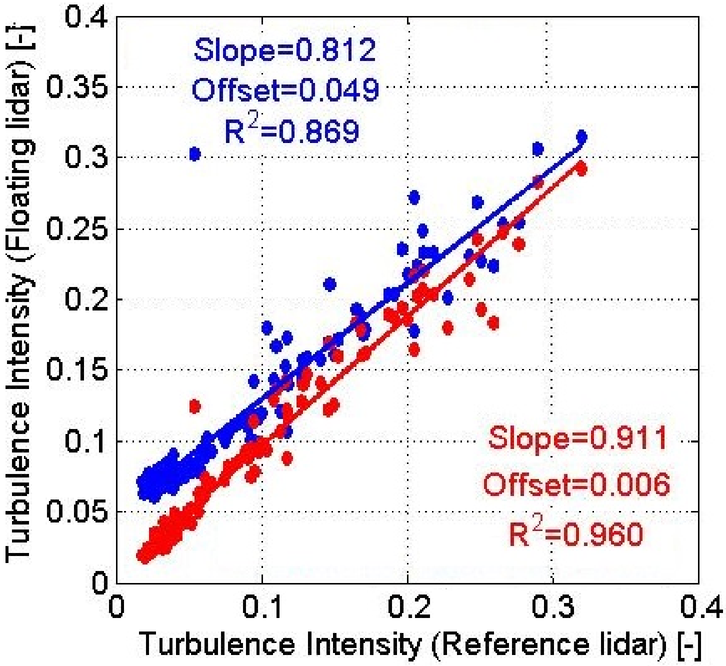

Figure 4.11: TI calculated with raw data (blue dots) and window-averaged data (red dots).

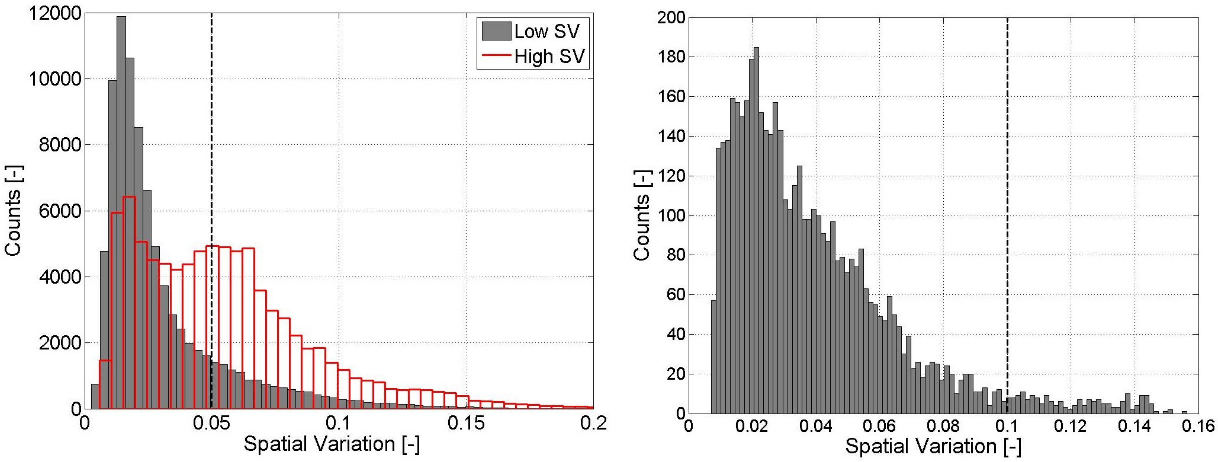

Figure 4.12: SV histograms. (a) Histogram of the SV distribution for two case examples (low- and high-SV scenarios) using 1-s data. (b) 10-min SV for the whole PdP campaign. (Both panels) dashed black lines indicate the screening threshold used.

period and angular amplitudes are usually lower than 15 deg, the floating lidar behaves as if it were apparently static for most of the scanning period.

Case 1 corresponds to a day (June 18th, 2013) with ENE (East-North East) wind (i.e., sea-to-land wind, see Fig. 4.1a), 8.0 m/s mean speed ("fresh breeze" in Beaufort scale) at 100 m in height while case 2 corresponds to a day (May 31th, 2013) with WNW (West-North-West) wind, 3.0 m/s mean speed ("light breeze") at 100 m in height. The "low motion" scenario is defined by a characteristic wave height between 0.1-0.5 m and $\approx$ 4 deg maximum angular amplitude while the "high motion" scenario is defined by a wave height between 0.5-1 m and $\approx$ 15 deg maximum angular amplitude. In both cases, Figs. 4.14-4.15 show the absolute error (magnitude of the difference

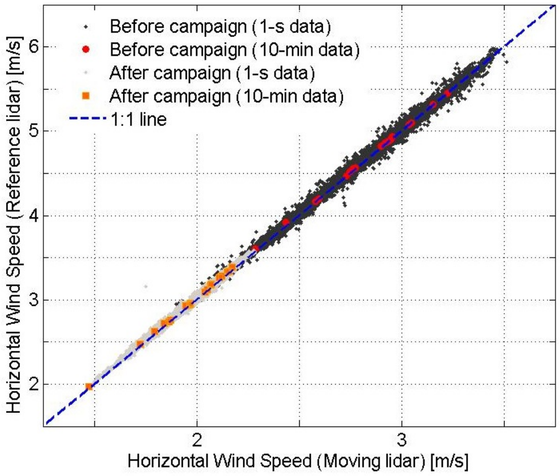

Figure 4.13: Example of HWS intercomparison tests before (02/05/2013 from 09:00UTC to 12:00UTC) and after (26/07/2013 from 09:30 to 12:30) PdP campaign using 1-s and 10-min data. Black and grey dots correspond to 1-s data before and after the campaign, respectively. Red and orange squares correspond to 10-min data.

between the value of a quantity measured by the floating lidar and its actual value given by the reference lidar) in the retrieved 1-s HWS as a function of the angular amplitude (Figs. 4.14a, 4.15a) and SV (Figs. 4.14b, 4.15b). Specifically, in Fig. 4.14 and 4.15, pitch (α) and roll (β) are calculated by averaging 10-Hz measurement every 1-s, while in Fig. 4.6b and 4.17 hourly and daily values are obtained by averaging the 10-min RMS values from 10-Hz measurements. Errorbars depict the approximate 1σ dispersion of the mean HWS error (Y-axis) and have been computed from the standard deviation in the retrieved mean absolute errors. Angular amplitudes have been grouped into 0.5-deg bins and SV into 0.01 bins when computing daily histograms for these two days.

Figs. 4.14a and 4.15a show that the HWS error can be bounded below 0.5 m/s when the motion amplitude is below 5 deg. This value is in agreement to previously published results (*M. Pitter et al.*, 2014) for low-to-mid wind speed (3-15 m/s). From a physical point of view, errors arise as a consequence of the inhomogeneous ensemble of turbulent- and motion-induced wind velocities (random variables) in the probe volume of the lidar. According to the central limit theorem stating that the probability density function (p.d.f.) of a myriad of independent random variables (no matter which their original distribution is) tends be Gaussian, one can assume errorbars do follow a Gaussian p.d.f. (*Barlow*, 1989), which gives maximum likelihood of occurrence at the center of the errorbar (solid dots in Fig. 4.14 and 4.15). Under this assumption, when comparing Fig. 4.14a with Fig. 4.14b for case 1, it arises that when the angular amplitude is larger than approximately 5 deg the main contribution to the mean HWS error (tendency line shown in dashed black trace) comes from the lidar angular motion and not from the SV. This is also shown in Fig. 4.14b by HWS errors remaining bounded to approximately some 0.5 m/s for the whole SV range of the day, SV = 0-0.25. In contrast, in the low-motion scenario of case 2 (angular motion below 3.5 deg for the whole day, HWS error $<$ 0.4 m/s, Fig. 4.15a), the SV is the main error source (HWS error $>$ 0.4 m/s for SV $>$ 0.05, Fig. 4.15b), which accounts for the turbulent behaviour of the wind flow that day.

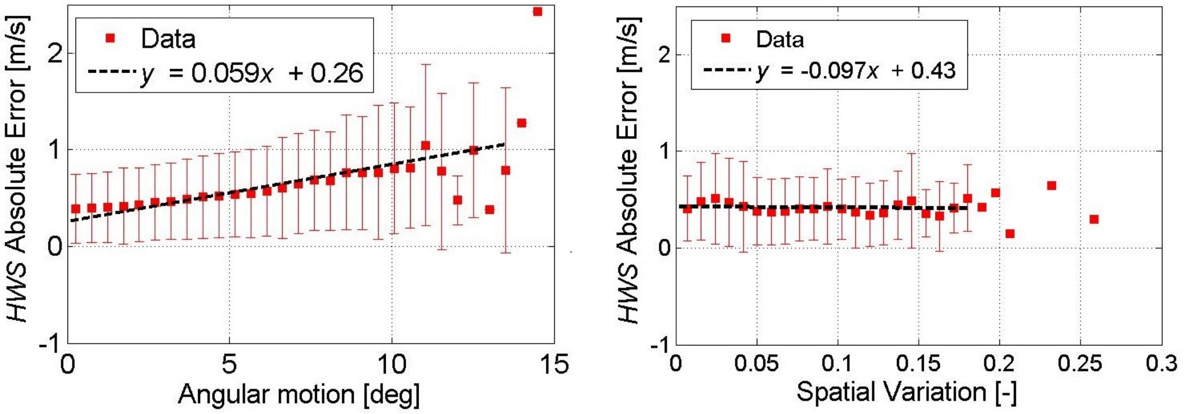

Figure 4.14: *Case 1*: High-angular-motion, low-SV case (June 18, 2013, 00:00-23:59 UTC). Behaviour of the mean 1-s HWS absolute error as a function of (a) angular motion amplitude (1 bin = 0.5 deg) and (b) SV (1 bin = 0.01 SV [a.u.]).

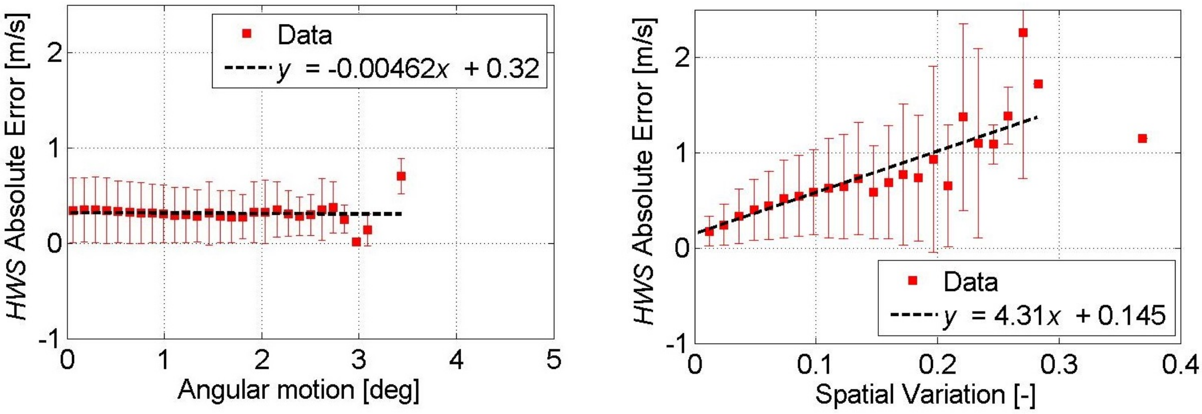

Figure 4.15: *Case 2*: Low-angular-motion, high-SV case (May 31, 2013, 00:00-23:59 UTC). (a-b) Same as Fig. 4.14.

4.4.3 Wind spectrum analysis and motion compensation

Central to study the impact of sea-induced motion on the measured HWS and related performance of the motion-compensation algorithm (Sect. 4.3.2) is analysis of the HWS from a spectral perspective.

One-day-long 1-s HWS time series with an availability higher than 90% has been used to estimate the Power Spectral Density (PSD) for both the reference and the floating lidar under the two different motion scenarios presented above: "low motion" and "high motion". Three PSD estimators have been considered and intercompared: the periodogram, Welch's method and Burg's method (*Proakis and Manolakis*, 2006) yet, in what follows, and because Burg's method yields exactly the same spectral estimates as Welch's but with a lower variance, all PSDs shown next are computed using Burg's. By experiment a filter order of M = 1800 has been used in Brug's (this parameter being equivalent to using 6-h data segments, M' = 21600 samples in Welch's (*Canadillas et al.*, 2010).

Fig. 4.16 shows the lidar-measured wind spectrum under low- (Fig. 4.16a) and high-motion (Fig. 4.16b) scenarios for (i) the reference lidar, (ii) the floating lidar, and (iii) the floating lidar after application of the motion-corrrection algorithm of Sect. 4.3.2. An asymptotic straight line has been fitted to the reference-lidar spectrum giving a fitting slope of -1.8, which is very close to the -5/3 theoretical slope - or "true" wind spectrum - (≈ 8% error) of Kolmogorov's spectrum function in the inertial range (*Frisch*, 1995). Important is also to notice the slight signal increase above the fitted asymptote or "true" wind spectrum in the frequency range between approximately $3\ 10^{-3}$ and $5\ 10^{-1}$ Hz observed by the floating lidar (this is better seen in the "low-motion" scenario of Fig. 4.16a). This is also in agreement with similar results in the state of the art (*Canadillas et al.*, 2010).

When addressing the "high-motion" scenario of Fig. 4.16b, sea motion induces a strong increase in the spectral content from $2\ 10^{-3}$ to $5\ 10^{-1} Hz$ (end of the frequency range) of some 10 dB at $f = 10^{-2} Hz$ and more that 15 dB at $f = 5\ 10^{-1}\ Hz$ (blue trace). After applying the motion compensation algorithm of Sect. 4.3.2, the PSD of the floating lidar virtually coincides with that of the reference lidar, hence verifying the goodness of the proposed algorithm. The correction algorithm has been applied by recomputing the length of the adaptive tapering window every 10-min for the whole 24-h time series. Similar satisfactory results are obtained for the "low-motion" scenario, though with the added difficulty of having much lower spectral levels to correct.

4.4.4 PdP campaign statistical results

Fig. 4.17 summarises the 38-day campaign statistics on a daily basis using three different "filtering" stages from Sect. 4.3.2: (i) no filtering at all (red trace), (ii) motion compensation by window averaging (green trace), and (iii) window averaging plus SV filtering (blue trace). External conditions regarding the angular-motion parameter and the atmospheric-induced SV (Sect. 4.4.2) are also plotted as time series. For reference, the SV can be related to the lidar-observed TI via Fig. 4.6a and the angular motion can be related to the wave height via Fig. 4.6b. The adaptive window length of the motion-compensation algorithm has been computed by composing the 1-s time series for each day (86400 measurement samples) and by Fourier estimation of the buoy angular dominant

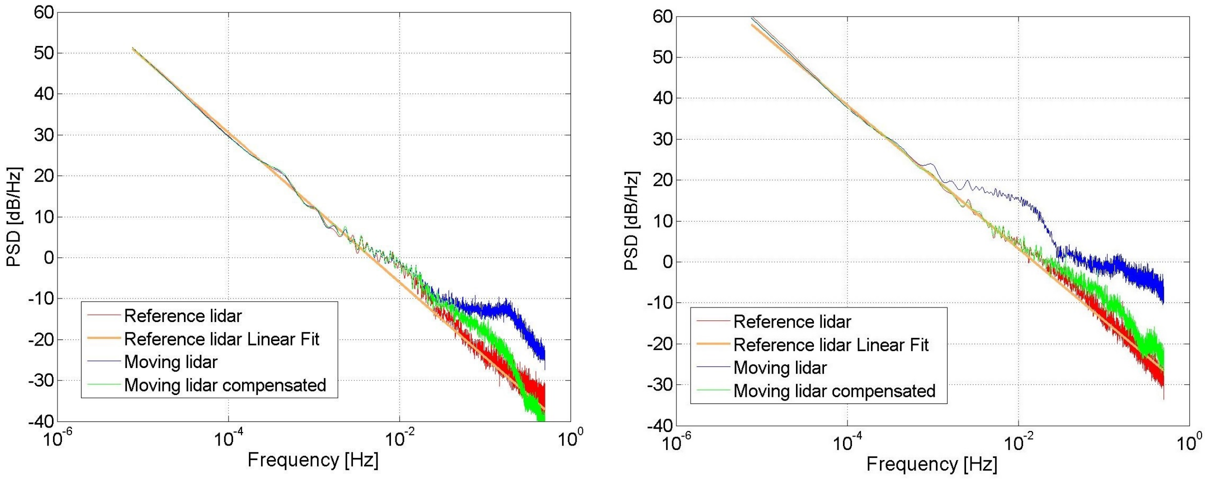

Figure 4.16: PSD of the lidar-measured HWS under low- and high-motion scenarios. (a) High-motion case showing wind spectra for the reference lidar (red), the floating lidar (blue), and the floating lidar after application of the motion-correction algorithm (green). (b) Low-motion case (same legend). The PSD is computed in units of $[(m/s)^2/Hz]$ and represented in decibels/Hz, $PSD\ [dB/Hz] = 10log_{10}\{PSD[(m/s)^2/Hz]\}$.

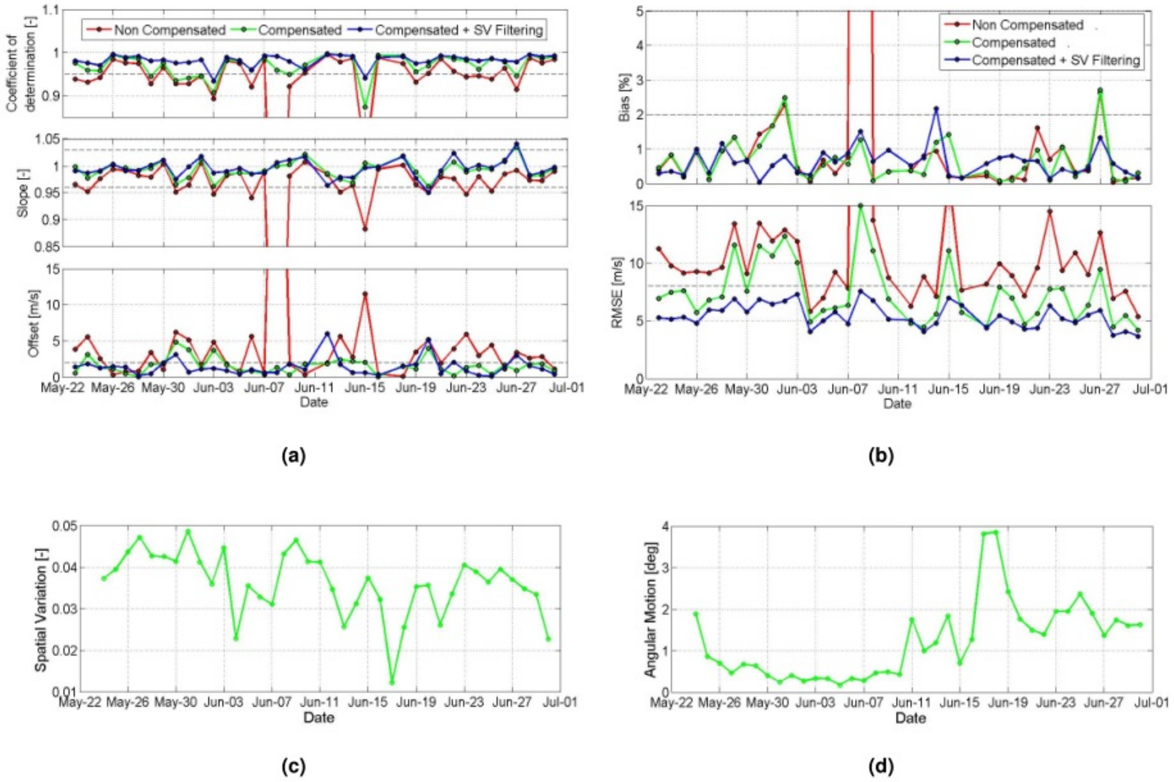

Figure 4.17: Performance statistics of 38-day PdP campaign using 1-s HWS data evaluated on a daily basis. (a) Linear fit regression indicators: coefficient of determination, ρ^2, slope, m, offset term, n. (b) Time-series statistical indicators: Bias, RMSE. Traces (all panels): (Horizontal dashed black) 1-s KPIs according to the range intervals given in Tab. 2.3. (Red) No filtering method applied. (Green) Window averaging (Sect. 4.3.2). (Blue) Window averaging and SV filtering (Sect. 4.3.2). Each colored dot represents a measurement day with aggregated statistics. (c) Time-series external conditions: atmospheric-induced SV and (d) Angular motion (Sect. 4.4.2). Note that all blue dots fulfil Tab. 2.3 KPI standards, i.e., they lie above the horizontal dashed black trace ((a), top panel), below it ((a), bottom panel; (b), both panels) or within dashed black traces ((a), middle panel).

period (peak level of the angular power spectrum distribution) every 10 minutes along the daily time series. The SV threshold (above which measurement samples are treated as outliers) has been set to SV $>$ 0.05 when computing daily histograms (38 histograms). This SV criterion yields a 30% mean rejection ratio over the 38-day measurement period for 1-s data. Though different SV thresholds can be set, there is always a trade-off between threshold level and data availability (i.e., the amount of “clean” data available for the end user after removing outliers). The mean rejection ratio can change depending on the wind field conditions of a specific measurement site. At complex terrain sites (i.e. highly turbulent environments) the rejection ratio is expected to be higher while at flat terrain sites (i.e. low turbulent environments) will be lower.

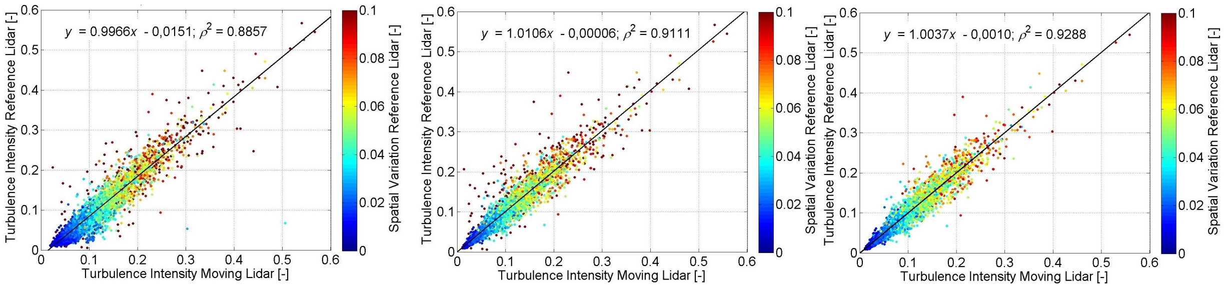

(a) (b) (c)

Figure 4.18: TI scatter plots for the whole campaign using 10-min data evaluated on for the whole campaign (May 23th, 00:00UTC, June 30th, 23:59UTC). (a) No filtering method applied (Red in Fig. 4.17). (b) After window averaging (Green in Fig. 4.17). (c) After window averaging and SV filtering (Blue in Fig. 4.17). (All plots) The colorbar codes SV.

Tab. 4.1 summarizes 1-s and 10-min KPI PdP-campaign error indicators for the three filtering stages considered ((i)-(iii) above) and in regard to HWS and TI variables. Statistics are representative of the whole PdP campaign and have been computed by using the composite 38-day time series. HWS case (ii) is skipped for 10-min data in Tab. 4.1 because typical FFT-window lengths for motion averaging are about 3 s, a much lower figure than 10-min. In brief, when 1-s data in Fig. 4.17 is cross-examined against Tab. 2.3, it emerges that the window-averaging technique (case (ii) above) yields substantial improvement for most of the days, thus, raising the default 30% 1-s KPI compliance when no filtering procedure is applied (case (i)) to 80% compliance. In spite of the huge improvement given by the window-averaging technique, only after subsequent SV filtering (case (iii)) is achieved that all days fulfill virtually all KPI requirements (98% compliance). When window averaging is used for motion compensation, the largest improvement in the error indicators of Tab. 4.1 occurs for the slope, which tends to the 1.000 ideal value (from 0.953 in case (i) to 0.993 in case (ii), 1-s data). The statistical indicator that behaves worse is the RMSE (from 12.24% in case (i) to 7.39% in case (ii), 1-s data).

These results warrant, however, some comments: Thus, day-by-day inspection of Fig. 4.17 reveals that in many days application of the motion-compensation algorithm is enough to ensure compliance of the 1-s KPIs of Tab. 2.3 (KPI’s shown in horizontal dashed trace) and which outlines that deviations are mainly an effect of motion rather than of different atmospheric situations (mainly, turbulence). This is shown by a green trace (motion-compensated data) moving far apart from the orange trace (“no filtering at all”) and virtually overlapping with the blue trace (motion

Table 4.1: 1-s and 10-min error-assessment indicators for the whole PdP campaign.

	ρ^2	**slope**	**Offset**	**bias**	**RMSE**
1-s data					
HWS (case i)	0.926	0.953	4.69%	2.34%	12.24%
HWS (case ii)	0.969	0.993	1.56%	0.68%	7.39%
HWS (case iii)	0.981	0.995	1.38%	0.62%	5.44%
10-min data					
HWS (case i)	0.996	1.005	0.10%	0.29%	3.43%
HWS (case iii)	0.996	1.005	0.10%	0.29%	3.43%
TI (case i)	0.886	0.997	15.75%	15.50%	23.60%
TI (case ii)	0.911	1.010	0.62%	0.50%	20.84%
TI (case iii)	0.929	1.000	0.65%	0.68%	18.03%

compensation + SV filtering). Consider, for example, "coefficient of determination" in the top panel of Fig. 4.17a and refer to e.g., May, 24-25; Jun, 8-9; Jun. 19-23, 25-26, 28-30. On other days, SV filtering is the main responsible for ensuring KPI compliance, hence showing that the deviations are mainly an effect of the atmospheric situation. This is identified by virtually overlapping red and green traces and a blue trace moving far apart from them (in the same example above refer to e.g., May 29, 31; June 1-2, 24). On a few days, however, the dominant mechanism (angular motion or turbulence) is not so evident and deviations from KPI acceptance levels may well come from a combined effect of both (e.g., Jun. 15, 23 and 27).

A clear improvement in all statistical indicators is therefore observed, hence showing that the proposed methodology (that is, motion compensation by window averaging and SV filtering) is a suitable tool to improve the reliability of the data gathered by the floating lidar (98% compliance) while ensuring 70% data availability for the 1-s data and 95% data availability for the 10-min data (100% compliance).

4.4.5 Turbulence intensity

As outlined in Sect. 4.1, atmospheric turbulence can have negative effects on power performance and reduce wind-turbine average lifetime. Therefore, reliable measurement of the TI becomes crucial for the wind industry. Differences between "real" (i.e., point-like measured) and "lidar-observed" TI (Sects. 4.3.1 and 4.4.3) can be problematic even for fixed lidar systems, not to mention for a moving lidar. Accepting these limitations for fixed lidars, in this subsection is show how successive application of the window-averaging and SV-filtering methods so far discussed aids to improve the reliability of the 10-min estimated TI by the floating lidar to a level *close* to that of the fixed lidar. First, 1-s data processing is forcibly used to enable application of the motion-compensation algorithm (Fig. 4.9a). Second, the output of this algorithm is recomposed into a 10-min time series from which a SV filter is applied and 10-min TI estimated (industry standard). Here, note that buoy motional periods typically range from three to a few seconds, which is a time scale according 1-s raw processing. Both lidars were well calibrated and located close enough so as to sense the same wind distribution and neglect instrumental errors (Sect. 4.4.1).

Fig. 4.18 shows TI scatter plots in response to the same signal processing cases discussed in the preceding subsection (cases (i), (ii) and (iii), in Sect. 4.4.4). To compute the scatter plots of Fig. 4.18 the 38-day campaign HWS data has been composed and synchronized (Sect. 4.3.1) into two 10-*min* time series (nominally, 5472 samples), one for the reference lidar and another for the floating lidar. The TI has been computed accordingly and TI scatter plots have been color coded for the SV value.

To begin with the analysis, Fig. 4.18a shows the 10-min TI scatter plot and pertinent regression analysis when no filtering is applied (case (i)). As expected in this case, a comparatively poor correlation between the "reference"- and the "floating"-lidar TIs is found showing a comparatively poor determination coefficient ($\rho^2 = 0.885$) and a large offset term (slope, $m = 0.997$; offset, $n = -0.015$). The large offset is related to an overestimated TI caused by high-frequency motion-induced HWS fluctuations in the floating lidar. When addressing Fig. 4.18b (case (ii), window averaging) the determination coefficient and the offset terms are significantly enhanced ($\rho^2 = 0.911$, slope, $m = 1.011$; offset, $n = -6\ 10^{-4}$) but still several outliers broad the scatter plot. In more detail, and by using that each point is colored with its corresponding SV magnitude (refer to SV colorbar), is noticed that most of these outliers correspond to high SV values ($SV > 0.1$). This $SV > 0.1$ relation translates into a 5% population when the 10-min histogram for the whole campaign is analysed.

Finally, Fig. 4.18c (case (iii), window averaging and SV filtering) shows one further improvement in the statistical indicators ($\rho^2 = 0.930$, slope, $m = 1.004$; offset, $n = -1\ 10^{-4}$) and a most relevant effect being the removal of the comparatively small population of SV outliers (5%) responsible for such high SV values ($SV > 0.1$). In summary, from case (i), i.e no filtering, to case (iii) the overall improvement in the statistical parameters goes from 0.996 to 1.003 in the slope; -0.0151 to -0.001 in the offset, and 0.885 to 0.930 in the determination coefficient. Overall, the latter represents a 5% enhancement factor in the TI determination coefficient (this figure can be taken as the percentage improvement achieved when estimating the TI from the floating lidar) while ensuring 95% data availability.

4.5 Conclusions

HWS and TI measurements at 100 m in height from a buoy Doppler lidar during a 38-day nearshore campaign at PdP (Badalona, Barcelona) have been revisited from a signal-processing methodology and statistical error-analysis perspective. This work has shown that *linear-fit indicators*, namely, slope, offset term and determination coefficient, and *time-series indicators*, namely, bias and RMSE, are useful error indicators to cross-examining "floating"- versus "reference"-lidar measurement datasets. 1-s time series analysis has enabled closer inspection of the HWS error beh, thus relating this error against angular motion amplitude of the floating lidar.

Study cases 1 and 2 (Sect. 4.4.2, Figs. 4.14 and 4.15) have corroborated angular motion and lidar-observed wind turbulence (parameterized by the SV) as the main error sources affecting the floating lidar KPIs. At methodological level, daily HWS error histograms have been computed as a function of the floating-lidar angular-motion amplitude and SV. Though this histogram classification of the HWS error does not inherently guarantee perfect separation between error sources (i.e., the HWS error associated to a given angular-motion amplitude is always inherently measured under some level of SV) it has served to the purpose to identify these two dominant error sources, their beh, and in relation to the filtering methods presented.

Two filtering methods, adaptive window averaging and SV filtering have been proposed at post-processing level:

- The *window-averaging technique* is implemented as a boxcar filter with an adaptive time window equal to the mean motion period (i.e., the inverse of angular-velocity spectrum peak frequency) recomputed on a 10-min basis. This technique has proven effective enough to minimize the impact of wave-induced angular motion on the floating lidar performance by yielding an overall improvement in all statistical indicators towards KPI compliance (Tab. 4.1). Specifically, the default 30% 1-s KPI compliance when no filtering procedure is applied (case (i)) is raised to some 80% compliance when window averaging is applied (case (ii)). Likewise, when considering HWS results for the whole campaign (Sect. 4.4.4), the width of the 1-s HWS error histogram (*Gutiérrez et al.*, 2015) is reduced from $\mathrm{RMSE_i} = 0.51$ m/s (12.24%, Tab. 4.1) to $\mathrm{RMSE_{ii}} = 0.34$ m/s (7.39%, Tab. 4.1). When considering TI (10-min data, Sect. 4.4.4), the offset between the "reference" and the "floating" lidar is reduced from $n_\mathrm{i} = -0.0157$ to $n_\mathrm{ii} = -6\ 10^{-4}$.

- *SV filtering*, which is implemented as the SV threshold above which measurements are treated as outliers, represents a trade-off between KPI improvement and data availability. When both window averaging and SV filtering procedures are applied (case (iii)) 98% KPI compliance is achieved (70% 1-s data availability, $SV > 0.05$ threshold, Tab. 4.1). Concerning TI (10-min data, Sect. 4.4.4) a further a 5% enhancement factor in the TI determination coefficient is obtained (95% data availability).

All in all, this work has enabled a wealth of signal processing and statistical methods to better understand the error behaviour of a ZephIR 300 floating Doppler wind lidar and ways to minimise these errors at post-processing level in relation to KPI compliance.

Chapter 5

A wind-lidar buoy for offshore wind measurements: first commissioning test-phase results

This Chapter addresses IJmuiden's measurement campaign to validate lidar buoy EOLOS developed in the framework of project NEPTUNE. Main characteristics of EOLOS and related signal processing methodologies developed to ensure trustworthy data retrievals are discussed.

The contents of this Chapter are part of the peer-review conference paper, *Gutierrez-Antunano et al.* (2017), "A wind-lidar buoy for offshore wind measurements: First commissioning test-phase results", 2017 IEEE International Geoscience and Remote Sensing Symposium (IGARSS), Fort Worth, TX, 2017, pp. 1607-1610. doi: 10.1109/IGARSS.2017.8127280.

5.1 Introduction

In 2012, KIC InnoEnergy (*Schuon et al.*, 2012) started project NEPTUNE. One of the objectives of the project was development of a floating lidar buoy. At the end of the project (December 2014), a lidar buoy (EOLOS FLS200) was ready to be validated in real offshore conditions and the OWA gave the possibility of a pilot validation trial at IJmuiden's test facilities (North Sea) against an offshore metmast.

The aim of this chapter is two-fold:

On one hand, the chapter is to present the EOLOS FLS200 buoy and the first phase of the pilot validation trial (March, 17, to June, 6, 2015). This includes and outline of the signal processing procedures developed to yield trustworthy lidar data, namely, solution of the ambiguous retrieval of the WD, and outlier data filtering.

On the other hand, wind measurements (HWS and WD), between the lidar buoy developed and metmast will be compared at IJmuiden test facility.

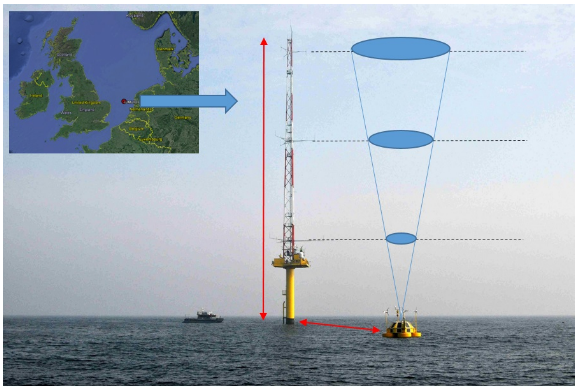

Figure 5.1: Validation campaign location and image of the IJmuiden test site (North Sea).

5.2 Measurement Campaign IJmuiden

As described in (*Gutierrez-Antunano et al.*, 2017), a validation campaign of the floating lidar was performed at the IJmuiden test site (*Werkhoven and Verhoef*, 2012; *Poveda et al.*, 2015), in the Netherlands. The aim of this campaign was to assess the accuracy of the EOLOS lidar buoy against metmast IJmuiden (*Carbon Trust*, 2013). The main instruments used were: (i) a moving ZephIR™300 lidar in the EOLOS buoy; (ii) a reference ZephIR™300 lidar placed on the metmast platform and measuring at 90, 115, 140, 165, 190, 215, 240, 265, 290, and 315 m above Lowest Astronomical Tide (LAT), both measuring sequentially at each height; and (iii) sonic anemometers at 27, 58, and 85 m above LAT. Additionally, data from IMUs were used to characterize the motion of the lidar buoy. This campaign took place between March and October 2015, but present work uses first phase of this cmampaign: from black 1 April to 1 June 2015.

5.2.1 IJmuiden test site

IJmuiden is a port city located in the mouth of the IJ, in the province of North Holland, in the Netherlands. The IJmuiden metmast, owned by RWE company and operated and maintained by Energy research Centre of the Netherlands (ECN), is located 85 km off-coast of the Netherlands (Fig. 5.1). The sea-depth at the test-site facility is around 28 m.

IJmuiden test facility is equipped with a 92-m tall metmast, which houses different sensors to gather main relevant environmental magnitudes. This measurement set-up allows to monitor the HWS at four heights (27, 58, 85 and 92 m above the LAT). Additionally, the presence of sensors monitoring the pressure, temperature and humidity at the lower and higher levels allows to assess the atmospheric stability, an important parameter due to its influence in the performance of the Wind Turbine Generators (WTGs). A Triaxys wave buoy is also moored in the area to provide sea currents at different levels and wave measurements in the site. Further details of the metmast and the related equipment have been presented in (*Werkhoven and Verhoef*, 2012).

5.2.2 The EOLOS lidar buoy

Although not a commercial buoy during the IJmuiden validation trial, today, the *EOLOS FLS200* is a commercial floating lidar system owned by EOLOS Floating Lidar Solutions. Is a 3-t weight, 3.77-m width lidar buoy and its metmast reaches 3 m above the water line. Developed to optimally fit a ZephIR 300 Lidar, ensuring proper dynamics for wind measurements, and at the same time acting as a multipurpose buoy platform capable to satisfy wind energy requirements. It is energy autonomous and can host other measuring instruments. Therefore, it can collect and communicate a wide variety of wind and sea-related data.

Following Fig. 5.2, it consists of a purposely design modular four-floater structure designed to optimize dynamics of the wind measurements that allowing easy transportation of its elements prior to assembly. Once assembled they buoy ensures power generation capability, stability over various sea-states, and enough floating capacity to handle several mooring configurations.

The *main structure* of the buoy has been constructed with stainless steel and is covered by aluminum reinforced fiberglass to protect the electronic equipment inside, that also serves as support for solar power modules. The interior contains power regulation, data management and communication electronics, and the lidar fixation itself, in a grid platform about 1 m above the sea level.

Four masts arise from the four corner cylinders. One of them acts as the “stern” of the buoy, with a mounted tail so that the opposite corner, despite the buoy’s symmetrical shape, always faces the wind. In that ‘bow’ mast facing the wind, two redundant meteorological stations are placed and measure undisturbed wind parameters. The other three masts hold three wind generators, with the navigation aids placed at the top of the tail.

Data acquisition system is based in Campbell Scientific dataloggers that gather, store and send the information from the different sensors and equipments. The system allows periodic data download trough Iridium satellite and a Wi-Fi link up to about 100-m for operations requiring more robust communication link (*Sospedra et al.*, 2015). Security measures following IALA recommendations (*Bole*, 1991) include Inmarsat satellite drift alarms and radar reflectors.

One of the main challenges for an offshore autonomous system is the power generation. EOLOS buoy hold solar panels and wind generators for a total of 2.200 W nominal maximum power. The battery system, contained in the cylinders that hold the floaters, sum 1320 A-h including backup batteries reserved for essential safety and positioning operations. In case of a low-battery status this battery bank ensures 48h of communications and key measurements.

The selected lidar is the Natural Power ZephIR 300, a continuous-wave Doppler lidar able to profile 10-heights up to 200 m in height. The device was configured to focus at 27, 58 and 85 m above LAT to match the metmast measurement heights. EOLOS FLS200 is also equipped with two surface weather stations, a current profiler, a wave sensor, and one three-axis accelerometer that provides attitude data.

5.2.3 Operations and logistics

All EOLOS buoy elements were assembled and tested at LIM-UPC facilities in Barcelona (Spain), Dec. 2014 to Jan. 2015. Once tests were passed the buoy was moved to IJmuiden by special

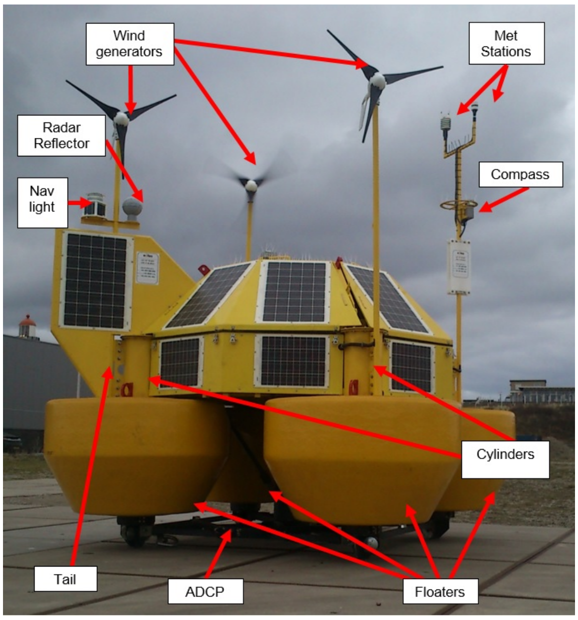

Figure 5.2: The EOLOS lidar buoy.

land transport. For a month the entire system, data acquisition, communications and energy, were tested in near real conditions.

Finally, on March 2015 the buoy was moved to its deployment position close to IJmuiden metmast by a tug.

Fig. 5.3 shows most relevant parameters of the waves during the first phase of the campaign. Fig. 5.3a shows the significant wave height measured by the buoy which reached more than 6 m in height. Fig. 5.3b shows the directionality of the waves, SW and N being the main directions of the waves.

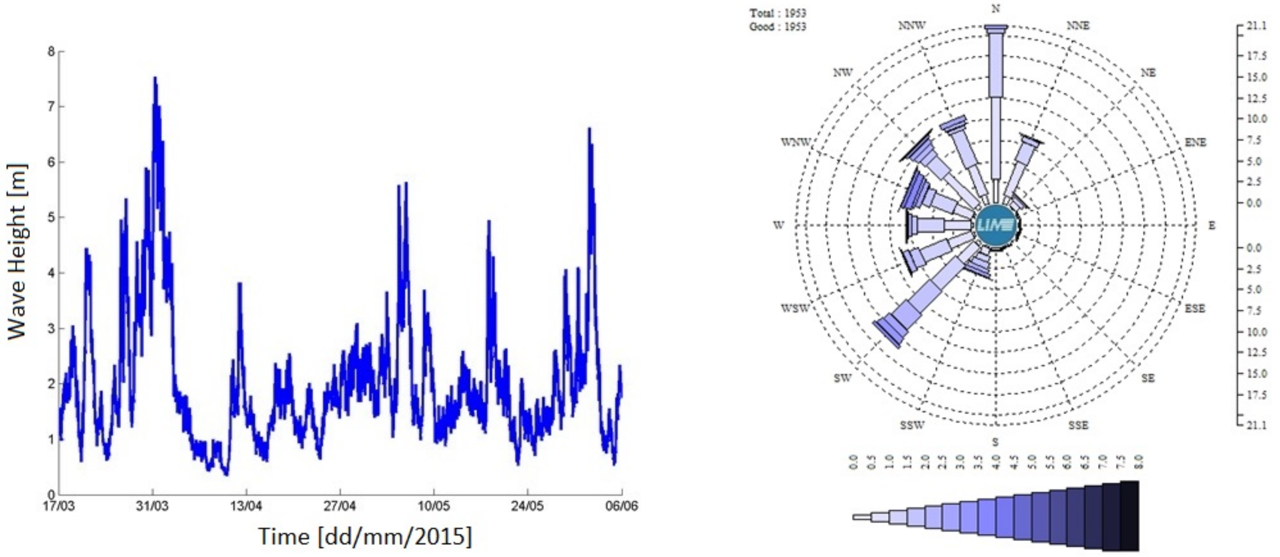

(a) (b)

Figure 5.3: Main wave parameters during the first phase of IJmuiden validation trial: (a) Significant Wave Height and (b) Wave Directionality (time resolution: 1-hour).

5.3 Methods

So far, the wind industry has provided state-of-the-art 10-min KPI. The KPIs became an essential "pass" requirement during the validation campaign at IJmuiden. Towards this end, signal-processing algorithms are aimed at ensuring appropriate data quality and necessary fulfillment of the KPIs. In absence of a official standard, (*Carbon Trust*, 2013) provides guidelines for the acceptance of lidars for offshore wind measurements.

Homodyne WD correction .- Main disadvantage of the ZephIR 300 lidar is its homodyne detection principle that produces an ±180 deg ambiguity in the calculation of the WD. This is to say that the lidar doesn't distinguish a wind coming from the South from one coming from the North (180-deg offset).

To solve this ambiguity, our algorithm uses as reference WD the non-ambiguous WD measured by a sonic anemometer at the buoy. Thus, the lowest WD measured by the lidar (27 m above LAT) is compared to the reference WD and if the difference is greater than certain threshold the lidar WD is offset by 180 deg. This procedure is repeated for each measurement height but using as reference the WD from the measurement height immediately below it.

To show the goodness of the method Fig. 5.4 shows the WD error histogram between the lidar and the reference metmast for the *corrected* and the *not-corrected* cases (log scale is used to highlight erroneous counts at ±180 deg). From this figure it becomes clear that correction of the homodyne ambiguity virtually removes all WD errors. The residual error in Fig. 5.4 after correction, |WD Error| ∈ (20 - 40) deg, is thought to be caused by "switched" and "non-switched" 1-s WD values coexisting in the 10-min measurement interval.

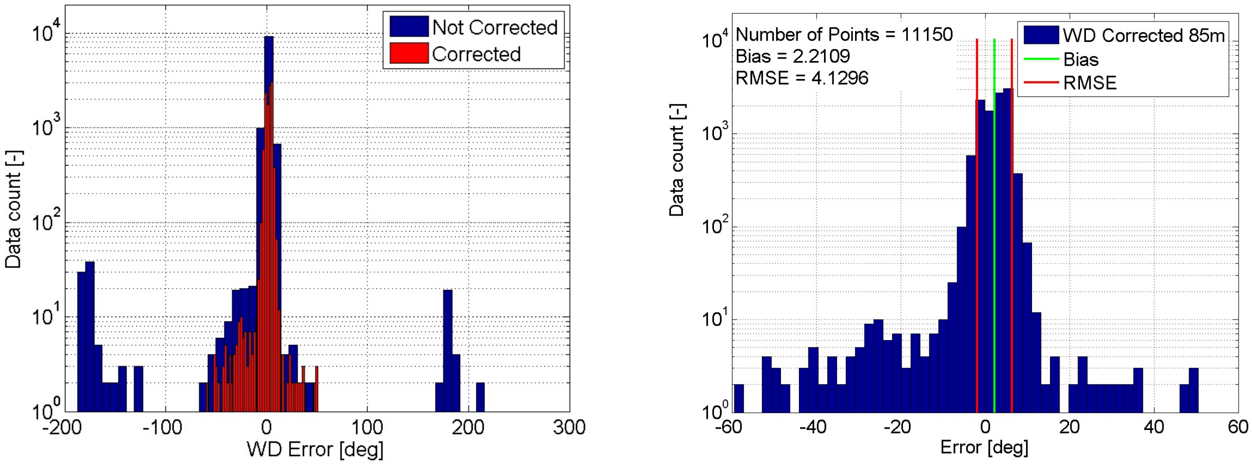

(a) (b)

Figure 5.4: WD error histogram. (a) Before and after application of the homodyme WD-correction algorithm. (b) Graphical representation of main statistical parameters: bias and RMSE.

Outlier data filtering .- Lidar measurement of the wind vector can be hampered by different reasons, including the buoy movement but also rain, fog or turbulence. Therefore, it is important to filter out untrustworthy data. A threshold filtering-algorithm has been developed and applied to key wind-measured variables, namely, HWS and WD, as well as internal lidar parameters in order

Table 5.1: Summary of KPI and achieved measurement results (*Carbon Trust*, 2013).

KPI	Parameter	Measured	Best Practice
HWS 85 m	Slope	1.00	0.98 - 1.02
	Determination Coef.	0.99	> 0.98
WD 85 m	Slope	1.01	0.97 - 1.03
	Offset	0.24 [deg]	< 5.00 [deg]
	Determination Coef.	1.00	> 0.97
Availability 85 m	System	100.00%	> 90.00%
	Post-processed	98.57%	> 85.00%

to qualify the measured datasets as valid data. Individual thresholds for each variable have been selected under a trial-and-error basis.

5.4 Discussion

The results of the measurement campaign (including signal-processing algorithms discussed) are summarized in Tab. 5.1, which describes the overall performance of the floating lidar versus the reference sonic anemometer in the metmast in term of the KPI requirements of (*Carbon Trust*, 2013). After the application of the methodology presented in Sect. 5.3 main KPI for HWS and WD reach virtually ideal values, well above Best Practice recommendations (*Carbon Trust*, 2013).

Fig. 5.5 plots the 10-min HWS time series measured at 85 for both the floating lidar and the metmast, after the application of the signal processing methodology shown in Sect. 5.3. In the figure the range of wind speeds is 2-25 m/s and the range of significant wave height is 1-7 m (See Fig. 5.3a).

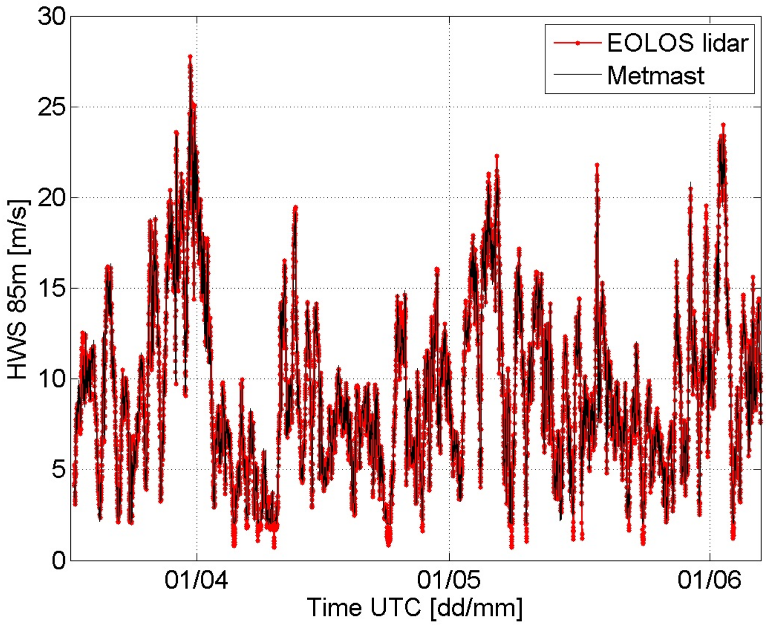

Figure 5.5: Temporal series of the 10-min HWS at 85-m height for the EOLOS lidar buoy and the reference metmast.

KPIs for Fig. 5.5 are embedded in Fig. 5.6.

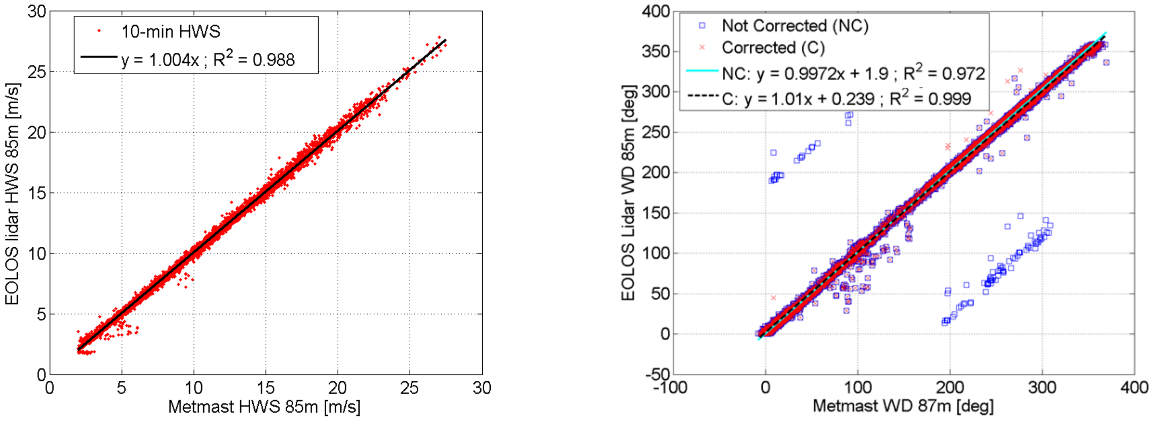

(a)

(b)

Figure 5.6: Scatter plot of the 10-min (a) HWS and (b) WD between the metmast and the EOLOS buoy at 85-m in height. WD is shown with and without the homodyne behaviour correction.

Fig. 5.6a shows the scatter plot between the HWS measured by the lidar and the HWS measured by the metmast (reference value). Both, the determination coefficient ($\rho^2 = 0.988$) and the slope of the tendency line ($m = 1.004$) show fulfillment of the KPI requirements.

To evidence the goodness of the WD-correction algorithm, Fig. 5.6b shows a scatter plot between the higher level WD measured by the metmast (reference) and the lidar for the cases "non-corrected" and "corrected" WD. While the "non-corrected" determination coefficient ($\rho^2 = 0.972$) is about to fail off the "Best Practice" interval of Tab 5.1, the "corrected" determination coefficient ($\rho = 0.999$) is close to the ideality, hence justifying the solution provided by the WD-correction algorithm.

Last but not least, data availability is another of the critical parameters when considering the use of a floating lidar. During the study period, the *system availability*, defined as the the ratio between the time that the system is ready to deliver the data and the total period, was of 100%. The *post-processed data availability*, defined as the ratio between the number of datasets remaining after filtering any internal or post-processing quality filters and the maximum datasets, reached 98.57% at 85 m.

5.5 Conclusions

This chapter has presented the development of an offshore buoy-based lidar (EOLOS FLS200) apt for assessing the suitability of candidate locations for a wind farm.

Main characteristics of the buoy have been presented as well as the first phase of the pilot validation trial at IJmuiden metmast that was performed to assess its commercial viability. The proposed methodology for data processing comprises: (i) a homodyne WD correction algorithm and (ii) an outlier data filtering procedure based on thresholding, all of which has proven effective enough to correct lidar data while fulfilling the KPIs selected by the wind industry to assess the suitability of a floating lidar device ($\rho^2_{HWS} = 0.988$ and $\rho^2_{WD} = 0.999$).

The comparative results shown between the lidar buoy developed and metmast measurements fulfill all requirements stated by the OWA (*Carbon Trust*, 2013) for commercial acceptance of floating lidar systems, and therefore the developed EOLOS buoy proves its capabilities as a useful device for the wind resource assessment of a candidate offshore wind farm location.

Chapter 6

Estimation of the motion-induced horizontal-wind-speed standard deviation in an offshore Doppler lidar

The contents of this chapter are two fold: On one side, the foundations of the Vertical Azimuth Display offshore motion simulator conceived at CommSenslab – DONLL are presented. On the other side, the mathematical bases of a new –to our knowledge- motional statistical methodology to estimate the motion-induced standard deviation and related TI on the retrieved HWS are formulated. Both approaches are rooted to the case of a conically-scanning lidar (the ZephIR lidar), where the wind speed vector is retrieved from the Line of Sight velocities over one scan period.

The motion-induced error is estimated from the simulator's side by using basic motional parameters, namely, roll/pitch angular amplitude and period of the floating lidar buoy, as well as reference wind speed and direction measurements at the study height. The impact of buoy motion on the retrieved wind speed and related standard deviation is compared against either simulated motional records or the reference sonic anemometer and reference fixed lidar over a 60-day period during IJmuiden's measurement campaign.

The contents of this Chapter are a combination of the journal paper, *Gutiérrez-Antuñano et al.* (2018) (available at MDPI website `https://www.mdpi.com/2072-4292/10/12/2037`, Open Access) and peer-review conference paper, *Tiana-Alsina et al.* (2017), 2017 (available at the IEEE Xplore website `https://ieeexplore.ieee.org/document/8127282`). Systematic or multiple reproduction or distribution to multiple locations via electronic or other means is prohibited and is subject to penalties under law.

6.1 Introduction

Floating lidar buoys suffer from translational and rotational motion, which has to be understood in order to find an appropriate methodology to compensate the errors induced on wind measurements.

On one hand, *translational motion* (sway, surge and heave, along the X, Y and Z axes, respectively) can be easily compensated by subtracting the motion vector from the measured wind vector, which justifies that translation motion in the horizontal plane is not studied in this work.

On the other hand, *rotational motion* is studied elsewhere (roll, pitch and yaw, around the X, Y and Z axes, respectively) is more difficult to be canceled out. Thus, buoy tilting has a strong impact on the LoS measurements of the lidar, which can induce a non-negligible bias on the measured wind vector (*Gottschall et al.*, 2012a; *M. Pitter et al.*, 2014) and which justifies the need for further insight.

In the present work, and with the aim of analysing and deconvolving the effect of lidar motion on the radial velocity measured along each LoS a *VAD simulator* is developed. Towards this end, the simulator uses given attitude data (pitch and roll information). The simulator is capable to reproduce different motion conditions and compute the corresponding LoS velocity measurements. The VAD simulator will help us to better understand the effect of the motion over the quality of the measured floating lidar data and therefore envisage postprocessing improvements to gather non perturbated lidar data.

Turbulence intensity (TI), which is defined as the ratio between the standard deviation of the HWS to the mean HWS, has a critical impact on wind turbine production, loads and design. The IEC61400-1 Normal Turbulence Model describes the TI threshold a wind turbine is designed for, and defines the wind turbine class of the machine that describes the external conditions that must be considered (*International Electrotechnical Commission*, 2005; *Manwell et al.*, 2009; *Hansen et al.*, 2012).

The *lidar-observed TI* is not identical to the "true" TI that can be measured by point-like measurements from cup anemometers. The lidar-observed TI is affected by the spatial (i.e., probe length) and temporal averaging (i.e., scanning time) of the Doppler lidar instrument and by the motion effects of sea waves on the lidar buoy. While spatial/temporal averaging effects on the measured TI can be found elsewhere (*Sathe et al.*, 2011; *Sathe*, 2012; *Sathe et al.*, 2015; *Wagner et al.*, 2009), here the aim is to *study the effects of lidar motion on the measured TI and their statistical correction.*

To simplify the mathematical framework to be presented next, the motion-corrected HWS standard deviation is numerically assessed under simple harmonic motion conditions of the lidar buoy for a given HWS and WD. Towards this end, a software motion simulator is considered to emulate the motion of sea waves under these simplified motion conditions and the VAD algorithm (*Fujii and Fukuchi*, 2005) to retrieve the motion-corrupted HWS. Furthermore, simulation results are validated against experimental results as part of the IJmuiden test campaign.

6.2 Velocity Azimuth Display Simulator For Doppler Wind-Lidar Error Assessment

6.2.1 The VAD motion simulator

The VAD algorithm enables the retrieval of the three components of the wind-speed vector from a vertically-pointing, conically-scanning Doppler lidar, as is the case of the ZephIR™300. Under the assumption of a constant wind vector, it can be shown that the radial wind speed component along the lidar LoS as a function of the scan time follows a sinusoidal pattern (the so-called VAD pattern).

The wind speed components can be retrieved from the amplitude and offset and this sinusoidal pattern by using geometrical considerations and a simple least-squares fitting procedure (*Fujii and Fukuchi*, 2005; *Clifford et al.*, 1994).

The VAD algorithm enables to retrive the wind-vector components (u, v, w) by combining the wind-speed projections along each LoS (i.e. the radial speed on each LoS) over a conical scan (*Banakh et al.*, 1995; *Fujii and Fukuchi*, 2005). Fig.6.1 shows the case of a vertically pointing lidar system with a scanning cone containing multiple LoS. In the case of the ZephIR lidar, the LoS are scanned in a cone with a 30-deg inclination from the vertical. 50 LoS are combined in each conical scan at a frequency of 1 scan/s.

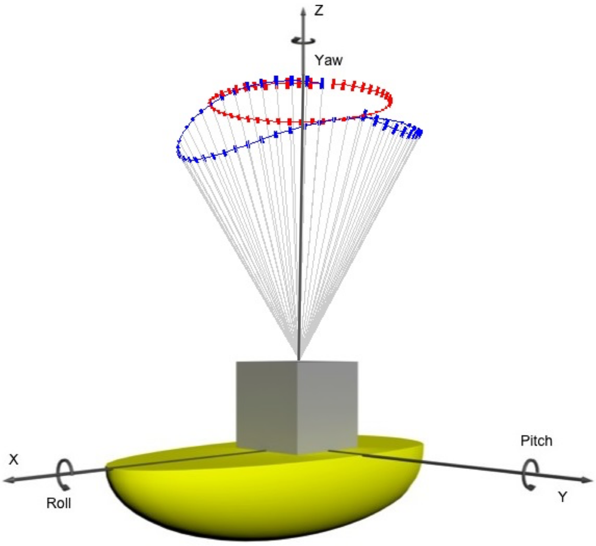

Figure 6.1: Schematic of the geometry of the VAD conically-scanning technique (*Banakh et al.*, 1995; *Fujii and Fukuchi*, 2005) and lidar rotational motion (Euler angles).

6.2.2 Foundations of the VAD simulator

This section describes the VAD simulator conceived at CommSenslab. According to Euler's rotation theorem, any rotation can be described by three angles. There are several conventions for Euler angles, depending on the axes where the rotations are carried out. Here is used roll-pitch-yaw angle (x-y-z convention), where ψ is roll, θ is pitch and ϕ is yaw. The rotation matrix defining the composite rotation or *rotated coordinate system* can be written as:

$$R = R_{\psi} R_{\theta} R_{\phi}, \tag{6.1}$$

where R_{ψ}, R_{θ}, and R_{ϕ} are the component rotation matrices describing a clockwise rotation about x-axis (roll), y-axis (pitch), and z-axis (yaw), respectively.

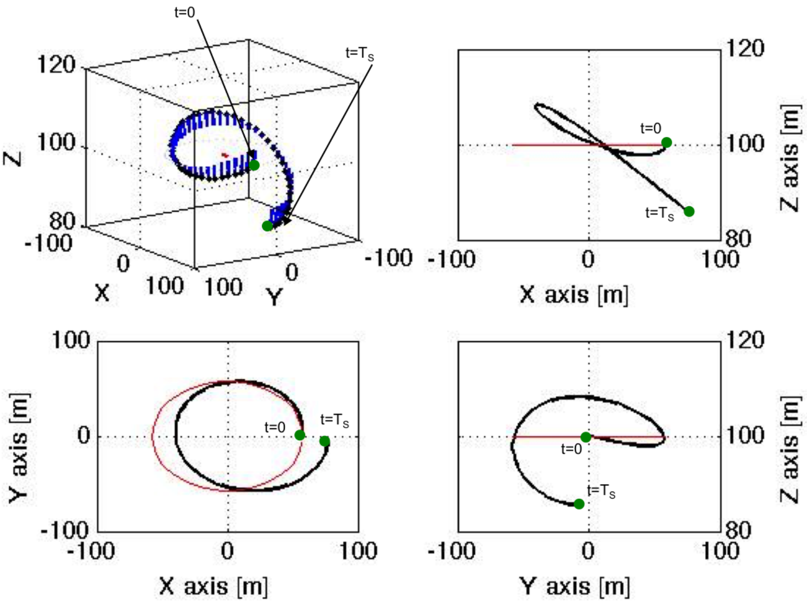

Figure 6.2: Example of a single conical scan for a fixed (red) and moving (black) lidar buoy. Blue lines represent the LoS velocity vector in the rotated coordinate system, $\vec{v}_{LoS}^{rot}$. Red lines show the scanning trajectory in the fixed reference coordinate system. T_s stands for the total scanning time.

$$\begin{aligned} R_\psi &= \begin{bmatrix} 1 & 0 & 0 \\ 0 & \cos(\psi) & \sin(\psi) \\ 0 & -\sin(\psi) & \cos(\psi) \end{bmatrix}, \\ R_\theta &= \begin{bmatrix} \cos(\theta) & 0 & -\sin(\theta) \\ 0 & 1 & 0 \\ \sin(\theta) & 0 & \cos(\theta) \end{bmatrix}, \\ R_\phi &= \begin{bmatrix} \cos(\phi) & \sin(\phi) & 0 \\ -\sin(\phi) & \cos(\phi) & 0 \\ 0 & 0 & 1 \end{bmatrix}. \end{aligned} \tag{6.2}$$

By using roll-pitch-yaw angles, obtained from time-series from the IMUs of the lidar buoy, the geometry of the problem or *lidar attitude* (Fig. 6.2) can be known at each succesive scanning LoS. As a result the problem is invertible (i.e., has an inverse function). Finally, each LoS and the corresponding LoS velocity can be written as

$$\begin{aligned} \hat{r}_{LoS}^{rot} &= \mathbf{R} \cdot \hat{r}_{LoS}, \\ \vec{v}_{LoS}^{rot} &= \vec{v}_{LoS} \cdot \hat{r}_{LoS}^{rot}, \end{aligned} \tag{6.3}$$

where $\hat{r}_{LoS}$ is a unit vector along the LoS, $\vec{v}_{LoS}$ is the LoS velocity vector, $\mathbf{R}$ is the rotation matrix of Eq. 6.1. $\hat{r}_{LoS}^{rot}$ and $\vec{v}_{LoS}^{rot}$ are the counterparts of $\hat{r}_{LoS}$ and $\vec{v}_{LoS}$ in the rotated coordinate system. Superindex "*rot*" is a reminder of "rotated coordinate system".

6.3 Motion-Induced HWS Error Variance

6.3.1 Formulation

This section introduces the methodology used to estimate the HWS error variance induced by lidar motion. This assumes no “a priori” information about the radial wind component measured by each LoS of the scanning pattern.

As mentioned in Sect. 6.2.1, the VAD simulator retrieves the motion-corrupted HWS (1-s resolution) in response to roll and pitch harmonic motion, lidar scan phase, and HWS and WD at a given measurement height. In turn, each degree of freedom (roll/pitch) is characterised by three variables—namely, amplitude, period, and phase. Therefore, the HWS retrieved by the VAD motion simulator can be expressed as

$$\overline{HWS} = h(HWS, WD, H, A_r, \phi_r, T_r, A_p, \phi_p, T_p, \phi_s), \tag{6.4}$$

where h is the non-linear function modelling the VAD-fitting algorithm, H is the measurement height, and A, ϕ, and T are the amplitude, phase, and period associated to sinusoidal roll/pitch motional excitation, $A \cdot sin(2\pi ft + \phi)$, with $f = \frac{1}{T}$ (subscripts r and p stand for roll and pitch angles, respectively), and ϕ_s is the conical scan phase of the lidar.

Horizontal Wind Speed (HWS), WD, and roll/pitch amplitudes and periods ($A_{r/p}$, $T_{r/p}$, respectively) are deterministic variables because they can be measured experimentally (e.g., HWS and WD from metmast anemometers or a reference fixed lidar, and roll/pitch amplitudes and periods from IMUs on the buoy). In contrast, roll/pitch motional phases, $\phi_{r/p}$, and VAD scan phase, ϕ_s, become random variables because buoy initial motion conditions ($\phi_{r/p}$) cannot be recovered from IMU measurements, nor is the scan phase (ϕ_s) available from the lidar.

For convenience, is defined the HWS-error function g as Eq. (6.4) above, constrained to the set of deterministic conditions $\vec{S} = (HWS, WD, A_p, T_p, A_r, T_r)$ (i.e., given HWS, WD, and buoy attitude) minus the true HWS,

$$Z = g(\phi_r, \phi_p, \phi_s) = h|_{\vec{S}} - HWS. \tag{6.5}$$

The motion-induced HWS error variance can be estimated from the first and second raw moments of Z as

$$Var(Z) = E(Z^2) - E(Z)^2. \tag{6.6}$$

By using the expectation theorem (*Barlow*, 1989), the first two raw moments of Z can be computed as

$$E(Z^n) = \int_{-\infty}^{\infty}\int_{-\infty}^{\infty}\int_{-\infty}^{\infty} g(\phi_r, \phi_p, \phi_s)^n f_{\Phi_r\Phi_p\Phi_s}(\phi_r, \phi_p, \phi_s) d\phi_r d\phi_p d\phi_s, \tag{6.7}$$

where $f_{\Phi_r\Phi_p\Phi_s}(\phi_r, \phi_p, \phi_s)$ is the joint probability distribution function for the random-variable set of phases, Φ_r, Φ_p, and Φ_s; and $n = 1, 2$. At this point, and following standard notation in probability theory, (*Papoulis*, 1965) is used upper-case Greek letters to denote random variables and lower-case letters to denote the values for these variables.

Formulation of the multivariate distribution function $f_{\Phi_r\Phi_p\Phi_s}(\phi_r,\phi_p,\phi_s)$ can largely be simplified by introducing different properties describing the statistics of random variables Φ_r, Φ_p, and Φ_s. It is hypothesised that information about any one of these three variables gives no information about the other two, which is equivalent to saying that phases Φ_r, Φ_p, and Φ_s are independent random variables. This will be further discussed in Sect. 6.3.2. As a result, joint density function $f_{\Phi_r\Phi_p\Phi_s}$ factors out as the product of univariate functions f_{Φ_r}, f_{Φ_p}, and f_{Φ_s}, as $f_{\Phi_r\Phi_p\Phi_s} = f_{\Phi_r} f_{\Phi_p} f_{\Phi_s}$. This enables us to rewrite Eq. (6.7) as

$$E(Z^n) = \int_0^{2\pi}\int_0^{2\pi} f_{\Phi_r}(\phi_r) f_{\Phi_p}(\phi_p)\left[\int_0^{2\pi} g(\phi_r,\phi_p,\phi_s)^n f_{\Phi_s}(\phi_s)d\phi_s\right]d\phi_r d\phi_p, \tag{6.8}$$

where it has been used that random variables Φ_r, Φ_p, and Φ_s are *uniformly* distributed in $[0,2\pi)$ so that

$$f_\nu(\nu) = \frac{1}{2\pi}, \nu \in [0,2\pi)\ with\ \nu = \phi_r,\phi_p,\phi_s. \tag{6.9}$$

The hypothesis of uniform distribution in $[0,2\pi)$ for scan phase Φ_s is well-justified on account of the fact that, despite the 1-s temporal resolution of the lidar, measurements are not exactly delivered every second due to lidar refocusing and internal checkings.

The following expression is defined,

$$g_n'(\phi_r,\phi_p) = \int_0^{2\pi} g(\phi_s)^n\Big|_{\Phi_r=\phi_r,\Phi_p=\phi_p} f_{\Phi_s}(\phi_s)d\phi_s, \tag{6.10}$$

which can physically be understood as the n-th raw moment of the HWS error due to random variable scan phase, Φ_s, for a given pair of roll and pitch phases, $\Phi_r = \phi_r$ and $\Phi_p = \phi_p$. Equivalently, Eq. (6.10) can be written as

$$g_n'(\phi_r,\phi_p) = E(g(\phi_s)^n\Big|_{\Phi_r=\phi_r,\Phi_p=\phi_p}, \tag{6.11}$$

which is the expected value of $g(\phi_s)^n$ for a particular pair of motional phases $\Phi_r = \phi_r$ and $\Phi_p = \phi_p$. Because f_{Φ_s} is a uniform probability density function, the expected value is just the arithmetic mean of $g(\phi_s)^n$ along the Φ_s dimension. By substituting Eq. (6.10) into Eq. (6.8), Eq. (6.8) takes the form

$$E(Z^n) = \int_0^{2\pi} f_{\Phi_r}(\phi_r)\left[\int_0^{2\pi} g_n'(\phi_r,\phi_p) f_{\Phi_p}(\phi_p)d\phi_p\right]d\phi_r. \tag{6.12}$$

By comparing Eq. (6.12) to Eq. (6.8) above, it emerges that is reduced the calculus from the tri-dimensional domain $[\Phi_r,\Phi_p,\Phi_s]$ in Eq. (6.8) to the bi-dimensional domain $[\Phi_r,\Phi_p]$ in Eq. (6.12). The same procedure above can be repeated recursively to reduce Eq. (6.12) from the bi-dimensional domain $[\Phi_r,\Phi_p]$ to the one-dimensional domain, $[\Phi_r]$. Thus, in similar fashion to Eq. (6.10) it is defined

$$g_n''(\phi_r) = \int_0^{2\pi} g_n'(\phi_p)\Big|_{\Phi_r=\phi_r} f_{\Phi_p}(\phi_p)d\phi_p, \tag{6.13}$$

which can also be written as (counterpart of Eq. (6.11))

$$g''_n(\phi_r) = E(g'_n(\phi_p)\Big|_{\Phi_r=\phi_r} . \tag{6.14}$$

Substitution of Eq. (6.13) into Eq. (6.8) yields

$$E(Z^n) = \int_0^{2\pi} g''_n(\phi_r) f_{\Phi_r}(\phi_r) d\phi_r, \tag{6.15}$$

or, equivalently,

$$E(Z^n) = E(g''_n(\phi_r)), \tag{6.16}$$

which is to say that the raw moments of the HWS error function Z can be calculated by using a three-step procedure given by Eqs. (6.11), (6.14), and (6.16), where the contribution from each random variable (i.e., roll phase, Φ_r, pitch phase, Φ_p, and scan phase, Φ_s) are successively averaged out.

The practical computational procedure of Eqs. (6.11), (6.14), and (6.16) is as follows: for a given set of simulation parameters $\vec{S} = (HWS, WD, H, A_p, T_p, A_r, T_r)$, the HWS error (Eq. (6.20)) is calculated by the motion simulator of Sect. 6.2.1 in the $[0 - 2\pi) \times [0 - 2\pi) \times [0 - 2\pi)$ domain of random phases Φ_r, Φ_p, and Φ_s by using a grid of $24 \times 24 \times 24$ evenly spaced points between 0 and 2π. This gives a 3D matrix of HWS error values similar to the 2D matrix represented in Fig. 6.10, but in three dimensions. Then, the HWS error is averaged along the Φ_s (scan phase) dimension of the matrix for every pair of roll/pitch phase values (ϕ_r, ϕ_p) to obtain g'_1 (1st raw moment, Eq. (6.11)). Next, this procedure is repeated recursively over the Φ_p dimension of g'_1 (now a 2D instead of a 3D matrix) to yield g''_1 (a 1D matrix or vector, Eq. (6.14)), and finally, over the Φ_r dimension of g''_1, which yields the scalar $E(Z)$ (Eq. (6.8)). This three-step procedure is repeated twice to compute $E(Z)$ and $E(Z^2)$. Finally, the sought-after HWS error variance, $Var(Z)$, is obtained from Eq. (6.6). The standard deviation of the motion-induced HWS error, σ_Z, is computed as the square root of the variance.

6.3.2 Roll/Pitch correlation hypothesis

As described by vector $\vec{S}$ (Eq. (6.5)), besides the input parameters directly related to the wind (i.e., HWS and WD), the simulator requires roll and pitch angular amplitude and period information to describe buoy attitude. This information is derived from 5 Hz IMU data on the buoy (*Gutierrez-Antunano et al.*, 2017). It is hypothesise that if significant correlation between roll and pitch periods and between roll and pitch amplitudes is found, these two angular variables can be considered equivalent and, therefore, a single amplitude and period can meaningfully be used to describe motion in both axes. Thus, for each 10-min timestamp, the motional amplitude is computed as the average roll and pitch angular amplitude, and the motional period as the average roll and pitch period. This is to say that buoy attitude can be given by significant wave height and wave period, which is a state-of-the-art practice in oceanography and wind energy to model the sea state. To evaluate this hypothesis, Fig. 6.3 shows roll–pitch scatter plots for both amplitude and period variables as measured by inertial measurement units during the study period. The pitch-to-roll determination coefficients in angular amplitude and period were 0.88 and 0.54, respectively, demonstrating the validity of the correlation hypothesis for the amplitude and a comparatively weaker correlation for the period. The determination coefficient is equivalent to the cross-covariance at zero time lag (see inset). Further experimental analysis showed that this comparatively lower correlation is due to the bi-modality behaviour of the angular period, which means that two dominant motional periods (or frequencies) coexist in many measurement records. In this case, the single-frequency harmonic motion model becomes an oversimplification of reality, this being the main limitation of the method.

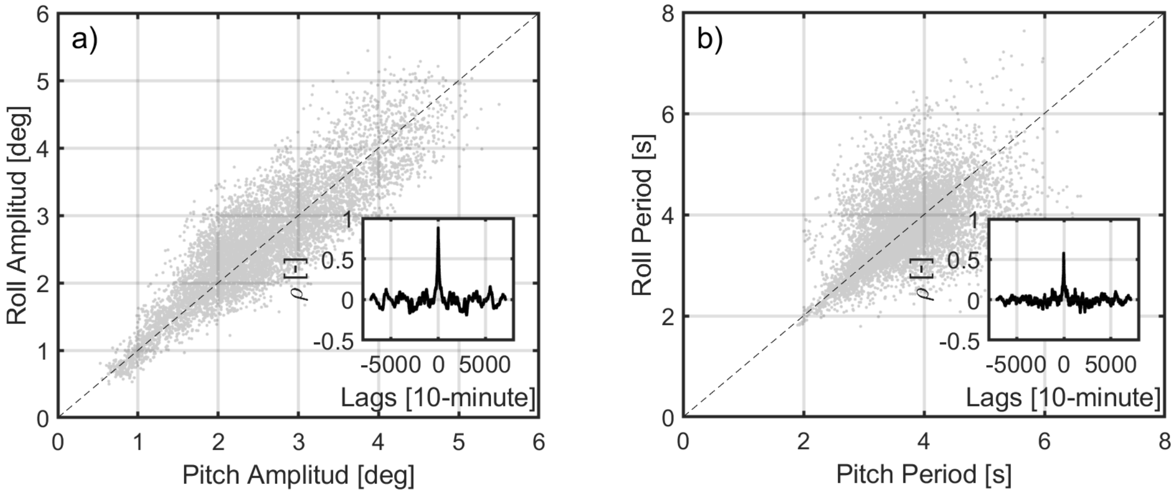

Figure 6.3: Scatter plots for 10-min-averaged roll and pitch angles. (a) Angular amplitude; (b) Angular period. Dashed lines correspond to the 1:1 reference line. Insets show the roll–pitch cross-covariance for different time lags.

6.3.3 Wind direction

In previous works (*Tiana-Alsina et al.*, 2017) limited to one degree of freedom in angular motion (i.e., roll or pitch only) the authors have shown that WD has a relevant impact on the HWS error. Besides, under one-degree-of-freedom harmonic motion it has been shown that the HWS error exhibits sinusoidal dependence with WD.

Under the two-degrees-of-freedom model and the approximation of nearly correlated roll and pitch motion (Sect. 6.3.2), the HWS error was simulated for different WDs (0, 30, 60, ..., 330 deg) and periods (1, 1.5, 2, 2.5, ..., 10 s) for a particular pair of values, HWS (10 m/s) and angular amplitude (3.5 deg). Fig. 6.4 shows the increase of the motion-induced HWS error standard deviation for low angular periods and that the error standard deviation does not depend on WD.

A plausible explanation is as follows: the fact that roll and pitch are approximately linearly correlated in amplitude and period enables an equivalent one-degree-of-freedom treatment of buoy motion (buoy tilt “amplitude” and buoy tilt “period”). Because the HWS error standard deviation follows a sinusoidal variation with WD (*Tiana-Alsina et al.*, 2017) and roll and pitch axes are orthogonal ($\pi/2$ phase shift between roll and pitch sinusoidal variation with WD), the error standard deviation, which is the quadratic sum of roll and pitch error standard deviations, remains constant

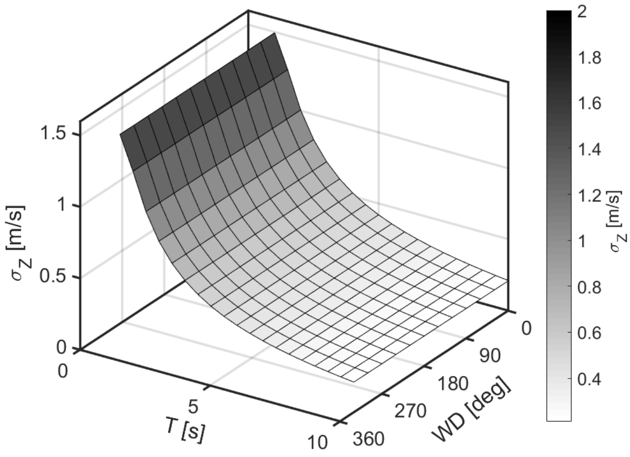

Figure 6.4: Simulator results of motion-induced HWS error standard deviation, σ_Z as a function of motional period, T (X-axis) and WD (Y-axis). HWS is 10 m/s HWS, roll-and-pitch amplitude is 3.5 deg.

with WD. Similar simulations were carried out for other HWSs and angular amplitude conditions, showing analogous behaviour with WD. Therefore, under the approximation of correlated roll and pitch motion, WD was excluded from the analysis.

6.3.4 Variance of the sum of partially correlated variables

Next, it is discussed how to combine the motion-induced HWS error standard deviation, σ_Z, estimated by the simulator (Sect. 6.3), with the reference HWS standard deviation, σ_{ref}, which is measured from either the lidar on the metmast, $\sigma_{ref(lidar)}$, or the sonic anemometer, $\sigma_{ref(sonic)}$, in order to estimate the *motion-corrected HWS standard deviation,* σ_{corr}. The latter is the key output of our study to be compared with the HWS standard deviation measured by the floating lidar, σ_{moving}.

According to the law of propagation of errors, the corrected variance, σ^2_{corr}, of the sum of two variables (the real wind speed (or reference), HWS, and the motion-induced HWS error, Z; Eq. (6.20)) is written as (*Barlow*, 1989)

$$\sigma^2_{corr} = \sigma^2_{ref} + \sigma^2_Z + 2\ cov(ref, Z), \tag{6.17}$$

where σ^2 stands for variance (i.e., the square of the standard deviation) and $cov(ref, Z)$ is the covariance between the reference HWS and the motion-induced HWS error.

Eq. 6.17 above states that the standard deviation of the HWS measured by the moving lidar not only depends on the variance from both the wind (intrinsic turbulence) and the motion-induced error, but also on the covariance between these two variables. In the limit cases of: (i) uncorrelated variables (U), $cov(ref, Z) = 0$, and (ii) linearly correlated variables (C), $cov(ref, Z) = \sigma_{ref} \cdot \sigma_Z$, Eq. (6.17) reduces to

$$\sigma^U_{corr} = \sqrt{\sigma^2_{ref} + \sigma^2_Z}, \tag{6.18}$$

$$\sigma_{corr}^{C} = \sigma_{ref} + \sigma_{Z}. \tag{6.19}$$

In what follows, and unless otherwise stated, the motion-corrected HWS standard deviation σ_{corr} is calculated assuming partial correlation between these variables (i.e., by using Eq. (6.17)). The term $cov(ref, Z)$ is computed from the determination coefficient between the reference HWS, ref, and the expected value of the motion-induced HWS error, $E(Z)$. Here, is used the mathematical definition $cov(ref, Z) = \rho_{ref,Z} \cdot \sigma_{ref} \cdot \sigma_{Z}$, where $\rho_{ref,Z}$ is the determination coefficient, and σ_{ref} and σ_{Z} are the standard deviations of the 10-min reference HWS and 10-min motion-induced HWS error, respectively. In practice, and considering that the binning process ensures similar motional characteristics in each bin (Sect. 6.4.2.A), a single ordered pair (reference HWS, $E(Z)$) per bin (109 simulations) is computed and a single determination coefficient given these 109 bins ($\rho = 0.78$), which is representative of the motional conditions of the overall sample under study.

6.4 Results

This Section presents discussion results on the application of Sects. 6.2-6.3 methodology for the assessment of the motion-induced HWS standard deviation. First, synthetic data will be used to illustrate the behaviour of the VAD simulator (Sect. 6.2). Second, the statistical approach developed in Sect. 6.3 will be applied to IJmuiden's data. Finally, the latter results will be applied to assess the impact of motion on the apparent TI.

To validate the simulator's performance (Sect. 6.2) when estimating the motion-induced HWS error standard deviation on the floating lidar (in the buoy), data from metmast IJmuiden (Sect.5.2.1) was used. Two sensors were chosen as reference: (i) the ZephIR™300 lidar and (ii) the sonic anemometers in the metmast. The intercomparison was carried out at 10-min temporal resolution.

On one hand, the advantage of using the fixed lidar as reference is that two identical lidars are compared although configured to sequentially measure at a different number of heights (the lidar in the metmast measured at 10 heights while the lidar in the buoy at only 3). On the other hand, the advantage of using sonic anemometers is that this technology is more accepted by the wind industry and more similar to the cup anemometer, the official sensor reference in the state-of-the-art. This is because both sonic and cup anemometers perform point-like measurements as opposed to the volume scanning technique of the lidar.

There is only one measurement height in common for the three collocated devices: 85 m. Therefore, this height was the one used in for the comparison.

6.4.1 Application of the VAD motion simulator to synthetic data

A *motion simulator* with the constitutive Eqs. 6.1-6.3 above has been implemented. A time-static and spatially-uniform wind vector is used, thus being the main oversimplification. Thus, a constant wind field exclusive of wind-field random fluctuations is used. The simulated motional behaviour can either be static or periodic (sinusoidal like, in the present case). System parameters are the intensity [m/s] and direction [deg] of the simulated wind-field, the amplitude and frequency of the rotational motion. In the following and for the sake of comparison, the angular frequency is $f_{\mathrm{tilt}} = 0.3$ Hz, the reference velocity is $\vec{v}_{ref}$ =(10,0,0) and the measurement height is h = 100 m.

The simulator uses Euler's angles to compute the rotated LoS vector at a given time in response to simultaneous pitch, roll, and yaw tilting angles (three degrees of freedom). Because the rotation matrix of the buoy can numerically be computed as a function of discrete time in response to harmonic excitations in these three angles, it is possible to compute the rotated set of lines of sight of the lidar for each conical scan in response to buoy motion. When the VAD retrieval algorithm is applied to the radial wind speed onto the rotated set of lines of sight, the motion-induced HWS is retrieved with a temporal resolution of 1-s (scan period of the ZephIR™300). In principle, the simulation process is complicated by the existence of three degrees of freedom, each one being described by three variables (i.e., amplitude, phase, and frequency) representing the sinusoidal excitation. In practice, dependence on the yaw is not considered because yaw motion can be considered static as compared to the lidar scan period. Therefore, WD errors caused by yaw motion are corrected by means of the buoy compass. The fact that the scan phase of the lidar scanning pattern (i.e., the starting LoS of the scanning pattern at time zero) is completely uncorrelated with buoy roll/pitch movement forced us to carry out the study by defining different constraints on these variables (this is further discussed in Sections 6.3–6.3.2). Thus, two simple cases were considered in the publication above: static and dynamic buoy tilting.

6.4.1.A Static tilting

The first simulation case studies the effect of static tilt about the pitch axis. Motion angles range from 0 to 15 deg, HWS from 0 to 20 m/s and WD from 0 to 360 deg. The HWS error is a signed quantity obtained as the difference

$$Z = \overline{HWS} - HWS, \tag{6.20}$$

where HWS is the real wind speed and $\overline{HWS}$ is the VAD-retrieved HWS.

Fig. 6.5 gives an example of the impact of an static inclination in the VAD representation to the wind vector presented previously on Fig. 2.3, $\overrightarrow{\mathrm{V}} = <0,\ 1,\ 0>\ [m/s]$.

In this case, the fit of the corrupted LoS (blue dots) has an offset that introduces an error in the retrieved wind vector, therefore, the retrieved wind vector will be $\overrightarrow{\mathrm{V}}_{rot} = <0,\ 0.976,\ -0.216>$.

Figure 6.6a does the parameter study by varying the WD and the pitch amplitude in the ranges above while keeping the wind speed constant (10 m/s over x-axis). In response, Fig. 6.6a shows a systematic underestimation of the HWS which monotollicaly grows as the tilt amplitude increases. Here, it is worth noting that the HWS error goes to zero when the WD is aligned with the rotation axis (y-axis for the pitch angle). This is an expected result since the projected wind vector on the tilted scanned cone gives a ymmetric number of LoSs with over/under-estimated radial speeds. On the other hand Fig. 6.6b does now the parametric study by varying the HWS pitch amplitude while keeping a constant WD (0 deg). Figure 6.6a shows that the error increases when the wind-speed intensity also increases. In spite of the specific set of values used to vary the HWS, it is worth noting that the relative error on the HWS (i.e., the ratio between the HWS error and the input

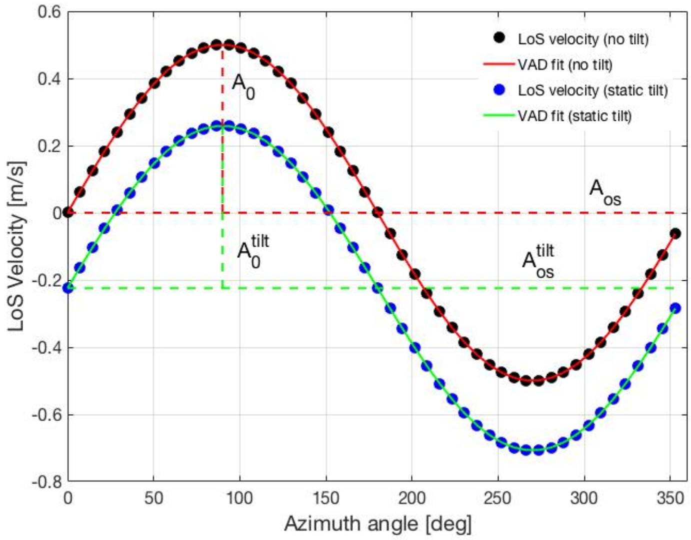

Figure 6.5: VAD representation of the LoS velocity (Y-axis) as a function of the azimuth angle (X-axis). Synthetic values (dots) and sinusoidal fit (traces). No tilting (black dots, red trave) and static tilted (blue dots, green trace).

HWS, figure not shown) remains constant for a given tilt angle. Analogous results (though 90 deg shifted) are reencountered when the simulation is performed for the roll angle.

6.4.1.B Dynamic tilting (I)

Fig. 6.7 gives an example of the effect of a dynamic tilting in the VAD representation.

As shown in Fig. 6.7 the error is no longer constant, as it can be positive or negative depending on the conditions of the motion.

Next, error performance on the retrieved HWS for the case of sinusoidal pitch tilt is studied. These two basic cases considered are limited to these specific constraints:

- Only one degree-of-freedom (either roll or pitch)
- Zero initial phase of the angular movement
- Zero scan phase of the VAD scanning pattern.

The simulation frequency chosen is 0.3 Hz because is a typical figure measured in similar lidar buoys in the nearshore Mediterranean Sea (*Grifoll et al.*, 2016). The initial phase is 0 deg, corresponding to the lidar scanning cone pointing in the vertical direction (i.e. no initial tilt). Figure 6.8 shows the error performance for the same parameter space as in Figure 6.6. The results obtained differ from the ones shown with a static tilt because both negative and positive biases are retrieved while sweeping the WD. The two points marked white and black are choosen as representative of such positive and negative biases.

Figure 6.9 gives a more in-depth discussion for the two selected points. Thus, Fig. 6.9 shows the projections of the reference wind vector ($\vec{v}_{ref} = (u, v, w)$, $w = 0$ for horizontal wind) over the rotated coordinate system during one scan period of the lidar as well as the retrieved VAD velocity

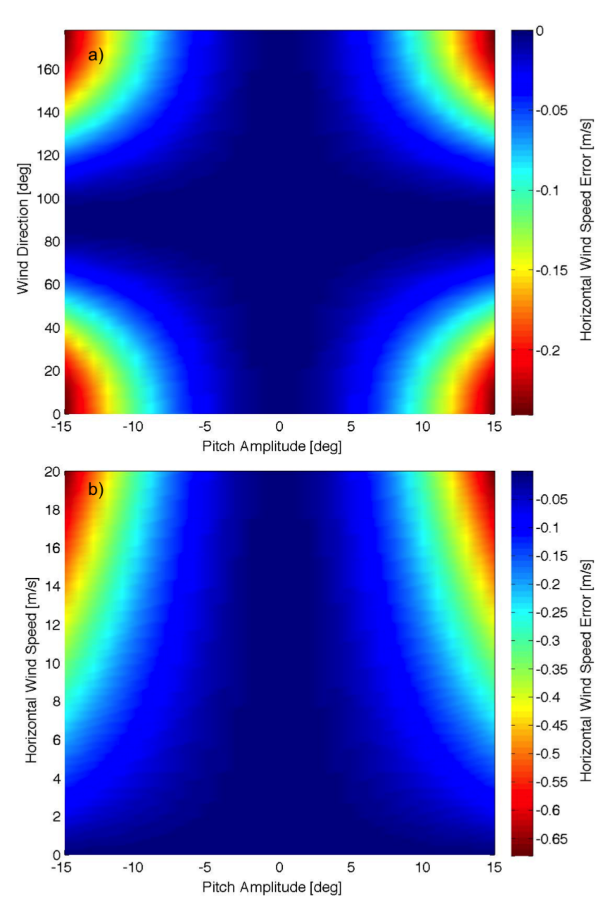

Figure 6.6: Error behaviour of the retrieved HWS in response to static tilt. (a) Different WD. (b) Different HWS.

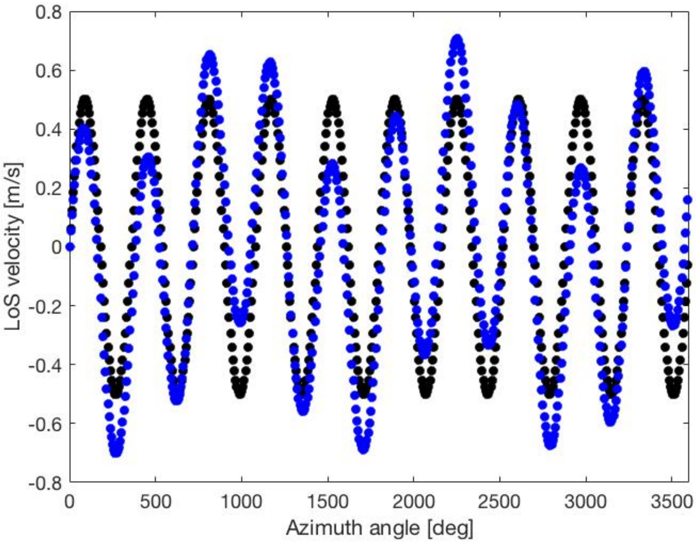

Figure 6.7: VAD representation of the LoS velocity (Y-axis) as a function of the azimuth angle (X-axis). In black no tilt and in blue dynamic tilt.

vector ($\vec{v}_{rot} = (u_r, v_r, w_r)$) for the two study points in (black and white) in Fig. 6.8. Important is to mention that these projections are shown in Fig. 6.9 over the reference (i.e., fixed) coordinate

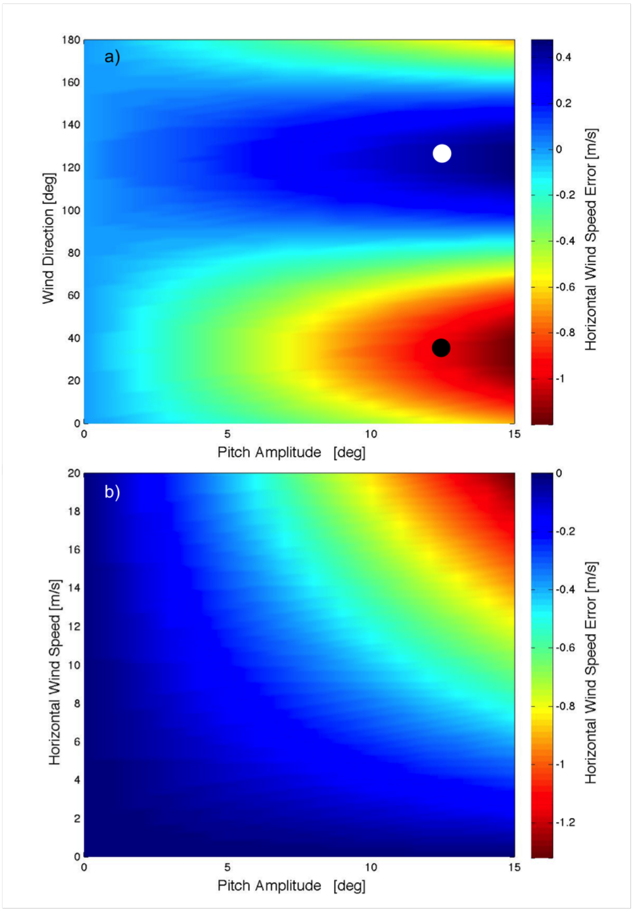

Figure 6.8: Error behaviour of the retrieved HWS in response to sinusoidal pitch tilting ($f_{\text{tilt}} = 0.3$ Hz). (a) For different WD relative to lidar. (b) For different HWS. White and black dots refer to the two case examples analysed in Fig. 6.9 (pitch motion amplitude of 12.5 deg and WD of 35 and 125 deg, respectively).

system XYZ and more specifically, on the XZ, YZ and XY planes. Left and right panels correspond to the black and white points of Fig. 6.8 respectively.

On one hand, for the black-point case (angular amplitude, 12.5 deg; WD, 35 deg; Fig. 6.9a, 6.9b, 6.9c) retrieved velocity components u_r and v_r are slightly underestimated (Fig. 6.9c, blue arrow below the red arrow). Besides, as a consequence of the assymetric amount of tilt of the scanning cone over one scanning period, the VAD algorithm retrieves a net upside vertical component, w_r (Fig. 6.8a, 6.8b). The same figure panels show the underestimation over x- and y- axes.

On the other hand, for the white-point case (angular amplitude, 12.5 deg; WD, 35 deg; Fig. 6.9d 6.9e, 6.9f, i.e. 90-deg rotated with respect to the previous case) the opposite behaviour occurs. This is characterized by an overestimation of the retrieved wind component, u_r and v_r (Fig. 6.9f), and by a net downside vertical component, w_r (Fig. 6.9d 6.9e). Here, it is worth noting the unbalanced behaviour of the absolute error (-1.2 to +0.4 m/s in Fig. 6.8a; -1.3 to 0 m/s in Fig. 6.8b) resulting from asymetries on the LoS velocity projections for different WDs.

6.4.1.C Dynamic tilting (II): Importance of the scan phase

The constraints enunciated at the beginning of Sect. 6.4.1.B are overcome by considering:

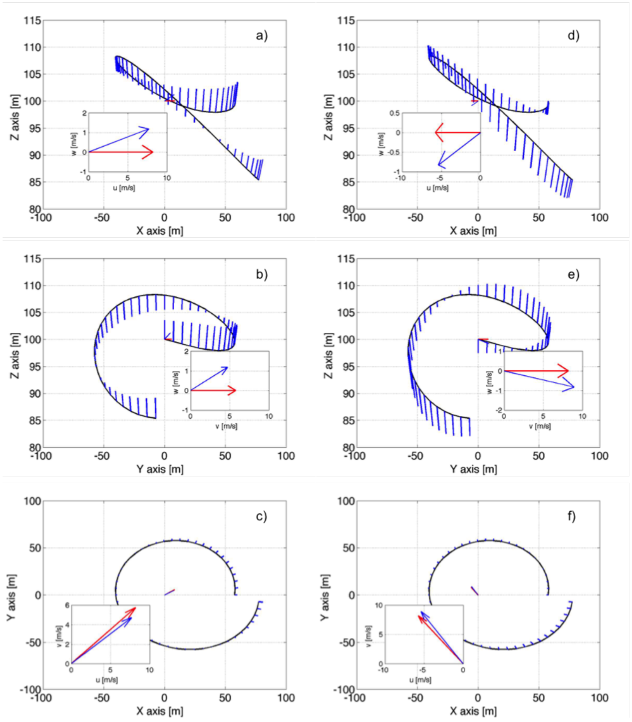

Figure 6.9: Scanning trajectory (black line) and LoS-projected velocities (blue line) during one scanning period of the moving lidar represented over the fixed coordinate system (XZ, YZ, and XY planes). (a, b, c) Black-dot case in Fig. 6.8 corresponding to an angular amplitude of 12.5 deg and WD of 35 deg. (d, e, f) White-dot case corresponding to an angular amplitude of 12.5 deg and WD of 125 deg. Insets represent the reference wind velocity vector (red arrow) and the retrieved one (blue arrow) in the fixed coordinate system.

- The combined contributions from both roll and pitch degrees of freedom.
- All possible phases in roll and pitch motion
- All possible phases in the VAD scan.

To illustrate the importance of these parameters, Fig. 6.10 plots the simulated error on the VAD-retrieved HWS (Eq. (6.20)) under roll-only lidar motion (one degree of freedom) as a function of the scan phase (X-axis), motional angular period (Y-axis), and motional phase (Figures 6.10a–6.10d).

This plot shows that for 10-m/s HWS and 3.5-deg tilt, the HWS error increases to ±10% depending on the lidar scan phase. When comparing top and bottom panels in Fig. 6.10, which account for 180-deg difference in roll phase, positive HWS errors in the top panels translate into negative ones in the bottom panels and vice-versa. Therefore, both the initial phase of movement and that of the VAD scan should be taken into account to evaluate the impact of lidar motion on the HWS error.

6.4.2 Application of the statistical approach to IJmuiden's data

6.4.2.A Binning

As discussed in Sect. 6.3, an underlying requirement of the proposed methodology to estimate motion-induced HWS error variance is the assumption of uncorrelated- and uniformly-distributed

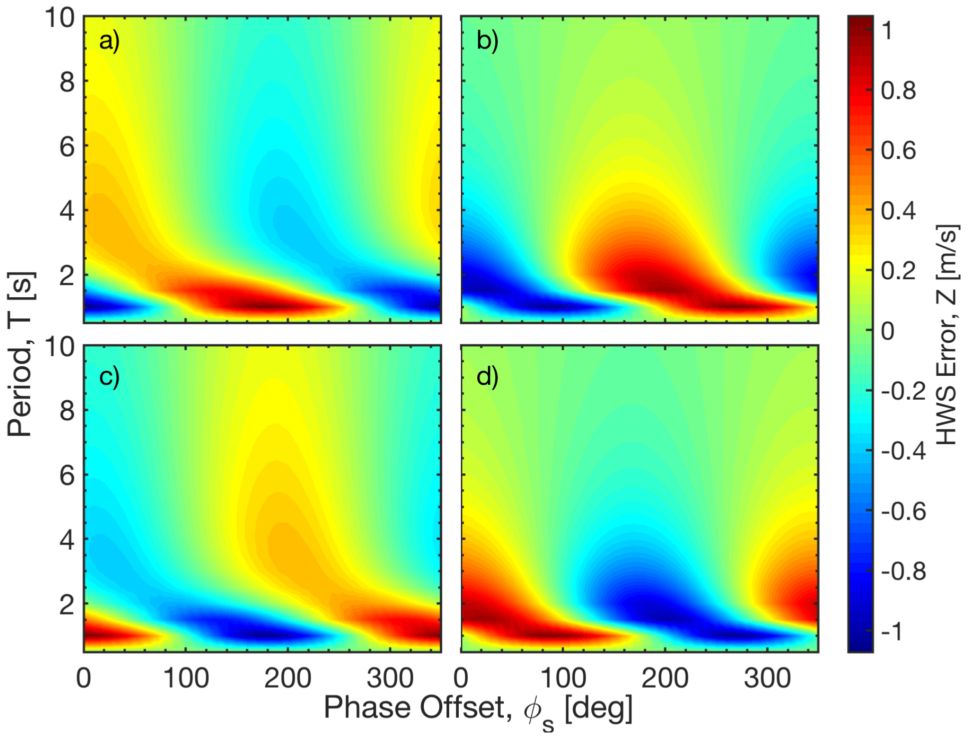

Figure 6.10: Simulated HWS error, Z (Eq. (6.20)), under roll-only motion as a function of VAD scan phase (X-axis) and motional period, T, (Y-axis). Roll phase (ϕ_r) varies for each panel. (a) 0 deg. (b) 90 deg. (c) 180 deg. (d) 270 deg. Roll amplitude is 3.5 deg, wind vector is $(0, 10, 0)$ m/s, and measurement height is 100 m in all panels (*Tiana-Alsina et al.*, 2017).

phases ϕ_r, ϕ_p, and ϕ_s in the floating lidar for each HWS and buoy motional condition under study. To better fulfil this requirement, a binning procedure was applied to the whole campaign dataset (6985 10-min records). As a result, each bin contained measurement records with similar HWSs and motional conditions but not necessarily (and usually not) having correlative timestamps. As a result of this timestamp “mixing” into a bin (also called time “scrambling”), the requirement of uncorrelated and uniformly distributed phases (Sect. 6.3) into a bin was reinforced. The chosen binning variables were: HWS, angular amplitude, and period in equally spaced bins of width 1 unit ((m/s), (deg), and (s), respectively) centred on integer values (bin edges at [0.5 1.5), [1.5 2.5) units, etc.).

Tab. 6.1 shows the 25 most frequent cases in the IJmuiden campaign. The most common HWSs were between 3 and 12 m/s, amplitudes were between 2 and 4 degrees, and motional periods were between 3 and 4 s. The total set of measurement cases is considered in Fig. 6.13and Section 6.4.2.C. The conditions of the site during the study period included HWS between 2 and 21 m/s, angular amplitudes between 1 and 5 deg, and periods between 2 and 5 s.

6.4.2.B Analysis of particular cases

In order to discuss the goodness of the proposed methodology to estimate the motion-induced HWS standard deviation, this section tackles three representative cases (or bins) from Tab. 6.1: cases no. 2, 18, and 25. The first case gave good estimation of the motion-induced HWS standard deviation; the second one, overestimation; and the third one, underestimation.

Table 6.1: The 25 most frequent HWS and motional cases in the IJmuiden campaign. “Case no.” is the bin number sorted by decreasing frequency of event occurrence (“1” indicating the most frequent case); HWS (m/s) stands for 10-min mean HWS; AA (deg) stands for motion angular amplitude; T (s) stands for period; Count no. is the bin count number; and σ_Z (m/s) is the motion-induced HWS error standard deviation estimated by the simulator after Eq. (6.6). Dashed lines highlight test cases.

Case no.	**HWS (m/s)**	**AA (deg)**	T **(s)**	**Count no.**	σ_Z **(m/s)**
1	8	3	4	288	0.18
2	5	2	4	247	0.07
3	9	3	4	237	0.20
4	7	2	4	208	0.10
5	6	2	4	198	0.09
6	7	3	4	196	0.16
7	6	3	4	182	0.13
8	6	2	3	180	0.12
9	3	2	4	175	0.04
10	7	2	3	174	0.14
11	10	3	4	169	0.22
12	5	2	3	166	0.10
13	4	2	4	164	0.06
14	8	2	4	157	0.12
15	8	2	3	133	0.16
16	11	3	4	130	0.25
17	5	3	4	130	0.11
18	9	3	3	112	0.27
19	8	3	3	108	0.24
20	7	3	3	106	0.21
21	12	3	4	100	0.27
22	11	4	4	95	0.33
23	2	1	3	91	0.02
24	4	2	3	86	0.08
25	3	1	3	80	0.03

Fig. 6.11 plots the standard deviation of the HWS with and without correction (Eq. (6.17)), using the lidar on the metmast as reference. The sample size associated to each of these three cases is listed in the "Count no." column of Tab. 6.1.

Fig. 6.11a (case no. 2) shows 247 10-min measurements for which the proposed methodology accurately estimated the standard deviation of the motion-induced HWS error. Before applying Eq. (6.17) correction, uncorrected values fell below the 1:1 line, which indicates that the moving lidar "saw" a higher standard deviation. After Eq. (6.17) correction, most of the measurements laid on the 1:1 reference line.

Figs. 6.11b and 6.11c, which are representative of case nos. 18 and 25, respectively, show two opposite situations: On one hand, for case no. 18 (Fig. 6.11b), the simulator overestimated the influence of motion and the corrected values laid above the 1:1 line. Further investigation showed that this can be caused by the lack of consistency of the roll/pitch correlation hypothesis (Sect. 6.3.2) due to most measurements undergoing bi-modal motion behaviour. On the other hand, case no. 25 (Fig. 6.11c) showed corrected values falling nearly always below the 1:1 line, which means that the estimated correction given by the motion simulator was too low. Further inspection indicated that this underestimation was caused by untrustworthy retrieval of the HWS by the VAD algorithm, as evidenced by too-high SV values from the ZephIR™300 lidar (Fig. 6.12, to be discussed in Sect. 6.4.2.C). The SV is a lidar internal parameter related to the goodness of fit that reveals whether the measurement data is consistent or not with the sinusoidal model assumed by the VAD algorithm. Thus, high SV values are related to a poor VAD fitting, and they are usually found in low HWS, where Taylor's frozen-eddies hypothesis is no longer true and the lidar does not measure a homogeneous wind along the VAD scanning area.

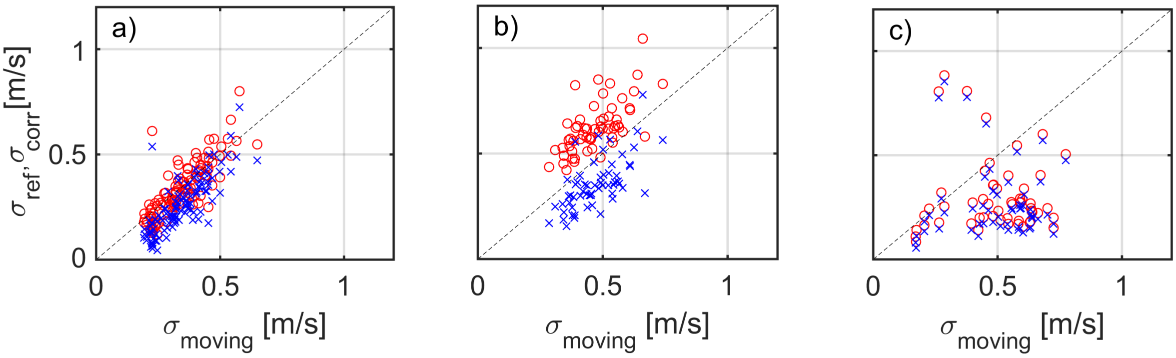

Figure 6.11: Selected discussion case examples from Tab. 6.1. (a) Case no. 2, HWS = 5 m/s; angular amplitude (AA) = 2 deg; period (T) = 4 s. (b) Case no. 18, HWS = 9 m/s; AA = 3 deg; T = 3 s. (c) Case no. 25, HWS = 3 m/s; AA = 1 deg; T = 3 s). All panels: the X-axis represents the 10-min HWS standard deviation of the floating lidar, denoted σ_{moving}. The Y-axis represents (in blue crosses) the standard deviation of the reference-lidar HWS (denoted σ_{ref}) and (in red circles) the standard deviation of the motion-corrected HWS (denoted σ_{corr}). The dashed black line represents the 1:1 reference line.

Tab. 6.2 gives MD and root mean square error (RMSE) indicators for case nos. 2, 18, and 25 in Fig. 6.11 without and with motion correction.

The concepts of MD (equivalently, average bias) and RMSE already introduced in Chap. 2 are applied next to the concept of standard-deviation error.

The motion-corrected MD is defined as

$$MD_{corr} = \frac{\sum_i (\sigma_{moving,i} - \sigma_{corr(x),i})}{N}, \tag{6.21}$$

where N is the case "count no." (Table 6.1), σ_{moving} is the HWS standard deviation measured by the floating lidar (already introduced in Section 6.3.4), and $\sigma_{corr(x)}$ is the motion-corrected HWS standard deviation (Equation (6.17)) of the reference instrument, where $x = lidar$ denotes the reference fixed lidar and $x = sonic$ denotes the sonic anemometer. Subscript i is the count-number index, that is, i went from $i = 1$ to $i = 247$ for case no. 2.

The motion-corrected root mean-square error is defined as

$$RMSE_{corr} = \sqrt{\frac{\sum_i (\sigma_{moving,i} - \sigma_{corr(x),i})^2}{N}}. \tag{6.22}$$

Similarly, uncorrected MD and RMSE indicators are computed by substituting $\sigma_{corr(x),i}$ with $\sigma_{ref(x),i}$, the reference HWS standard deviation, in Eqs. (2.8)–(2.9). These indicators are denoted MD_{ref} and $RMSE_{ref}$, respectively.

As shown in Tab. 6.2, the MD for case no. 2 improved from 0.08 (uncorrected) to 0.02 m/s after motion correction. The RMSE also improved from 0.11 to 0.08 m/s. For overestimation case no. 18, the MD changed sign from 0.12 to -0.12 m/s and for underestimation case no. 25 the MD virtually did not change (from 0.22 to 0.20 m/s). In over/underestimated case nos. 18 and 25, the RMSE did not improve after motion correction by Eq. (6.17). All things considered, these indicators were consistent with the discussion carried out for Figs. 6.11a–6.11c, and they were therefore used to quantitatively analyse the overall campaign in the following.

6.4.2.C Analysis of the whole campaign

In this section is discussed the *overall performance* of the motion-corrected HWS standard deviation, σ_{corr}, calculated via Eq. (6.17) and, for comparison, via Eqs. (6.18)–(6.19), for the whole measurement campaign at IJmuiden (6985 10-min records clustered into 109 cases).

In similar fashion to Fig. 6.11 but for the whole campaign, Fig. 6.12 compares the HWS standard deviation of the moving lidar, σ_{moving}, to the motion-corrected standard deviation (Eq. (6.17)) of the sonic and fixed-lidar reference devices ($\sigma_{corr(sonic)}$ and $\sigma_{corr(lidar)}$, respectively; right panels) and to the uncorrected ones (left panels; labelled $\sigma_{ref(sonic)}$ and $\sigma_{ref(lidar)}$), respectively). Linear regression parameters and determination coefficients, superimposed on Fig. 6.12, clearly improved after applying the correction methodology for both the sonic and the fixed-lidar references. Therefore, better agreement between the floating lidar and the instrumental references was obtained. Despite the improvement, there was a tendency to slightly overestimate the motion-corrected standard deviation, $\sigma_{corr,(x)}, x = sonic, lidar$, for both the sonic and lidar references.

To further investigate this issue, each point in the scatter plots was colour-coded according to the SV given by the floating lidar. Blue dots, which are associated to low SV, exhibited good correlation while poorly correlated points were associated to SV figures above 0.06. These high

Table 6.2: Statistical indicators with and without motion correction for the selected discussion case examples from Tab. 6.1. MD and RMSE units are (m/s) and dashed lines highlight test cases.

Case no.	Count no.	Reference sonic				Reference lidar			
		Corrected		Uncorrected		Corrected		Uncorrected	
		MD	RMSE	MD	RMSE	MD	RMSE	MD	RMSE
1	288	-0.02	0.12	0.14	0.18	-0.02	0.08	0.13	0.16
2	247	0.08	0.15	0.14	0.19	0.02	0.08	0.08	0.11
3	237	-0.03	0.15	0.14	0.20	-0.04	0.11	0.13	0.16
4	208	0.01	0.12	0.10	0.15	0.01	0.07	0.10	0.12
5	198	0.04	0.12	0.12	0.16	0.02	0.09	0.10	0.13
6	196	0.01	0.14	0.14	0.20	-0.01	0.09	0.13	0.16
7	182	0.03	0.12	0.14	0.18	0.00	0.08	0.12	0.14
8	180	-0.02	0.12	0.08	0.14	-0.04	0.11	0.06	0.12
9	175	0.10	0.22	0.13	0.24	0.05	0.08	0.09	0.11
10	174	-0.01	0.13	0.11	0.17	-0.02	0.08	0.10	0.13
11	169	-0.09	0.13	0.10	0.14	-0.07	0.12	0.12	0.16
12	166	-0.01	0.12	0.07	0.14	-0.03	0.12	0.05	0.13
13	164	0.10	0.23	0.15	0.26	0.04	0.09	0.09	0.12
14	157	-0.02	0.09	0.08	0.12	0.02	0.07	0.12	0.14
15	133	-0.05	0.12	0.08	0.13	-0.02	0.07	0.11	0.13
16	130	-0.12	0.16	0.09	0.14	-0.08	0.13	0.14	0.17
17	130	0.07	0.13	0.16	0.20	0.03	0.08	0.13	0.15
18	112	-0.10	0.18	0.14	0.21	-0.12	0.15	0.12	0.15
19	108	-0.09	0.17	0.12	0.18	-0.11	0.15	0.10	0.14
20	106	-0.06	0.13	0.12	0.16	-0.08	0.12	0.09	0.13
21	100	-0.14	0.19	0.09	0.15	-0.09	0.15	0.15	0.19
22	95	-0.11	0.15	0.17	0.20	-0.11	0.17	0.18	0.22
23	91	-0.02	0.14	-0.01	0.14	0.01	0.10	0.03	0.11
24	86	0.08	0.19	0.15	0.22	0.05	0.16	0.12	0.20
25	80	0.20	0.26	0.22	0.28	0.20	0.31	0.22	0.33

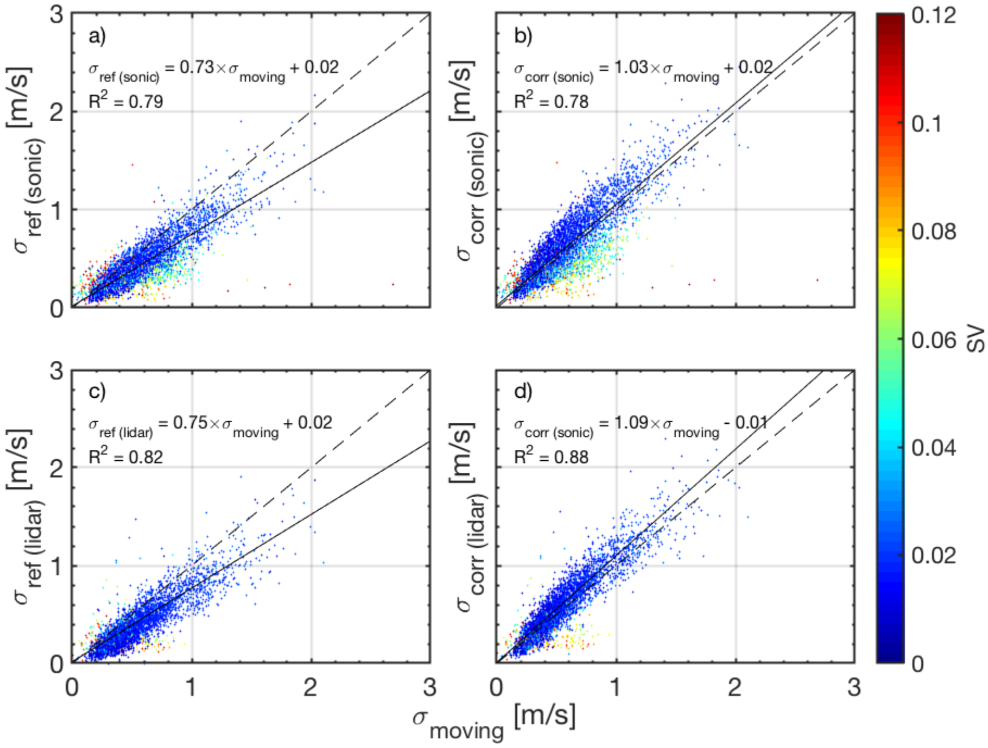

Figure 6.12: Analysis of the whole campaign (109 cases, 6985 10-min measurement records) by using as reference the sonic anemometer (upper panels) and the lidar on metmast (lower panels), without motion correction (left panels; , $\sigma_{ref(sonic/lidar)}$ in the Y-axis) and with motion correction (right panels; $\sigma_{corr(sonic/lidar)}$ in the Y-axis). The X-axis represents the HWS standard deviation of the floating lidar, denoted σ_{moving}. Each point is a 10-min record. Dashed lines represent the 1:1 line. Solid lines plot the regression lines. Color bar indicates SV.

figures were usually due to errors in the VAD-retrieved HWS caused by inhomogeneity of the wind. This means that regression-line results could better approach the ideal 1:1 line by filtering out these outliers on a SV criterion, which is out of the scope of the present work.

To quantitatively discuss the whole campaign via MD and RMSE indicators (Eqs. (2.8–2.9)), Tab. 6.3 presents the results for all 109 cases in the campaign, for both the fixed lidar and sonic references. Results are graphically depicted in the histogram of Fig. 6.13 for the lidar reference only. Fig. 6.13 shows that the motion-uncorrected MD, MD_{ref}, had a positive bias of 0.13 m/s when using the fixed lidar as reference. This bias accounts for the systematic error in the measured HWS standard deviation caused by floating lidar motion as previously reported in (*Gottschall et al.*, 2014; *Gutiérrez-Antuñano et al.*, 2017). After motion correction, the MD_{corr} reduced to the virtually unbiased figure of -0.03 m/s when using the fixed lidar as reference. The negative sign indicates the tendency to overestimate, as mentioned previously. This accounts for an 80% reduction in absolute value. Using the sonic anemometer as reference, the MD reduced from 0.12 to -0.03 m/s (histogram not shown). The RMSE reduced from $RMSE_{ref} = 0.17$ (uncorrected) to $RMSE_{corr} = 0.12$ m/s(motion corrected) when using the lidar reference (this accounts for a 29% reduction) and from 0.18 to 0.16 m/s when using the sonic reference. This is considered evidence of the accuracy of the proposed methodology in estimating the motion-induced standard deviation.

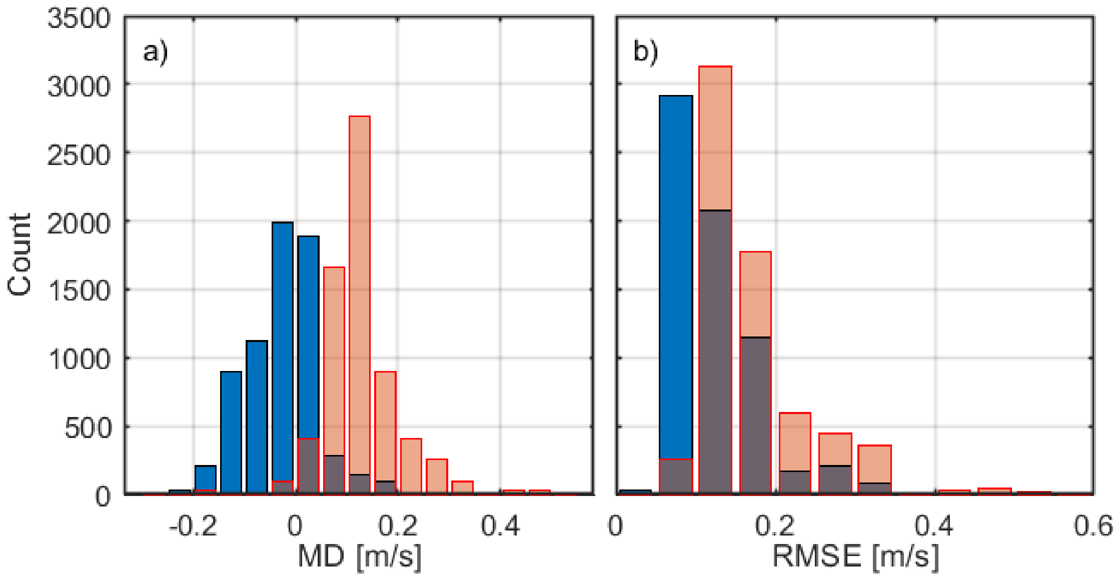

Figure 6.13: Histogram of the main statistical parameters. (a) Mean difference. (b) RMSE using the fixed lidar as reference. All panels: blue = motion corrected, red = uncorrected.

Table 6.3: Performance of the variance-combination laws of Sect. 6.3.4. (C) stands for linearly correlated variables, (PC) for partially correlated, and (U) for uncorrelated.

	Variance-combination law for σ_{corr} (C) Eq. (6.19)		(PC) Eq. (6.17)		(U) Eq. (6.18)		Uncorrected, σ_{ref}	
	Sonic	Lidar	Sonic	Lidar	Sonic	Lidar	Sonic	Lidar
MD	-0.06	-0.05	-0.03	-0.03	0.08	0.08	0.12	0.13
RMSE	0.17	0.13	0.16	0.12	0.15	0.13	0.18	0.17

As a remark,Fig. 6.14 shows similar HWS motion-corrected results to Fig. 6.12d, but under the limit hypotheses of uncorrelation (Eq. (6.18)) and linear correlation (Eq. (6.19)) between the reference HWS, and the motion-induced HWS error, Z. Fig. 6.14 shows that the uncorrelated case and the linear-correlated case can respectively be understood—in a statistical sense over the whole population—as lower (Eq. (6.18)) and upper (Eq. (6.19)) bounds of the proposed motion correction. According to the definition of determination coefficient, $0 <= |\rho| <= 1$, Eq. (6.17) lies in between these two limit cases ($\rho = 0$, $\rho = 1$). This is corroborated in Tab. 6.3, which shows MD and RMSE indicators when the lidar and the sonic anemometer are used as references, for the three combination hypotheses discussed in Sect. 6.3.4: partially correlated (PC), uncorrelated (U) and correlated (C) variables. It emerges that the approximation of partial correlation yielded the best results, as shown by the lowest MD and RMSE figures in Tab. 6.3.

6.4.3 Turbulence intensity

Analogously to Fig. 6.12d, Fig. 6.15a compares the TI of the floating lidar, TI_{moving}, to the motion-corrected TI of the fixed-lidar reference, $TI_{corr(lidar)}$. Dots are colour-coded according to their SV parameter. HWSs below 3 m/s, which are usually out of the production regime of commercial

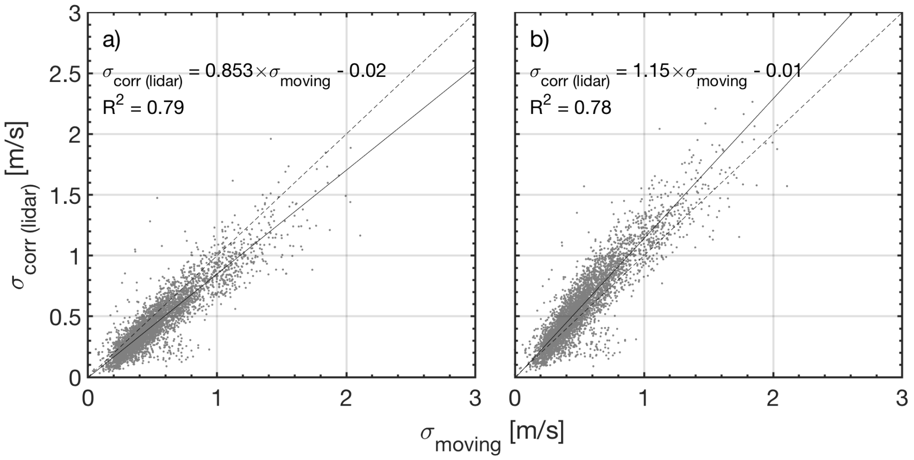

Figure 6.14: Comparison between 10-min floating-lidar HWS standard deviation measurements and motion-corrected ones by using Eq. (6.18) versus Eq. (6.19). (a) Uncorrelation hypothesis (Eq. (6.18)). (b) Linear-correlation hypothesis (Eq. (6.19)). The dashed line indicates the 1:1 line and the solid line shows the linear regression.

wind turbines and tend to numerically distort the TI, were filtered out to enhance the readability of the graph. Although some scattering is present in the pattern of dots, the regression line (slope $=$ 0.86, intercept $=$ 0.01) shows similar tendency to that of Fig. 6.12d of approaching the 1:1 line after motion correction. Quantitatively, by defining similar MD and RMSE indicators for the TI (counterpart of Eqs. (2.8)–(2.9) by changing standard deviation, σ, into TI), the MD for the moving lidar reduced from 0.016 (uncorrected) to 0.003 (motion corrected). In terms of RMSE, the reduction was from 0.018 to 0.012, which despite being not very important implies an approximate 30% reduction in the dispersion of data. Besides, most of the points falling far from the 1:1 line had high SV figures, typically SV $>$ 0.06, which is characteristic of low HWS.

Fig. 6.15b illustrates the successful application of the motion-correction algorithm by superimposing: (i) the TI measured by the uncorrected fixed-lidar reference ($TI_{ref(lidar)}$, red); (ii) the TI derived from the motion-corrected lidar reference ($TI_{corr(lidar)}$, grey); and (iii) the TI measured by the moving floating lidar (TI_{moving}, black) as a function of the 10-min HWS. To aid visual interpretation, average TIs using a 1.0 m/s binwidth were also plotted in red, white, and black traces, respectively. As expected, the *apparent* TI measured by the floating lidar (black trace) was higher than the *true one* measured by the reference lidar (red trace). After application of motion correction to the reference TI, $TI_{ref(lidar)}$ (red dots/red trace), the motion-corrected TI, $TI_{corr(lidar)}$ (grey dots / white trace), approximately followed the floating lidar TI, TI_{moving} (black dots/black trace). At this point, it must be said that, in practice, the correction is to be applied to the TI measured by the floating lidar so as to shift it down. However, this does not change the line of reasoning. Quantitatively, the mean value of the TI measured by the fixed lidar in the 3–20 m/s HWS range was $TI_{ref(lidar)} = 0.047$ and the TI measured by the floating lidar was $TI_{moving} = 0.065$. After motion correction, the mean value of the reference-corrected TI was $TI_{corr(lidar)} = 0.067$, which was only -0.002 apart from TI_{moving} and drastically reduced the initial difference between floating lidar and the reference lidar TI from 0.018 to -0.002. These differences account for an error reduction from 38.3% to 4.3%.

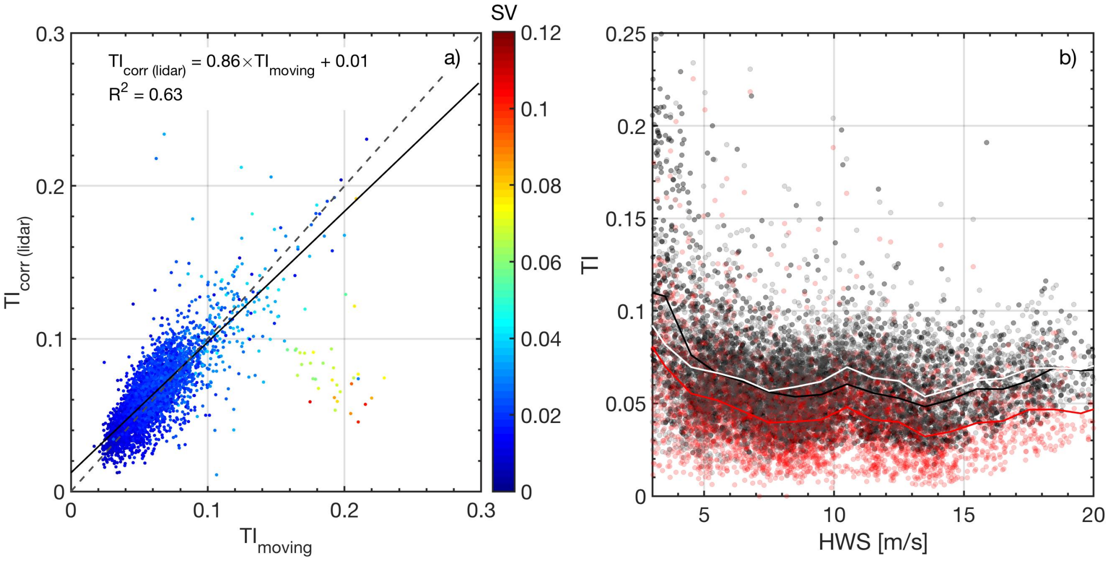

Figure 6.15: TI results for the whole campaign. (a) Comparison between the motion-corrected TI of the fixed-lidar reference, $TI_{corr(lidar)}$ and the floating-lidar TI, TI_{moving}. Colour bar indicates SV. Dashed line indicates the 1:1 line. (b) Plots of TI versus HWS (see text): Red dots = uncorrected fixed-lidar reference, $TI_{ref(lidar)}$. Grey dots = motion-corrected lidar reference, $TI_{corr(lidar)}$. Black dots = floating lidar, TI_{moving}. Traces with the same colours plot average TIs using a 1.0-m/s binwidth.

As discussed in Sect. 6.1, in order to improve the design layout of offshore wind farms and selection of the appropriate wind turbine model, TI measurements of a floating lidar are needed. Performance results from Sect. 6.4.2.C and Sect. 6.4.3 showed that in the environmental conditions considered, the proposed methodology has the potential to estimate the influence of motion on TI measurements with the ZephIR™300 lidar.

6.5 Conclusions

A VAD motion simulation for off-shore wind lidars has been presented (Sect. 6.4.1) for the case of a conically-scanning lidar (50 LoS, 1 scan/s) and VAD velocity-vector retrieval over one scan period. The simulator uses pitch-roll-yaw Euler's angle formulation to relate the LoS-velocity projections of the wind vector and lidar attitude in the fixed coordinate system (reference observation system) to the rotated coordinate system, where the velocity vector is VAD retrieved.

Two main motional lidar cases have been considered to study the HWS retrieval error: static and dynamic (sinusoidal) pitch tilt [angular amplitudes range, $0-15$ deg; wind speed, $0-20$ m/s; and WD, $0-180$ deg, normalised wind velocity (when not parameterized), 10 m/s]. Results are summarised in Figs. 6.6-6.8. The static case has shown that the HWS error is null when the WD is aligned with the rotation axis (Y axis for pitch tilt). For WD between 60 to 120 deg (normalised wind velocity 10 m/s), HWS errors lie between 0 to -0.075 m/s (i.e., -0.75%) while for WD between 0 to 45 deg and 135 to 180 deg display HWS errors between -0.1 to -0.25 m/s (i.e., -1% to -2.5%). The dynamic case has yielded non-symmetric HWS errors that are roughly between $+0.5$ m/s and -1.2 m/s (Fig. 6.8) when the WD is varied in the margin above (normalised wind velocity 10 m/s).

Using this simulator and the mathematical formulation given by Eqs. (6.4-6.16), a methodology to estimate the 10-min motion-induced standard deviation and TI on the retrieved HWS has been presented. This methodology has been applied to a ZephIR™ 300 lidar at a given measurement height without accessing individual LoS information of the lidar scanning pattern or individual 1-s data.

The motion simulator input parameters are the 10-min average HWS and 10-min motional amplitude and period of the floating lidar buoy as well as initial roll/pitch motional phases and lidar scan phase (ϕ_r, ϕ_p, and ϕ_s, respectively). Initially, synthetic data is used to better understand the operation of the simulator (Sect. 6.4.1), both with static and dynamic tilting, and later, the estimation of the variance is applied to real offshore conditions (Sects. 6.4.2-6.4.3). A binning procedure is used to group measurement records into bins with similar HWS and motional conditions. The procedure is aimed at computing the 10-min HWS error standard deviation in each bin by internally sweeping these phases in the $[0, 2\pi)$ range, which therefore become blind inputs to the user.

The method relies on the approximation that roll/pitch amplitudes and periods are linearly correlated on a 10-min basis and that, consequently, only one motional amplitude and period is needed. This one-degree-of-freedom approximation combined with that of simple harmonic motion are the main limitations of the method. Under these hypotheses, the motion-induced HWS standard deviation was proven to be independent of WD, which allows this variable to be neglected in the computations (wind direction errors caused by yaw motion are always corrected by means of the buoy compass).

According to error-propagation laws, the motion-corrected HWS standard deviation (Eq. (6.17)), which combines the motion-induced HWS error and the reference HWS, was shown to depend on the correlation between these two variables and the degree of approximation by which it is estimated. Uncorrelated ($\rho = 0$) and linearly-correlated ($|\rho| = 1$) sub-cases were interpreted as upper and lower bounds of the motion-corrected HWS standard deviation, respectively.

The performance of the proposed methodology (Sects.6.4.2.B-6.4.2.C) was tested as part of a 60-day study period at offshore metmast IJmuiden by using a sonic anemometer and a fixed lidar as reference instruments. The motion-corrected HWS standard deviation and that of the reference HWS (from either the fixed lidar or the sonic anemometer) were compared to the measured floating-lidar HWS standard deviation for the 109 most frequent cases of the campaign. This indicated an overall improvement in the average MD from 0.13 (uncorrected) to -0.03 m/s (motion corrected) and an average RMSE reduction from 0.17 to 0.12 m/s, which essentially means that the floating-lidar and the motion-corrected HWS standard deviation laid on the ideal 1:1 line with a dispersion equal to the RMSE.

When analysing the whole campaign as a function of the SV, the most poorly correlated points were associated to mid-to-high SV (SV $>$ 0.06). Wider dispersion arose when using the sonic anemometer as reference, which was caused by the inherently different wind measurement principle of the sonic as compared to the lidar. Analysis in terms of TI (Sect. 6.4.3) showed similar improvement, evidenced by a reduction in the difference between the reference-lidar and the floating-lidar

TI from 0.018 (uncorrected) to -0.002 (motion corrected).

Despite these good results, they must be interpreted with caution because performance is based on MD and RMSE criteria over the whole statistical sample and not on an individual measurement basis. Overall, in the environmental conditions considered, the proposed methodology holds promise for use in the estimation of the influence of motion on TI measurements with the ZephIR™300 lidar. These results should be extended to other conditions and set-ups which, if proven effective, could eventually be used to correct TI measurements of floating lidars as standalone devices.

Chapter 7

Conclusions

This Chapter gives concluding remarks and tentative outlook of work derived from Chaps. 2-6 of this Ph.D. Thesis.

7.1 Conclusions

- *On quality assessment of the lidars .-*

  A methodology to assess floating-lidar wind-measurement errors in terms of statistical indicators and KPIs has been presented (Chap. 2). Different signal processing and filtering tools applied to the ZephIR 300 lidar have enabled to minimize the errors induced by the lidar motion.

  The main wind magnitudes of study have been HWS, VWS, WD, and TI, in both high- (1s) and low-time resolution (10min). Backscatter and SV have been found to have a relevant role when studying the quality of these measurements. The inherent homodyne Doppler detection technique of the ZephIR lidar causes 180-deg phase jumps with severe impact on the WD estimates. This error has been corrected by using as reference WD the unambiguous WD measured by the sonic anemometer of the lidar buoy (Chap. 5).

- *On mechanical motion compensation of the floating lidar .-*

  A cardan frame, which virtually keeps the lidar stand still and pointing to the zenith, has been tested and optimized both in laboratory and near-shore conditions. Regarding the lab-based tests, sinusoidal motion (amplitude, $A = 16$ *deg*, and period, $T = 12$ *s*) has been applied without and with cardan compensation. Without cardan compensation (cardan frame blocked) there is a clear deterioration of all 1-s data statistical parameters, which fall below the required KPIs (Tab. 3.11). When the cardan frame is unblocked the motion amplitude reduces drastically (from 16 *deg* down to 2 *deg*). As a result, motion-induced fluctuations in the 1-s HWS time series are filtered out, the HWS distribution is less scattered and the determination coefficient approaches unity. e conditions. Regarding the lab-based tests, sinusoidal motion (amplitude, $A = 16$ *deg*, and period, $T = 12$ *s*) has been applied without and with cardan compensation. Without cardan compensation (cardan frame

blocked) there is a clear deterioration of all 1-s data statistical parameters, which fall below the required KPIs (Tab. 3.11). When the cardan frame is unblocked the motion amplitude reduces drastically (from 16 *deg* down to 2 *deg*). As a result, motion-induced fluctuations in the 1-s HWS time series are filtered out, the HWS distribution is less scattered and the determination coefficient approaches unity. A physical harmonic model based on a simple compound pendulum with one degree of freedom has enabled to understand the resonant behavior in near-shore conditions at PdP.

- *On the signal processing and filtering tools developed .-*

    1. A basic *delay-correction* algorithm has been developed compensate for the travel time between two non-collocated fixed lidars (Chap. 4).
    2. The *window-averaging algorithm* algorithm uses a rectangular window of adaptive time length recomputed on a 10-min time basis. The time length equals the inverse of the peak frequency of the angular-velocity spectrum (pitch/roll) of the buoy. This algorithm has proven very effective to minimize the impact of the wave-induced angular motion. For 1-s data, it has been shown that KPIs compliance improves from 30% to 80% of the measurement sample (Chap. 4).
    3. *SV filtering* uses a SV threshold above which HWS measurements are treated as outliers. This filtering algorithm entails a trade-off between KPI improvement and data availability (Chap. 4).
    4. The *homodyne WD-correction algorithm* uses sequential correction of the WD at each successive measurement height of the lidar. The algorithm uses a bottom-up approach such that departing from the WD measured at buoy level (sonic anemometer), the WD measured at the *(i-1)-th* height is used as reference for the WD at the *i-th* height and so on (Chap. 5).

An in-depth study comparing “floating” and “reference“ HWS and TI lidar measurements at 100 m in height for the 38-day campaign at PdP are summarised in Fig. 4.17 and Tab. 4.1.It comes as no surprise that angular motion and lidar-observed turbulence are the main error sources affecting the floating lidar.

On the VAD simulator and TI estimation .- The VAD simulator uses Euler’s angle formulation (pitch, roll, yaw) to relate the LoS-velocity projections of the wind vector in the fixed coordinate system to the rotated one, where the wind vector is estimated.

Two simple motional cases have been presented: static and dynamic (sinusoidal) tilting. The static case has shown the dependence of the HWS retrieved error on the WD whereas the dynamic case evidenced non-symmetrical errors with the WD. The importance of the initial phase angle of the motion and at lidar scanning has graphically been introduced in Fig. 6.10 to motivate the important role in *comprehensive models*.

One of such models is the mathematical formulation given in Chap. 6 to *estimate the 10-min motion-induced standard deviation and apparent TI without accessing individual LoS* *information of the lidar scanning pattern (undisclosed by the manufacturer).* This method is based on the VAD simulator so far presented and that roll and pitch amplitudes are linearly correlated. As a result of this assumption, HWS standard deviation becomes independent of WD.

Eq. 6.17 provides the mathematical framework to combine the inherent variance (as a synonym of turbulence) of the wind with the motion-induced one. As a first approach, uncorrelated and linearly-correlated cases have yielded upper and lower bounds of motion-corrected HWS standard deviation. The proposed formulation (Sec. 6.3.1) has been applied using to EOLOS commissioning phase at IJmuiden, where both a sonic anemometer and a fixed lidar of the same type were used as references. Binned analysis has shown overall correction of the motion-induced HWS standard deviation.

- *On technology transfer and market results .-*

  Finally, trial validation and evolution of offshore lidar buoy EOLOS FLS200 has been shown in the measurement campaign carried out at PdP (Chap. 4, prototype buoy) and IJmuiden (Chap. 5, commissioning tests).

  EOLOS spin-off (European EIT Innovation Award 2015) is the key result of European project NEPTUNE and holds promise to effectively measure the wind resource at candidate wind-farm locations.

7.2 Outlook

As shown in this Ph.D., floating lidar technology faces challenges, a key one being the impact of floating lidar buoy movement in the wind measurement, which should be minimized and better understood to limit the motion-induced uncertainty of the measurement.

1. At *motion-simulator level*, the VAD simulator developed (*Tiana-Alsina et al.*, 2017) in the framework of EU project NEPTUNE relies on the simplifying assumption of uni-modal harmonic excitation to simulate pitch and roll lidar-buoy motion. Further research is to include:
   - adaptation of the VAD simulator to be excited with real-data motional records acquired from buoy IMUs. This is to enable performance evaluation of the proposed motion-correction algorithms under real sea conditions.
   - all 6 degrees of freedom in the simulator (rotational and translational) as well as
   - simulation of non-uniform wind fields over the scanning volume of the lidar.
2. At *algorithm level*, future actions comprise:
   - improvement of the “window-averaging technique” (Chap. 4) in order to assimilate both pitch and roll IMU information and to allow comparison with “wave period” and “significant wave height” measured by the wave sensor on the buoy. So far, the window-averaging algorithm is limited to only one degree of freedom (either pitch or roll; assumption of linear correlation) and the temporal averaging length is estimated as the

inverse of the frequency yielding the peak power spectrum density (PSD) of the roll (or pitch)-angle timeseries, alternatively, the mean 3-dB cut-off frequency.

- application of Principal Component Analysis (PCA) and machine learning algorithms to help unveil hidden correlations among the huge dataset collected during the three measurement campaigns (UPC-LIM lab tests, PdP, and IJmuiden).
- implementation of the Homodyne WD correction algorithm enunciated in Chap. 5 at high resolution data.

3. At measurement campaign level, and in the framework of recently granted project PGC2018-094132-B-I00 of the Spanish National Science foundation, it is planned to expand research at either Riso DTU facilities or MARHIS Scientific-Technical Singular Infrastructure (ICTS) operated by the Laboratory of Maritime Engineering (LIM/UPC and lead partner in this scientific field).

Appendix A

List of Publications

A.1 Journals

1. Gutiérrez-Antuñano, M. A., Tiana-Alsina, J., and Rocadenbosch, F. (2017) Performance evaluation of a floating lidar buoy in nearshore conditions. *Wind Energ.*, 20: 1711– 1726. doi: 10.1002/we.2118.
2. Gutiérrez-Antuñano, M.A.; Tiana-Alsina, J.; Salcedo, A.; Rocadenbosch, F. (2018) Estimation of the Motion-Induced Horizontal-Wind-Speed Standard Deviation in an Offshore Doppler Lidar. *Remote Sens.* 2018, 10, 2037. doi: 10.3390/rs10122037

A.2 International Conferences

1. Gutiérrez-Antuñano, M. A., Tiana-Alsina, J., Bischoff O. Cateura, J. and Rocadenbosch, F. (2015) Performance evaluation of a floating Doppler wind lidar buoy in mediterranean near-shore conditions, *2015 IEEE International Geoscience and Remote Sensing Symposium (IGARSS)*, Milan, 2015, pp. 2147-2150. doi: 10.1109/IGARSS.2015.7326228
2. Tiana-Alsina, J., Gutiérrez-Antuñano, M. A., Würth, I., Puigdefàbregas, J. and Rocadenbosch, F. (2015) Motion compensation study for a floating Doppler wind lidar, *2015 IEEE International Geoscience and Remote Sensing Symposium (IGARSS)*, Milan, 2015, pp. 5379-5382. doi: 10.1109/IGARSS.2015.7327051
3. Tiana-Alsina, J., Rocadenbosch, F. and Gutiérrez-Antuñano, M. A., (2017) Vertical Azimuth Display simulator for wind-Doppler lidar error assessment, *2017 IEEE International Geoscience and Remote Sensing Symposium (IGARSS)*, Fort Worth, TX, 2017, pp. 1614-1617. doi: 10.1109/IGARSS.2017.8127282
4. Gutiérrez-Antuñano, M. A., Tiana-Alsina, J., Rocadenbosch, F., Sospedra, J., Aghabi, R. and González-Marco, D. (2017) A wind-lidar buoy for offshore wind measurements: First commissioning test-phase results, *2017 IEEE International Geoscience and Remote Sensing Symposium (IGARSS)*, Fort Worth, TX, 2017, pp. 1607-1610. doi: 10.1109/IGARSS.2017.8127280

5. Bischoff O, Würth, I., Tiana-Alsina, J., Gutiérrez-Antuñano, M. A., and Cheng P.W. (2014) Motion effects on lidar wind measurement data of the EOLOS buoy, *1st International Conference on Renewable Energies Offshore (RENEW)*, Lisbon, 2014.

A.3 National Conferences

1. Gutiérrez-Antuñano, M. A., (2014) Project NEPTUNE: Development of EOLOS floating LIDAR, *International Energy Agency Topical Expert Meeting*, Wind Task 11, IEA R+D Wind Task 11 - Topical Expert Meeting, Las Palmas, 2014.

A.4 Workshops

1. Gutiérrez-Antuñano, M. A., (2015) NEPTUNE project. *Master's in Renewable Energy (MSc RENE) Innovation Seminar*, Barcelona, 2015.

2. Gutiérrez-Antuñano, M. A., (2018) Project NEPTUNE: Development of an autonomous multi-purpose measurement LIDAR buoy. *Second Training Workshop for Next Generation: Representing environmental complexity in experimental design and acoustic measurement techniques*, Barcelona, 2018.

References

Arfken, G. (1985), Introduction, in *Mathematical Methods for Physicists*, pp. xxi–xxii, Elsevier BV, doi: 10.1016/b978-0-12-059820-5.50008-2. 58

Arranz, P. G. (2011), Measurements in complex terrain using a lidar, *Tech. rep.*, CENER. 59

Associates, B. (2017), Future renewable energy costs: offshore wind update 2017, *Tech. rep.*, KIC Innoenergy. xxv, 2, 4, 5

AWS Truepower (2014), AWS Truepower Loss and Uncertainty Methods, *Tech. rep.*, AWS Truepower. xxv, 19

Banakh, V. A., I. N. Smalikho, F. Köpp, and C. Werner (1995), Representativeness of wind measurements with a cw doppler lidar in the atmospheric boundary layer, *Appl. Opt.*, *34*(12), 2055–2067. xxi, 16, 81

Barlow, R. J. (1989), *Statistics: a guide to the use of statistical methods in the physical sciences*, Manchester physics series, Wiley, Chichester. 62, 83, 87

Belu, R., and D. Koracin (2013), Statistical and spectral analysis of wind characteristics relevant to wind energy assessment using tower measurements in complex terrain, *Journal of Wind Energy*, p. 12, doi: 10.1155/2013/739162. 57

Bischoff, O., D. Schlipf, I. Würth, and P. Cheng (2015), Dynamic motion effects and compensation methods of a floating lidar buoy, in *EERA DeepWind 2015 Deep Sea Offshore Wind Conference*, edited by E. E. R. A. (EERA). 8, 57

Bolaños, R., G. Jordà, J. Cateura, J. Lopez, J. Puigdefabregas, J. Gomez, and M. Espino (2009), The XIOM: 20 years of a regional coastal observatory in the spanish catalan coast, *Journal of Marine Systems*, *77*(3), 237–260. 26

Bole, A. (1991), IALA aids to navigation guide (NAVGUIDE). international association of lighthouse authorities (IALA). 168 pages, plus annexes, 29·7 × 21 cm, IALA, 1990. 30 SF., *Journal of Navigation*, *44*(03), 438, doi: 10.1017/s0373463300010316. 73

Bonner, W. D. (1968), Climatology of the low level jet, *Monthly Weather Review*, *96*(12), 833–850, doi: 10.1175/1520-0493(1968)096<0833:COTLLJ>2.0.CO;2. 18

Canadillas, B., A. Bégué, and T. Neumann (2010), Comparison of turbulence spectra derived from lidar and sonic measurements at the offshore platform FINO1, in *Proceedings DEWEK 2010 German Wind Energy Conference*, DEWI. 64

Carbon Trust (2013), Carbon trust offshore wind accelerator roadmap for the commercial acceptance of floating lidar technology, *Tech. rep.*, Carbon Trust. xix, xxv, 6, 8, 19, 20, 21, 22, 24, 50, 52, 57, 72, 75, 76, 78

Clifford, S. F., J. C. Kaimal, R. J. Lataitis, and R. G. Strauch (1994), Ground-based remote profiling in atmospheric studies: an overview, *Proceedings of the IEEE*, *82*(3), 313–355, doi: 10.1109/5.272138. 81

Clifton, A., and M. Courtney (2013), 15. ground-based vertically profiling remote sensing for wind reosurce assessment, *Tech. rep.*, IEA Wind expert group study on recommended practices. 19, 24

Clifton, A., et al. (2018), IEA wind task 32: Wind lidar identifying and mitigating barriers to the adoption of wind lidar, *Remote Sensing*, *10*(3), 406, doi: 10.3390/rs10030406. 24

Cool, G. A. (2016), Floating LIDAR technology. oceanographic parameters influencing accuary of wind vector reconstruction, Master's thesis, Aerospace Eng., Delf University of Technology. 50

Courtney, M., A. Clifton, and A. Rettenmeier (2012), Wind lidar systems for wind energy deployment (LIDAR), *Tech. rep.*, International Energy Agency (IEA). 19

Courtney, M. S., and C. B. Hasager (2016), *Remote sensing technologies for measuring offshore wind*, chap. 4, pp. 59–82, Elsevier. 49

Frisch, U. (1995), *Turbulence: The Legacy of AN Kolmogorov*, Cambridge University Press. 64

Fujii, T., and T. Fukuchi (2005), *Laser remote sensing*, CRC Press. xvii, xxi, 14, 15, 16, 18, 80, 81

Gottschall, J., H. Lilov, G. Wolken-Möhlmann, and B. Lange (2012a), Lidars on floating offshore platforms; about the correction of motion-induced lidar measurement errors, in *EWEA 2012 proceedings*, edited by EWEA. 8, 57, 80

Gottschall, J., M. Courtney, R. Wagner, H. E. Jørgensen, and I. Antoniou (2012b), Lidar profilers in the context of wind energy–a verification procedure for traceable measurements, *Wind Energy*, *15*(1), 147–159. 50

Gottschall, J., G. Wolken-Möhlmann, T. Viergutz, and B. Lange (2014), Results and conclusions of a floating-lidar offshore test, *Energy Procedia*, *53*, 156 – 161. 99

Goyer, G. G., and R. Watson (1963), The laser and its application to meteorology, *Bulletin of the American Meteorological Society*, *44*(9), 564–570, doi: 10.1175/1520-0477-44.9.564. 13

Grifoll, M., J. Navarro, E. Pallares, L. Ràfols, M. Espino, and A. Palomares (2016), Ocean–atmosphere–wave characterisation of a wind jet (ebro shelf, nw mediterranean sea), *Nonlin. Processes Geophys.*, *23*, 143–158. 90

Gutiérrez, M. A., J. Tiana-Alsina, O. Bischoff, J. Cateura, and F. Rocadenbosch (2015), Performance evaluation of a floating doppler wind lidar buoy in mediterranean near-shore conditions, in *Geoscience and Remote Sensing Symposium Proceedings*. 49, 69

Gutiérrez-Antuñano, M., J. Tiana-Alsina, A. Salcedo, and F. Rocadenbosch (2018), Estimation of the motion-induced horizontal-wind-speed standard deviation in an offshore doppler lidar, *Remote Sensing*, *10*(12), 2037, doi: 10.3390/rs10122037. 79

Gutierrez-Antunano, M. A., J. Tiana-Alsina, F. Rocadenbosch, J. Sospedra, R. Aghabi, and D. Gonzalez-Marco (2017), A wind-lidar buoy for offshore wind measurements: First commissioning test-phase results, in *2017 IEEE International Geoscience and Remote Sensing Symposium (IGARSS)*, Institute of Electrical and Electronics Engineers (IEEE), doi: 10.1109/igarss.2017.8127280. 71, 72, 85

Gutiérrez-Antuñano, M. A., J. Tiana-Alsina, and F. Rocadenbosch (2017), Performance evaluation of a floating lidar buoy in nearshore conditions, *Wind Energy*, *20*(10), 1711–1726, doi: 10.1002/we.2118. 49, 99

Hansen, K. S., R. J. Barthelmie, L. E. Jensen, and A. Sommer (2012), The impact of turbulence intensity and atmospheric stability on power deficits due to wind turbine wakes at horns rev wind farm, *Wind Energy*, *15*(1), 183–196, doi: 10.1002/we.512. 80

Hardesty, R. M., and B. F. Weber (1987), Lidar measurement of turbulence encountered by horizontal-axis wind turbines, *Journal of Atmospheric and Oceanic Technology*, *4*(1), 191–203, doi: 10.1175/1520-0426(1987)004<0191:LMOTEB>2.0.CO;2. 13

Ilas, A., P. Ralon, A. Rodriguez, and M. Taylor (2018), Renewable power generation costs in 2017, *Tech. rep.*, International Renewable Energy Agency IRENA. xvii, 3, 4

International Electrotechnical Commission (1998), IEC 61400-12 wind turbine power performance testing, *Tech. rep.*, International Electrotechnical Commission. 1, 19

International Electrotechnical Commission (2005), IEC 61400-1 2005 Wind turbine power performance testing, *Tech. rep.*, International Electrotechnical Commission. 80

International Energy Association (2007), State of the art of remote wind speed sensing techniques using sodar, lidar and satellites, *Tech. rep.*, International Energy Association. 2

KIC InnoEnnergy (2015), Neptune project leaflet, *Tech. rep.*, KIC InnoEnergy. xvii, 5, 6

Kost, C., and T. Schlegl (2018), Levelized cost of electricity renewable energy technologies, *Tech. rep.*, Fraunhofer Institut for solar energy systems ISE. 2, 3

M. Pitter, E. B. d. R., J. Medley, M. Mangat, C. Slinger, and M. Harris (2014), Performance stability of zephir in high motion enviroments: floating and turbine mounted, *Tech. rep.*, ZephIR. 62, 80

Mangat, M. (2016), Repeatability of ZephIR 300 performance, *Tech. rep.*, ZephIR Lidar. 18

Manwell, J. F., J. G. McGowan, and A. L. Rogers (2009), *Wind energy explained: theory, design and application*, Book, Whole, Wiley, Chichester, U.K. 80

Nicholls-Lee, R. (2013), A low motion floating platform for offshore wind resource assessment using lidars, in *ASME 2013 32nd International Conference on Ocean, Offshore and Arctic Engineering*, pp. V008T09A036–V008T09A036, American Society of Mechanical Engineers. 23

Nino, R., and P. Eecen (2001), Turbulence and wind shear: a literature study and measurements, *ECN, Petten*. 54

Nunalee, C. G., and S. Basu (2014), Mesoscale modeling of coastal low-level jets: implications for offshore wind resource estimation, *Wind Energy*, *17*(8), 1199–1216, doi: 10.1002/we.1628. 19

Papoulis, A. (1965), *Probability, random variables, and stochastic processes.*, McGraw-Hill, New York. 84

Pichugina, Y. L., R. M. Banta, W. A. Brewer, S. P. Sandberg, and R. M. Hardesty (2011), Doppler lidar–based wind-profile measurement system for offshore wind-energy and other marine boundary layer applications, *Journal of Applied Meteorology and Climatology*, *51*, 327–349. 2

Poveda, J., D. Wouters, and S. E. C. Nederland (2015), *Wind Measurements at Meteorological Mast IJmuiden*, ECN.: E-series ECN-E–14-058, ECN. 72

Proakis, J. G., and D. K. Manolakis (2006), *Digital Signal Processing (4th Edition)*, Prentice-Hall, Inc., Upper Saddle River, NJ, USA. 50, 58, 64

Rodrigo, J. S. (2010), State-of-the-art of wind resource assessment, *Deliverable D7*, Centro Nacional de Energías Renovables (CENER). 1, 2

Sathe, A. (2012), Influence of wind conditions on wind turbine loads and measurements of turbulence using lidars, Ph.D. thesis, Delft University, Wind Energy Research Institute. 80

Sathe, A., J. Mann, J. Gottschall, and M. Courtney (2011), Can wind lidars measure turbulence?, *Journal of Atmospheric and Oceanic Technology*, *28*(7), 853–868. 50, 80

Sathe, A., R. Banta, L. Pauscher, K. Vogstad, D. Schilpf, and S. Wylie (2015), Estimating turbulence statistics and parameters from ground- and nacelle-based lidar measurements, *Tech. rep.*, Technical University of Denmark. 80

Schlipf, D., A. Rettenmeier, F. Haizmann, M. Hofsäß, M. Courtney, and P. W. Cheng (2012), Model based wind vector field reconstruction from lidar data, in *Proceedings of the 11th German Wind Energy Conference DEWEK 2012*. 58

Schuon, F., D. González, F. Rocadenbosch, O. Bischoff, and R. Jané (2012), KIC InnoEnergy Project Neptune: Development of a Floating LiDAR Buoy for Wind, Wave and Current Measurements, in *Proceedings DEWEK 2012 German Wind Energy Conference*, DEWI. 5, 23, 71

Sjöholm, M., T. K. Mikkelsen, L. Kristensen, J. Mann, and P. Kirkegaard (2010), Spectral analysis of wind turbulence measured by a doppler lidar for velocity fine structure and coherence studies, in *In Detailed Program (online)*. 54

Smullin, L. D., and G. Fiocco (1962), Optical echoes from the moon, *Nature*, *194*(4835), 1267–1267, doi: 10.1038/1941267a0. 13

Sonnenschein, C. M., and F. A. Horrigan (1971), Signal-to-noise relationships for coaxial systems that heterodyne backscatter from the atmosphere, *Appl. Opt.*, *10*(7), 1600–1604, doi: 10.1364/AO.10.001600. 15

Sospedra, J., J. Cateura, and J. Puigdefàbregas (2015), Novel multipurpose buoy for offshore wind profile measurements eolos platform faces validation at ijmuiden offshore metmast, *Sea technology*, *56*(7), 25–28. 50, 73

Spieth, N. (2013), Simulation eines bewegten lidarsystems, Master's thesis, University of Stuttgart. 44

Synge, E. H. (1930), XCI. a method of investigating the higher atmosphere, *The London, Edinburgh, and Dublin Philosophical Magazine and Journal of Science*, *9*(60), 1014–1020, doi: 10.1080/14786443008565070. 13

Taylor, G. I. (1938), The spectrum of turbulence, *Proceedings of the Royal Society of London. Series A, Mathematical and Physical Sciences*, *164*(919), 476 – 490. 55

Tiana-Alsina, J., O. Bischoff, and F. Rocadenbosch (2013a), KIC-Project NEPTUNE: Evaluation report and recommendations (test campaign i). 23

Tiana-Alsina, J., I. Würth, and F. Rocadenbosch (2013b), KIC-Project NEPTUNE: Evaluation report and recommendations (test campaign ii). 23

Tiana-Alsina, J., M. A. Gutiérrez, I. Würth, J. Puigdefàbregas, and F. Rocadenbosch (2015), Motion compensation study for a floating doppler wind lidar, in *Geoscience and Remote Sensing Symposium Proceedings*. 23

Tiana-Alsina, J., F. Rocadenbosch, and M. A. Gutierrez-Antunano (2017), Vertical azimuth display simulator for wind-doppler lidar error assessment, in *2017 IEEE International Geoscience and Remote Sensing Symposium (IGARSS)*, Institute of Electrical and Electronics Engineers (IEEE), doi: 10.1109/igarss.2017.8127282. xxii, 79, 86, 94, 107

Vaughan, J., and P. Forrester (1989), Laser doppler velocimetry applied to the measurement of local and global wind, *Wind Engineering*, *13*(1), 1–15. 13

Wagner, R., T. Mikkelsen, and M. Courtney (2009), Investigation of turbulence measurements with a continuous wave, conically scanning lidar, *Tech. rep.*, DTU. 54, 56, 80

Werkhoven, E. J., and J. P. Verhoef (2012), Offshore meteorological mast ijmuiden abstract of instrumentation report, *Tech. rep.*, Energy Research Centre of the Netherlands (ECN). 10, 72

Wharton, S., and J. Lundquist (2012), Assessing atmospheric stability and its impacts on rotor-disk wind characteristics at an offshore wind farm, *Wind Energy*, *15*(4), 525–546, doi: 10.1002/we.483. 51

Zhang, D.-L., S. Zhang, and S. J. Weaver (2006), Low-level jets over the mid-atlantic states: Warm-season climatology and a case study, *Journal of Applied Meteorology and Climatology*, *45*(1), 194–209, doi: 10.1175/JAM2313.1. 18